

# **A path towards quantum metamaterials**

## **Ein Weg zu Quantenmetamaterialien**

Zur Erlangung des akademischen Grades eines  
DOKTORS DER NATURWISSENSCHAFTEN  
von der Fakultät für Physik des  
Karlsruher Institut für Technologie (KIT)

genehmigte

DISSERTATION

von

Dipl.-Phys. Pascal Macha  
aus Flensburg

**Tag der mündlichen Prüfung:** 7. Juni 2013

**Referent:** Prof. Dr. Alexey V. Ustinov

**Korreferent:** Prof. Dr. Evgeni Il'ichev



Für Nadine.



# Contents

<b>1</b>	<b>Introduction</b>	<b>1</b>
<b>2</b>	<b>Fundamentals</b>	<b>7</b>
2.1	The flux qubit . . . . .	7
2.1.1	Superconductivity and Josephson junctions . . . . .	8
2.1.2	From classical physics to quantum physics . . . . .	10
2.1.3	Coupled qubits . . . . .	15
2.2	Atoms and photons . . . . .	20
2.2.1	The Tavis-Cummings model . . . . .	21
2.2.2	Semiclassical treatment . . . . .	23
2.2.3	Analysis of the resonant behaviour . . . . .	24
2.2.4	Dispersive regime . . . . .	28
<b>3</b>	<b>Dressed state amplification</b>	<b>31</b>
3.1	The sample and experimental setup . . . . .	32
3.1.1	The sample . . . . .	33
3.1.2	Experimental setup . . . . .	34
3.2	A single qubit and a resonator . . . . .	38
3.2.1	Spectroscopy . . . . .	38
3.2.2	Ground state measurement . . . . .	40
3.2.3	Estimation of coherence times . . . . .	41
3.3	Temperature dependence . . . . .	43
3.3.1	Dispersive shift . . . . .	43
3.3.2	Change of flux bias . . . . .	43
3.4	Dressed states . . . . .	46
3.4.1	Multiphoton transitions . . . . .	47
3.4.2	AC-Zeeman shift . . . . .	52
3.4.3	Rabi resonance and level inversion . . . . .	53

<b>4</b>	<b>Implementation of a quantum metamaterial</b>	<b>59</b>
4.1	The sample . . . . .	60
4.1.1	The resonator . . . . .	61
4.1.2	The qubits . . . . .	63
4.2	Characterization of parameters . . . . .	67
4.2.1	Spectroscopy . . . . .	68
4.2.2	Reconstruction from higher harmonics . . . . .	71
4.2.3	Ground state measurement . . . . .	75
4.3	Resonant interaction . . . . .	78
4.3.1	Analysis of the resonant modes . . . . .	80
4.3.2	The higher harmonics . . . . .	84
4.3.3	Two stable states . . . . .	87
4.4	Strong driving and tuning the metamaterial . . . . .	88
4.4.1	Multiphoton processes . . . . .	90
4.4.2	Tuning of the qubit ensembles . . . . .	92
4.4.3	Additional effects . . . . .	101
<b>5</b>	<b>Conclusion</b>	<b>105</b>
	<b>Appendix</b>	<b>111</b>
	<b>References</b>	<b>113</b>
	<b>List of publications</b>	<b>129</b>
	<b>Acknowledgements</b>	<b>131</b>

# 1 Introduction

## Superconducting qubits as artificial atoms

Superconducting quantum circuits opened up a rapidly expanding research field with new possibilities compared to experiments with natural quantum particles such as atoms and spins [CW08]; [YN11]; [DS13]. The key element of such circuits is the superconducting quantum bit (qubit). It acts as artificial atom whose main properties can not only be designed and engineered during the fabrication phase, but also be tuned dynamically during the experiment. Although it is of macroscopic dimension, its characteristics obey the laws of quantum mechanics [NPT99]; [PCC+09]; [FPC+00]. For instance, the flux qubit is defined by two quantum mechanical states, which are characterized by opposite macroscopic currents in a loop having persistent currents of  $1 \mu\text{A}$  carried by a million pairs of electrons. Still it possesses quantum behaviour manifested in the tunnelling of the long-lived macroscopic magnetic moments [FMF+11].

Superconducting qubits are fabricated with nano-lithography technology and can be integrated into complex electronic circuits for precise control and measurement. These characteristics have led to the exploration of light-matter interaction at the single particle level [WSB+04]; [CNH+03], verification of fundamental concepts of quantum physics [AWB+09]; [WJP+11] and, in addition, they yield a strong application as basic elements for a future quantum computer [GDS09]. Yet another application for the qubit is the field of quantum simulation. Unlike a quantum computer which implements a universal set of quantum gates, in the quantum simulations approach specific Hamiltonians for defined problems are experimentally realized and analysed [CZ12]; [HTK12]. For those applications low coherence times have been a limitation for a long time. Recent progress in both, material science [CVC+13] and microwave engineering [PSB+11]; [RGP+12] pushed them to tens of microseconds.

All in all, it is save to say, that in the past years studies with superconducting qubits went beyond copying text book experiments from quantum mechanics (or quantum optics) to conquer new realms of physics, which have not been possible to reach up to now. One very recent milestone experiment has been the implementation of continuous quantum feedback control [WM93] by the demonstration of persistent Rabi oscillations [VMS+12], only shortly after the first ever realization of continuous quantum feedback [SDZ+11].

The superconducting flux qubit [MOL+99] is the fundamental element of this thesis. It effectively is, and serves as, an artificial quantum mechanical two-level system. Its transition frequency can be tuned *in situ* by an external magnetic field, which will be used to study the interaction between such systems and a multi mode cavity. The two fundamental elements, the cavity and the qubit, will be introduced in chapter 2.

### **Cavity Quantum Electrodynamics based on solid state physics**

Coupling a single artificial two-level system to a photon field in a superconducting microwave resonator (cavity) is the foundation of circuit quantum electrodynamics (cQED), i.e. a research field studying coherent quantum phenomena based on light-matter interaction in electrical circuits. The effective dipole moment of a superconducting qubit is several orders of magnitude larger than the dipole moment of a natural atom. This makes it possible to bring many-photon non-linear quantum optics to the single photon level. Outstanding examples are the observation of the Bloch-Siegert shift for the vacuum field of a resonator [FDLM+10] and the implementation of a Kerr medium at the single photon level [KVL+13].

Here, a first step towards another important ubiquitous quantum effect, namely lasing, is taken. Lasing stands for Light Amplification by Stimulated Emission of Radiation. Interestingly, the amplification process works even with a single atom [MBB+03], which has also been demonstrated using a superconducting charge qubit [AIN+07]. In the latter work, the quasiparticle bath of the superconductor serves as a third level in order to create a population inversion, one of three fundamental requirements for stimulated emission. This could be referred to as the active medium. The other two requirements are a pumping process to maintain the level

inversion in the active medium and a high quality cavity to ensure that photons are trapped long enough to pass through the cavity several times before leaving the cavity. A flux qubit has been used to realize cooling and amplification of a classical resonator [GPI+08]. In principle, this effect is similar to Rabi spectroscopy [IOI+03] and in the quantum picture – using a quantum resonator – it can be interpreted as lasing at the Rabi frequency [HFH+08]. In that scheme the pumping is done by coherently driving the two level system, creating a level inversion in the dressed state basis, which may be called lasing with a hidden inversion [MC00]. For atomic systems a similar effect has been demonstrated using the Rabi sidebands [WED+77]; [KVG88], as a transition directly at the Rabi frequency does not occur and, in addition, its frequency is typically too low to be accessible. Employing superconducting qubits, it is possible to use the direct transition at the Rabi frequency [HFH+08].

In chapter 3 of the thesis, a single qubit coupled to a superconducting high quality resonator is analysed and its level population is controlled by microwave driving. Initially, it is fully characterized, before experiments on the strongly driven system are presented.

### **Quantum metamaterials**

One natural pathway for the evolution of experiments with solid state qubits is to expand the system to many qubits. On the one hand, individually controlled qubits are used to build up quantum registers for future quantum computers [FSB+11]; [LBC+12]; [JPM+12]. Realizing such quantum registers requires individual readout and sophisticated control over each qubit. On the other hand, ensembles of coupled qubit systems can be employed to form artificial quantum materials. In this approach, the focus lies on the observation of collective quantum phenomena [RZS+08].

In reference to the field of metamaterials, a coupled qubit system may be referred to as a quantum metamaterial. Generally, metamaterials are any kind of artificially created structures with properties either unknown in nature or mimicking nature. They are of subwavelength scale and used to manipulate the propagation of electro-magnetic waves [ZK12]. Resonant structures, such as the split ring resonator, play the role of artificial atoms and shape the effective magnetic response. Superconducting metamate-

materials have moved into the spotlight for their very low ohmic losses and the possibility to tune their resonance by exploiting the non-linear Josephson inductance [ROA05]; [Anl11]. One example is the implementation of a metamaterial based on radio frequency superconducting interference devices (RF-SQUIDS) [DCL06]; [LT07], which has recently been realized [JBS+13]. In a similar configuration, by using DC-SQUIDS in a resonator, amplification and squeezing of quantum noise has been demonstrated [CBIH+08]. Today, these so-called Josephson parametric amplifiers are widely used and have led to the observation of quantum jumps in a superconducting qubit [VSS11]. Additionally, the cavities themselves can also act as a metamaterial. There has been a recent proposal to implement ideas from classical left-handed metamaterials, a left-handed transmission line, in the realm of circuit QED [EW13].

An analogue system for quantum metamaterials as implemented here, are spin ensembles found in nature. They have attracted renewed interest, because they are the basis for one possibility of hybrid quantum systems [XAY+13]. In such a hybrid system different quantum systems are combined in such a way to profit from the advantages while eliminating the drawbacks of each individual system. One example is the combination of natural spins and superconducting circuits. The storage of excitations in an electron spin ensemble and its use as quantum memory has been demonstrated [SSG+10]; [WGW+10]. Another future application of hybrid systems might be as an interface between microwave and optical frequencies, as offered by the use of Erbium [BFR+11].

One of the clear advantages of natural spin systems compared to artificial qubit materials is that they consist of identical atoms. Although this might appear trivial from the point of view of atomic systems, it is challenging for superconducting qubits. The properties of each qubit strongly depend on the fabrication parameters. In a linear qubit chain, which relies on nearest-neighbour interaction, a single off-resonant qubit may act as defect and may therefore destroy the collective modes. This can be circumvented by using a cavity as coupling element between the qubits. By carefully designing the coupling of the qubits to the cavity it is possible to make only multi-qubit resonances visible. In chapter 4, the realization of such an experiment with 20 superconducting flux qubits embedded into a single microwave resonator is reported. The phase of

the signal transmitted through the resonator reveals the resonant coupling of up to 8 qubits. Quantum systems based on this proof-of-principle experiment of many coupled artificial atoms with tunable parameters offer wide prospects: From the realization of a single photon detector in the microwave regime [RGRS09], over phase switching [Tia10] to the observation of a superradiant phase transition [LCJ+09].



## 2 Fundamentals

*This thesis deals with the interaction between artificial atoms and photons. Here, the building blocks will be introduced. In particular, these are the flux qubit, and the interaction between a resonator and the flux qubit.*

*There are a lot of different implementations of superconducting qubits. Currently, the most spread version of superconducting qubits is the so-called transmon [KYG+07], and with one of the biggest groups moving from phase qubits to transmons [BKM+13], it is dominating the research field by far. However, the flux qubit features important advantages for certain applications. For example, its high anharmonicity allows to drive the system very strongly while the two-level approximation is still valid. This will be of importance in chapter 3, where Rabi frequencies up to several GHz are realized. Furthermore, the flux qubit's small size is of advantage for the experiment described and analysed in chapter 4. There, many qubits are embedded into a single cavity and their small size makes it possible to couple them uniformly to the cavity.*

*In the first section 2.1 of the current chapter the properties of the flux qubit are introduced, whereas the second section 2.2 discusses the cavity and its interaction with the qubits.*

### 2.1 The flux qubit

The flux qubit or persistent current qubit is one of three fundamental realizations of superconducting qubits. All of them rely on the integration of one or more Josephson junctions into a superconducting circuit. The junctions serve as non-linear dissipation less inductance, which is shown in subsection 2.1.1. Together with the remaining circuit a non-linear quantum oscillator is formed. The properties of this oscillator and its quantum mechanical nature are discussed in 2.1.2. When the energy space

is truncated to the first two levels, which is justified by the anharmonicity, the system becomes a quantum mechanical two-level system, hence qubit. The properties of this qubit can be controlled by static magnetic and electric fields as well as by microwave radiation. Different coupling mechanisms of qubits are reviewed in subsection 2.1.3. Of special interest is how strong such interactions can get without significantly altering the properties of the coupled system when compared to a single qubit.

### 2.1.1 Superconductivity and Josephson junctions

More than 100 years ago Helium was liquefied for the first time by Kamerlingh Onnes. This event led to the important follow up discovery that the resistance of mercury vanishes below a critical temperature of 4.2 K, which opened up the field of superconductivity. The newly discovered phase was described phenomenologically by a vanishing resistance for electric current and a complete screening of external magnetic field. The theory of John Bardeen, Leon N. Cooper and John R. Schrieffer explained superconductivity by an attractive interaction between two electrons mediated by phonons. These so-called Cooper pairs condense into a single state at temperatures well below the critical temperature. The observation of flux quantization inclined that copper pairs are indeed responsible for the effect of superconductivity. The flux  $\Phi$  resulting from a superconducting current running in a closed loop is a whole-number multiple  $n$  of the flux quantum  $\Phi_0 = \frac{h}{2e}$ . Following Feynman [FLS71], this phenomenon is intuitively explained by the idea of a common ground state. The common phase of the superconducting state  $\Psi(r, t) = \sqrt{\rho}e^{i\theta(r,t)}$  is denoted by  $\theta$  and  $\rho$  is the Cooper pair density. Because the wave function is single valued the change of the phase over a closed path is an integer multiple of  $2\pi$ . The London equation  $\frac{\hbar}{q}\nabla\theta = \mathbf{A}$  links the flux and the phase. Here,  $\mathbf{A}$  is the vector potential of the electromagnetic field threading the loop with area  $O$  and the carrying charge  $q$  of superconductivity. Finally, using Stokes theorem and rewriting flux  $\Phi$  yields

$$\Phi = \int_O \mathbf{B}d\mathbf{F} = \int_O \nabla \times \mathbf{A}d\mathbf{F} = \oint_{\partial O} \mathbf{A}ds = \oint_{\partial O} \frac{\hbar}{q}\nabla\theta ds = \frac{h}{q} \cdot N, \quad (2.1)$$

where  $\hbar/q$  is the flux quantum with  $q = 2e$  and  $N$  an integer. The flux quantization will be of use later for the construction of the energy potential of the flux qubit.

When two superconductors are separated by a weak link, which can be an insulator forming a tunnel barrier, even in the absence of a voltage a current is flowing with

$$I = I_c \sin(\phi) , \quad (2.2)$$

where  $I_c$  is the critical current of the contact and  $\phi$  the phase difference between the wave functions of the bosonic mode left and right of the contact. Such a superconductor-insulator-superconductor (SIS) contact is called a Josephson junction. The critical current is proportional to the area of the junction and to the critical current density  $J_c$ , which generally depends on the electrode material and the type of the barrier. It decreases with the thickness  $h$  of the barrier as  $e^{-h}$ , and for Al-AlO-Al junctions with the oxidation time  $t$  for the barrier as  $e^{-t}$ . For junction calibration proposes the critical current can be estimated from the normal state resistance  $R_N$  with  $I_c \approx \Delta/R_N$  [AB63]. In addition to the first Josephson relation (2.2), the second Josephson relation connects the time evolution of the phase with the voltage across the junction as

$$V = \frac{\hbar}{2e} \frac{d\phi}{dt} . \quad (2.3)$$

By combining Equation (2.2) and Equation (2.3) in Farady's law  $V = -L_J \partial_t I$ , the junction's inductance is obtained as

$$L_J = \frac{\Phi_0}{2\pi I_c \cos \phi} . \quad (2.4)$$

If the subgap resistance is negligible, the current flow through the junction is basically dissipation-less. Therefore, the junction can be interpreted as a lossless non-linear inductance. The energy stored in the junction is obtained by  $\int V(t)I(t)dt$ , which yields

$$U = E_J \cdot (1 - \cos \phi) , \quad (2.5)$$

where the Josephson energy is  $E_J = \frac{\hbar I_c}{2e}$ . Furthermore, the junction forms a parallel plate capacitor with capacitance  $C$ , which results into the electrostatic energy

$$T_C = \frac{Q^2}{2C} = E_C N_c^2, \quad (2.6)$$

where  $E_C = \frac{4e^2}{2C}$  corresponds to the Coulomb energy of a single Cooper pair stored on the capacitor.  $N_c$  is the difference in number of pairs stored on either side of the junction.

### 2.1.2 From classical physics to quantum physics

For the experiments conducted in chapters 3 and 4, a three-junction flux qubit [MOL+99] is employed. It consists of a superconducting loop with three embedded Josephson junctions. One of them is by a factor of  $\alpha$  smaller than the other two. The flux quantization imposes the following condition for the phase differences  $\phi_i$  across junction  $i$ :

$$\sum_i \phi_i + 2\pi f = 2\pi N, \quad (2.7)$$

where  $f = \Phi/\Phi_0$  is the magnetic frustration of the loop and  $N$  corresponds to the number of flux quanta trapped in the loop. Please note, that the frustration in the experimental part of the thesis refers to the detuning from half a flux quantum,  $\tilde{f} = \Phi - \Phi_0/2$ .

Using condition (2.7) and summing up over the Josephson energy stored in each junction, described by Equation (2.5), the potential energy of the circuit reads

$$\frac{U}{E_j} = 2 + \alpha - \cos \phi_1 - \cos \phi_2 - \alpha \cos(2\pi f - \phi_1 - \phi_2), \quad (2.8)$$

where  $E_j$  is the Josephson energy of one of the large junctions. The self inductance of the qubit loop resulting from its geometric inductance is assumed to be negligible compared to the Josephson inductance. For an elaborate discussion on the matter refer to [Bri05].

To include the dynamics of the system, the kinetic energy of the system must be taken into account. It arrives from the charges stored on the island

between the Josephson junctions and results from the time derivatives of the phases as [OMT+99]

$$T = \frac{1}{2} \left( \frac{\Phi_0}{2\pi} \right)^2 (\dot{\phi}_1 \ \dot{\phi}_2) \cdot \mathbf{C} \cdot \begin{pmatrix} \dot{\phi}_1 \\ \dot{\phi}_2 \end{pmatrix}. \quad (2.9)$$

The capacitance matrix  $\mathbf{C}$  is diagonalized by the transformation to the phase differences  $\phi_p = \phi_1 + \phi_2$  and  $\phi_m = \phi_1 - \phi_2$ .

The potential energy for the new coordinates reads

$$\frac{U_{pm}}{E_j} = 2 + \alpha - 2 \cos(\phi_p/2) \cos(\phi_m/2) - \alpha \cos(2\pi f - \phi_p). \quad (2.10)$$

The potential is shown in Figure 2.1. Along the axis  $\phi_p$  it forms an effective one-dimensional double well potential, which is well separated from neighbouring wells for  $\alpha$  in the range  $[0.5, 1]$ . The barrier height  $E_B$  depends on  $\alpha$  and decreases with decreasing  $\alpha$ . For  $\alpha < 0.5$  the barrier vanishes completely. For  $\alpha > 1$  the potential barriers between different unit cells have the same height and the system becomes two-dimensional.

The two minima correspond to two classical states of opposite circulating currents. The magnitude of the current, the so-called persistent current, is found to be [MOL+99]

$$I_p = \pm I_c \sqrt{1 - \frac{1}{4\alpha^2}}. \quad (2.11)$$

A typical persistent current of  $0.5 \mu\text{A}$  is generated by roughly  $10^6$  Cooper pairs. The difference between the two current states is  $0.01\Phi_0$  in magnetic flux or  $10^6$  Bohr magnetons, which makes the flux qubit a truly macroscopic system. For a particle whose mass relates to the capacitance of the junctions in one of the two minima, the barrier  $E_B$  is classically impenetrable. However, quantum mechanically, it is allowed to tunnel through the barrier with a certain probability.

The flux qubit works in the regime  $E_j > E_C$ , where the phase is well defined. Therefore, the Hamiltonian can be derived from the classical

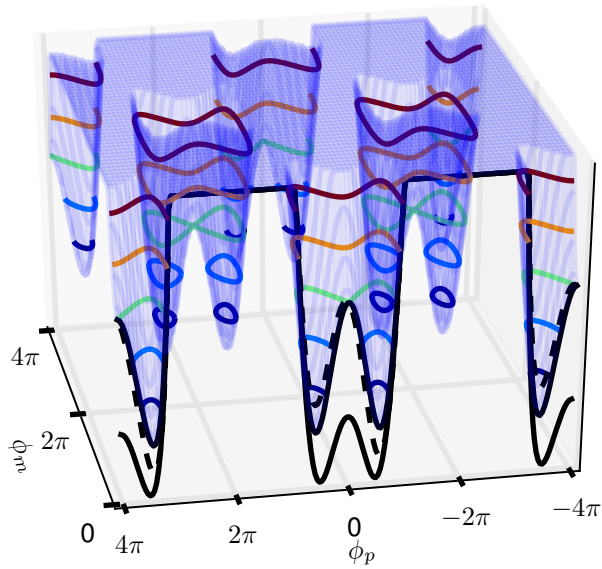


**Figure 2.1:** The potential landscape of the flux qubit according to Equation (2.10) for  $f = 0.5$  and  $\alpha = 0.8$ . The z-axis represents  $U_{pm}/E_j$ . Along the axis  $\Phi_p$  an effectively one-dimensional double well potential is formed. The two minima correspond to clockwise and counter-clockwise circulating persistent currents in the qubit loop. The lowered double well potential (black solid line) is for  $\alpha = 0.7$ . The black dashed line indicates the tilted potential for a frustration  $f = 0.51$ .

equation of motion, the Lagrangian  $\mathcal{L} = T - U$ , by considering the classical phases and their conjugate momenta as operators [OMT+99]. It reads

$$H = \frac{P_p^2}{2M_p} + \frac{P_m^2}{2M_m} + 2 + \alpha - 2 \cos(\phi_p/2) \cos(\phi_m/2) - \alpha \cos(2\pi f - \phi_p), \quad (2.12)$$

with the masses  $M_p = 2C(\Phi_0/2\pi)^2$  and  $M_m = 2C(1 + 2\alpha)(\Phi_0/2\pi)^2$ , and the momentum operators  $P_{p,m} = -\hbar \partial / \partial \phi_{p,m}$ .

The Hamiltonian (2.12) can be solved numerically. However, the tunnel rate between the wells can be also estimated using a tight-binding model [OMT+99]. At a frustration of  $f = 0.5$  it yields [FD10]

$$\Delta/2\pi \approx \frac{2E_j}{\sqrt{\alpha E_j/E_C}} e^{-0.15\sqrt{4\alpha(1+2\alpha)E_j/E_C}}. \quad (2.13)$$

The tunnel rate  $\Delta$  depends exponentially on the design parameters which makes the fabrication of identical flux qubits challenging. This rate corresponds to the Larmor frequency of the classical persistent current states, which oscillate as  $P(t) = (1 + \cos(2\pi\Delta t))/2$  (see Figure 2.2).

As mentioned before, the lowest two states can be treated as a two-level system, where the Hamiltonian in the persistent current basis  $\{\downarrow, \uparrow\}$  reads

$$\tilde{H}_q = \hbar \frac{1}{2} \epsilon \sigma_z + \hbar \frac{1}{2} \Delta \sigma_x, \quad (2.14)$$

where  $\sigma_z = |\uparrow\rangle\langle\uparrow| - |\downarrow\rangle\langle\downarrow|$ , and  $\sigma_x = |\uparrow\rangle\langle\downarrow| + |\downarrow\rangle\langle\uparrow|$ . The energy bias  $\epsilon$  is related to the frustration and corresponds to tilting the double well potential

$$\epsilon = 2I_p \left( \Phi - \frac{\Phi_0}{2} \right) / \hbar, \quad (2.15)$$

where  $\tilde{f} = \Phi - \frac{\Phi_0}{2}$  corresponds to the frustration used in the remainder of the thesis. After diagonalization of  $\tilde{H}_q$ , the qubit in its energy basis  $\{|g\rangle, |e\rangle\}$  is expressed by the Hamiltonian

$$H_q = \frac{\hbar\omega_q}{2} \sigma_z, \quad (2.16)$$

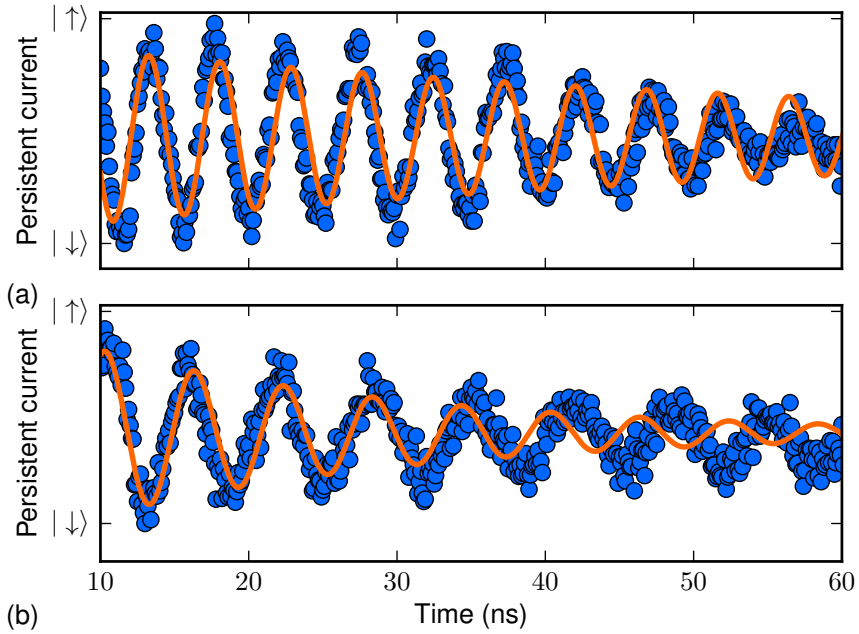


**Figure 2.2:** Experimental observation of the oscillations between clockwise and counter-clockwise persistent currents for (a)  $\Delta/2\pi = 200$  MHz and (b)  $\Delta/2\pi = 180$  MHz. The solid lines show fits to the damped oscillations  $P(t) \cdot \exp(-t/T_2)$  with  $T_2 = 62$  ns and  $T_2 = 34$  ns, respectively. The coupling  $\Delta$  decreases with increasing barrier. At a certain point the oscillation period approaches the dephasing time, thus showing the border between quantum and classical regime. A further increase of the barrier leads to a total destruction of the quantum phase between the persistent current states. As a consequence, the system is no longer regarded as quantum [FMF+11].

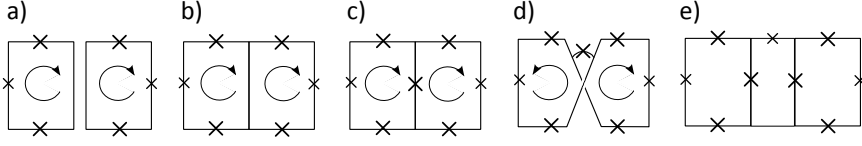


**Figure 2.3:** Various possibilities to couple flux qubits: (a) via geometric inductance, (b) with additional kinetic inductance over a shared line and (c) with additional Josephson inductance over a shared Josephson contact. All those designs feature anti-ferromagnetic coupling. The coupling can be made ferromagnetic by using the Josephson contact to effectively twist the lines (d) and tunable using a coupler loop (e).

where  $\sigma_z = |e\rangle\langle e| - |g\rangle\langle g|$ . The energy states are symmetric and antisymmetric superpositions of the persistent current states. In the symmetry point they are equal superpositions, whereas away from the symmetry point the ground state and excited state of the qubit correspond to one of the classical states.

The qubit frequency  $\omega_q/2\pi$  is set by

$$\omega_q = \sqrt{\Delta^2 + \epsilon^2}. \quad (2.17)$$

Such, the spectrum of the artificial two-level system follows a hyperbolic dependence on the magnetic frustration of the qubit loop.

### 2.1.3 Coupled qubits

#### Different coupling mechanisms

Flux qubits can be coupled straightforwardly by placing them next to each other. In the simplest configuration they couple through the geometric mutual inductance  $M_{\text{geo}}$  of their loops (see Figure 2.3 (a)). The qubit senses the magnetic flux generated from its neighbour effectively changing its energy bias and vice versa, thus the coupling type of such an arrangement is  $\sigma_z \sigma_z$ . Therefore, the interaction Hamiltonian between qubit  $i$  and  $j$  reads  $H_{qq}^{ij} = g_{qq}^{ij} \sigma_z^i \sigma_z^j$ . The current in each qubit screens the external magnetic flux. When the currents flow in the same direction, the neighbouring qubits have to screen less external flux. If the circulating currents had opposite directions, they would work against each

other, hence an anti-parallel orientation of the qubit fluxes is favoured. Consequently, the sign of the coupling energy  $g_{qq}^{ij} = \pm M_{qq} I_p^i I_p^j$  is positive corresponding to anti-ferromagnetic coupling.

Through different geometries varying types of coupling can be realized [Paa09]. For instance, ferromagnetic coupling is obtained by twisting the lines of the qubit loops (see Figure 2.3 (d)) [GIP+05]. Here, it is favourable for the currents to flow through the junction in the same direction, such leading to a parallel orientation of the qubit fluxes. The coupling strength can be significantly increased by sharing arms between the qubits, increasing the mutual inductance by the kinetic inductance (see Figure 2.3 (b)) and even further by placing an additional Josephson junction on the coupling line (see Figure 2.3 (c)). By using the Josephson inductance a remarkable qubit-qubit coupling of about 21 GHz has been demonstrated. The coupling in this system exceeds the level splitting by two orders of magnitude [GIP+05].

The coupling strength and type can also be modulated *in situ* using tunable couplers (see Figure 2.3 (e)). In this case the mutual inductance is provided by a coupling loop with embedded Josephson junctions. The inductance of this coupling loop depends on the Josephson inductance  $E_j$ , which can be tuned by an external magnetic field. A crossover from anti-ferromagnetic to ferromagnetic coupling has been demonstrated in such a system [PIB+07]. Spectroscopy of the tunable avoided level crossing between two qubits has also been shown [HRP+06].

### Weakly coupled qubit chains

In the following, a system of  $n$  qubits in anti-ferromagnetic configuration is analyzed. The Hamiltonian for  $n$  coupled qubits in the flux basis  $\{\downarrow, \uparrow\}$  reads:

$$H = \sum_{i=1}^n \tilde{H}_q^i + \sum_{i<j}^n H_{qq}^{ij} = \sum_{i=1}^n \hbar \frac{1}{2} (\epsilon_i \sigma_z^i + \Delta_i \sigma_x^i) + \sum_{i<j}^n \hbar g_{qq}^{ij} \sigma_z^i \sigma_z^j. \quad (2.18)$$

The first sum contains the contributions from the individual qubits and the second the interaction between nearest neighbours. In absence of the tunnel splitting  $\Delta_i$  the system corresponds to a classical Ising chain

[Paa09]. In order to study Hamiltonian (2.18), its spectrum is analysed numerically for different numbers of qubits  $n$  and positive coupling  $g_{qq}^{ij}$ .

First, a system of two coupled flux qubits is studied. The Hamiltonian (2.18) has four eigenstates which can be described by superpositions of the triplet states  $|\downarrow\downarrow\rangle$ ,  $1/\sqrt{2}(|\uparrow\downarrow\rangle + |\downarrow\uparrow\rangle)$ ,  $|\uparrow\uparrow\rangle$  and the singlet state  $1/\sqrt{2}(|\uparrow\downarrow\rangle - |\downarrow\uparrow\rangle)$  [SW03]. For very weak coupling, the first and second excited states of the coupled system are effectively degenerate at all times (see Figure 2.4 (a)). Therefore, there is no difference from the excitation spectrum of a single qubit. Even when one qubit is already excited, the transition frequency in order to excite the second one is identical to the first. Once the coupling is increased, it can be seen, that the coupling reduces the energy of the antiferromagnetic states and that the state  $1/\sqrt{2}(|\uparrow\downarrow\rangle - |\downarrow\uparrow\rangle)$ , i.e. the one with lower energy, is independent on the energy bias  $\epsilon$  (see Figure 2.4 (b)) [MPH+05]. Consequently, the energy of the first excited state is lowered (see Figure 2.4 (c)) compared to a single qubit. The effect of the coupling is strongest in the symmetry point. There, for a strongly coupled system, the transition frequencies to the second and third excited states are no longer identical to the transition frequency of the first excited state. Hence, the system becomes an effective 4 level system. Assuming qubit linewidths of tens of MHz, the coupling between the qubits becomes relevant when  $g_{qq} \gg 0.01 \cdot \Delta$ .

Next, the spectrum is analysed for a system with coupling  $g_{qq}^{ij} = 0.01 \cdot \Delta$  and an increasing number of qubits  $n$  (see Figure 2.5). The spectrum of a system of 6 coupled qubits is shown in Figure 2.5 (a). The number of eigenstates increases with  $2^n$ , which results in the appearance of band like structures. The width of the bands corresponds approximately to the coupling strength. However, the difference in the transition frequencies between the excited states is again small (see Figure 2.5 (b)). Therefore, the system behaves just like an ensemble of uncoupled qubits. This still holds while increasing the number of qubits  $n$ , where the transition frequency of the first excited state is slightly reduced compared to the single qubit case (see Figure 2.5 (c)).

For a in-depth discussion of strongly coupled qubit chains refer to [Paa09].

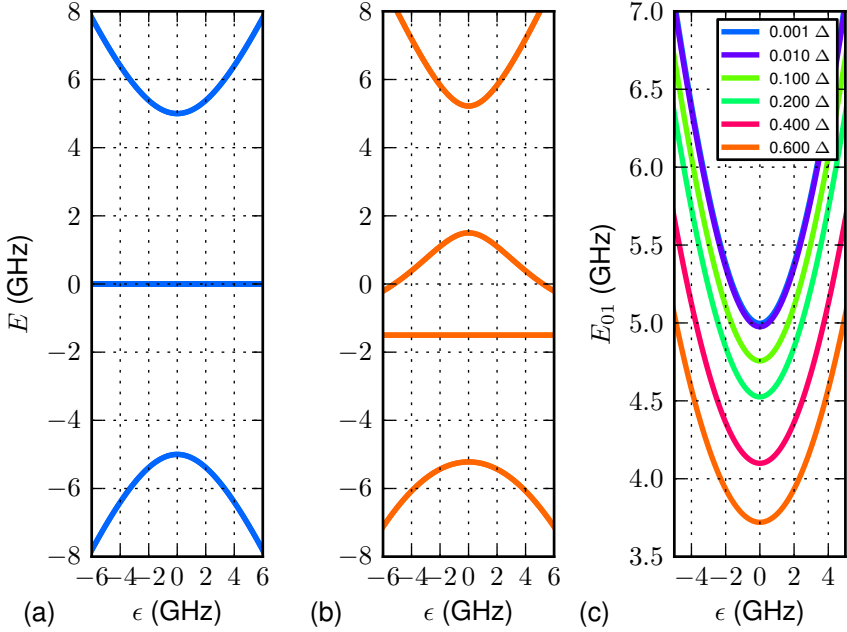


**Figure 2.4:** (a) The spectrum of two weakly coupled flux qubits  $g_{qq}^{ij} = 0.001 \cdot \Delta$ . The first and second excited state of the system are effectively degenerated. (b) Two qubits with a coupling of  $g_{qq}^{ij} = 0.6 \cdot \Delta$ . Now, the degeneracy is lifted. (c) The transition frequency between ground state and first excited state  $E_{01}$  in dependence on the qubit-qubit coupling.

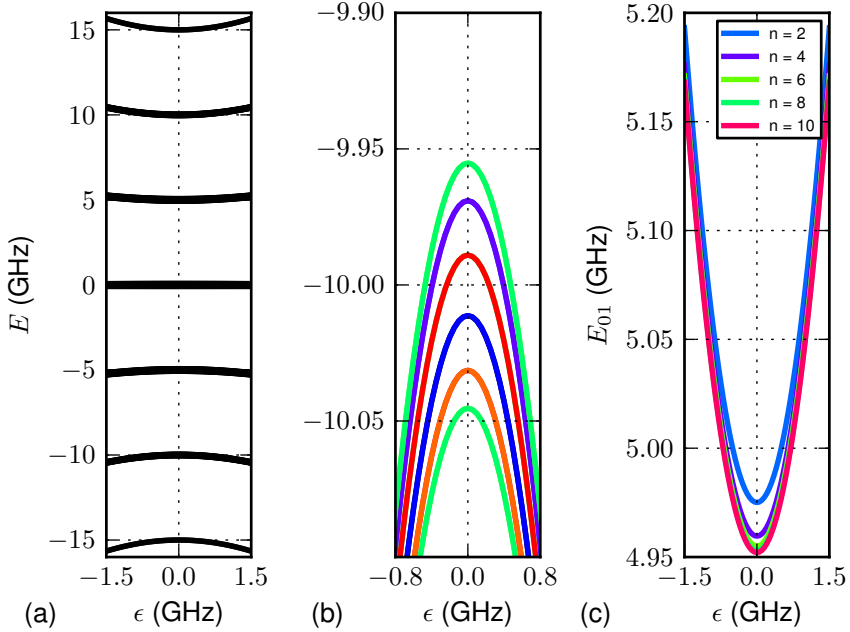


**Figure 2.5:** (a) The energy spectrum for a system of 6 coupled qubits with a coupling of  $g_{qq} = 0.01 \cdot \Delta$ . An energy-band like level structure is visible, however, the bands are only of the order of the coupling and therefore quite small. (b) The degeneracy between the excited states is lifted, (c) which leads to a decreasing transition frequency  $E_{01}$  with the number of qubits  $n$ .

### 2.2 Atoms and photons

Whereas it was a long time goal of cavity QED to couple the photon field of a cavity with a single atom, it was the starting point for circuit QED. This thesis is a first step towards further increasing the number of atoms, trying to break the dominating bottom-up approach regarding scalability of the field.

A superconducting qubit was analysed by the means of measuring a resonator for the first time by using the impedance measurement technique [IOI+03]. This approach relies on a high-quality resonator whose impedance is disturbed by the system to be analysed. Here, the system coupled to the resonator changes its effective inductance, thus leading to a shift of its resonance frequency. The resonator was formed by an LC circuit with a resonance frequency in the radio-frequency domain (of the order of MHz). Even at millikelvin temperatures such a resonator will not reach its ground state, as the energy of a single photon  $E_p = k_B 1 \text{ mK}$  is much less than the thermal noise from the environment. Therefore, the resonator acts as a classical field. When higher frequencies are used, the ground state of the cavity can be reached, i.e. experiments at single-photon levels are realized [WSB+04]. The two limiting cases of cavity QED are the weak coupling limit and the strong coupling limit. The strong coupling regime of cavity QED is reached, when the coherent coupling constant  $g$  exceeds the dissipation of the system [RBH01],  $g > [\Gamma, \kappa]$ , where  $\Gamma$  is the dephasing of the atoms and  $\kappa$  the photon loss rate of the cavity. For an optical cavity it was realized using the collective coupling [RTB+89]. The strong coupling regime between a transmission line resonator and a flux qubit was demonstrated in 2008 [AAN+08]. Recent experiments study effects which go beyond the physics described within the rotating wave approximation (RWA) in the so-called ultra strong coupling regime [BGA+09]; [NDH+10]. For instance, the counter-rotating terms produce a shift proportional to  $g^2/(w_q + w_r)$ , the Bloch Siegert Shift [BS40], which was observed in a system of a flux qubit and a lumped-element resonator at single photon level [FDLM+10]. For higher photon numbers a similar shift can be observed at a somewhat lower coupling [TSS+10].

This work studies systems close to the weak coupling limit, focusing on the interaction of photons and either a single qubit (see chapter 3)

or many qubits (see chapter 4). The model describing  $n$  mutually non-interacting qubits coupled to a photonic field is introduced in subsection 2.2.1. Subsequently, the system is analysed using a semiclassical approach (see subsection 2.2.2) in the resonant regime (see subsection 2.2.3). The section concludes with a brief discussion of the dispersive regime (see subsection 2.2.4).

### 2.2.1 The Tavis-Cummings model

The Tavis-Cummings Hamiltonian was named by Michael Tavis and Frederick W. Cummings who solved it directly in resonance [TC68]. It describes  $n$  mutually non-interacting qubits coupled to a bosonic mode.

The photon field in the resonator is characterized by the creation and annihilation operators  $a^\dagger$  and  $a$ . By neglecting the diagonal coupling term to the resonator, which is proportional to  $\sigma_z$ , as well as the non-resonant terms ( $a^\dagger\sigma_+$  and  $a\sigma_-$ ), where  $\sigma_\pm = (\sigma_x \pm i\sigma_y)/2$ , the Tavis-Cummings model reads [TC68]

$$H = \hbar\omega_r a^\dagger a + \sum_{j=1}^n \left( \frac{\hbar\omega_{q,j}}{2} \sigma_z^j + \hbar g_{\epsilon,j} (\sigma_+^j a + \sigma_-^j a^\dagger) \right), \quad (2.19)$$

where

$$g_{\epsilon,j} = g \frac{\Delta_j}{\omega_{q,j}} \quad (2.20)$$

is the transversal coupling strength between qubit  $j$  and the resonator. Until now, it has been diagonalized for up to 3 atoms. However, the total number of excitations  $n_{tot}$  commutes with the Hamiltonian (2.19), which allows the diagonalization within the manifold of a constant excitation number [Bre09]. Such, the Hamiltonian can be analysed in the single excitation basis  $\{|0ggg \dots\rangle, |1ggg \dots\rangle, |0egg \dots\rangle, |0geg \dots\rangle, |0gge \dots\rangle, \dots\}$ . Assuming identical qubits, the diagonalization results in two eigenstates, which are coherent superpositions of the basis states with the eigenenergies of [Bre09]

$$E_\pm = \hbar \frac{\omega_r + \omega_q}{2} \pm \frac{1}{2} \sqrt{(\omega_r - \omega_q)^2 + 4g_\epsilon^2 n}. \quad (2.21)$$

Interestingly, these correspond to the eigenstates of the Jaynes-Cummings Hamiltonian, which describes the interaction of a single atom and a cavity, where  $n$  corresponds to the number of photons  $N$  [BHW+04]. When  $n = 1$  and  $N = 0$ , the eigenstates of the Tavis-Cummings and Jaynes-Cummings Hamiltonians are identical. Here, the separation between the two states in resonance  $\omega_r - \omega_q = 0$  scales with the number of atoms  $\sqrt{n}$ , which is referred to as collectively enhanced coupling.

In order to describe the experiments, a driving field is necessary which accounts for the probe signal with frequency  $\omega_d/2\pi$  and driving strength  $f$ . The driving term  $\hbar f \cos(\omega_d t)(a + a^\dagger)$  is added to Hamiltonian (2.19). Subsequently, the Tavis-Cummings Hamiltonian (2.19) is transformed in the rotating frame of the driving frequency  $\omega_D/2\pi$  by using the unitary operator

$$U = e^{i\omega_d(a^\dagger a + \frac{1}{2} \sum_i^n \sigma_z^i)t} . \quad (2.22)$$

The new Hamiltonian follows from  $H = U^\dagger H U - \hbar\omega_d(a^\dagger a) + \frac{1}{2} \sum_i^n \sigma_z^i$  as

$$\tilde{H} = \hbar\delta_{rd}a^\dagger a + \sum_{j=1}^n \left( \frac{\hbar\delta}{2} \sigma_z^j + \hbar g_{\epsilon,j} (\sigma_+^j a + \sigma_-^j a^\dagger) \right) - \frac{\hbar f}{2} (a + a^\dagger) , \quad (2.23)$$

where the detunings  $\delta_{rd} = \omega_r - \omega_d$  and  $\delta = \omega_{q,j} - \omega_d$  are introduced.

In order to account for the coherence of the system, the Markovian Master equation, the equation of motion for the density matrix  $\rho$ ,

$$\dot{\rho} = \frac{1}{i\hbar} [\tilde{H}, \rho] + L[\rho] , \quad (2.24)$$

is introduced, where the dissipative Lindblad term  $L = L_r + L_q$  presents the photon loss with rate  $\kappa$  of the resonator ( $L_r$ ) as well as the relaxation  $\Gamma_\psi$  and dephasing  $\Gamma_\varphi$  of the qubit ( $L_q$ ). The steady state solutions  $\dot{\rho} = 0$  can be numerically calculated. It was shown that the full-quantum mechanical treatment gives the same results as the semiclassical treatment [Rei12]. The semiclassical ansatz allows for an analytical solution. Therefore, the main results of the thesis will be analysed using the semiclassical treatment, which is discussed in the following subsection.

### 2.2.2 Semiclassical treatment

The time evolutions of the expectation values of  $a$  and  $\sigma_-$  are [Rei12]

$$\langle \dot{a} \rangle = - \left( i\delta_{rd} + \frac{\kappa}{2} \right) \langle a \rangle - \sum_{j=1}^n ig \langle \sigma_-^j \rangle + \frac{if}{2}, \quad (2.25)$$

$$\langle \dot{\sigma}_-^j \rangle = - (i\delta + \Gamma_\varphi) \langle \sigma_-^j \rangle + ig \langle \sigma_z^j a \rangle. \quad (2.26)$$

It is assumed that all average values factorize, e.g.  $\langle \sigma_z^j a \rangle = \langle \sigma_z^j \rangle \langle a \rangle$ . For a weakly driven system follows  $\langle \sigma_z^j a \rangle = -\langle a \rangle$ , which means that the atoms are not excited by the drive signal and remain in their ground states.

Such,  $\sigma_-^j$  in Equation (2.25) can be replaced for the steady case  $\dot{\sigma}_-^j$  from Equation (2.26) and the equation of motion for  $\langle a \rangle$  follows

$$\langle \dot{a} \rangle = \left( - \left( i\delta_{dr} + \frac{\kappa}{2} \right) + \sum_{i=1}^n \frac{g_\epsilon^2}{\Gamma_\varphi + i\delta} \right) \langle a \rangle + \frac{if}{2}. \quad (2.27)$$

In the case of a steady state  $\langle \dot{a} \rangle = 0$  for a system driven directly at the resonance frequency of the resonator  $\delta_{dr} = 0$  follows

$$0 = \left( \frac{\kappa}{2} - \sum_{j=1}^n \frac{g_\epsilon^2}{\Gamma_\varphi + i\delta} \right) \langle a \rangle + \frac{if}{2}. \quad (2.28)$$

From now on, the detuning  $\delta$  refers to the detuning between qubit and resonator frequency. In the case of  $n$  identical qubits in Equation (2.28) the sum can be replaced by a product. This leads to an analytically solvable equation for  $\langle a \rangle$ . The observable measured in the experiment corresponds to the expectation value of  $\langle a \rangle$ . Later on, the phase of the measured signal will be analysed, which can be found as

$$\tan \varphi = \frac{\Im \langle a \rangle}{\Re \langle a \rangle}. \quad (2.29)$$

Separating imaginary and real part of  $\langle a \rangle$  from Equation (2.28) yields

$$\tan \varphi = \frac{-2ng_\epsilon^2\delta}{\kappa(\Gamma_\varphi^2 + \delta^2) + 2ng_\epsilon^2\Gamma_\varphi}. \quad (2.30)$$

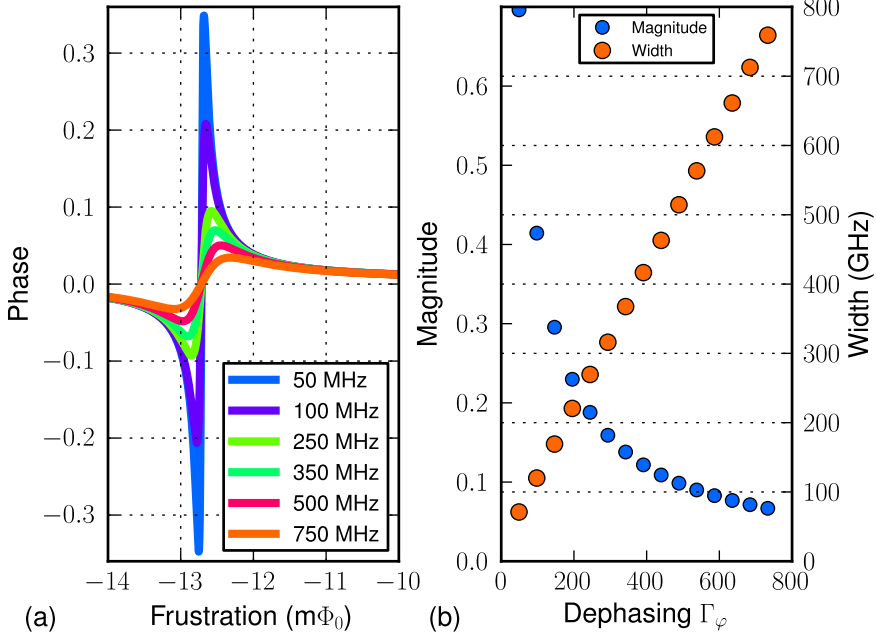


**Figure 2.6:** (a) The dependence of the resonant phase shift transmitted at the resonance frequency of a resonator coupled to 5 identical qubits for different dephasing rates  $\Gamma_\varphi$ . (b) The magnitude and the width of the resonant phase shift in dependence on the dephasing rate  $\Gamma_\varphi$  as extracted from (a).

The parameter tuned during the experiment is the qubit-resonator detuning  $\delta$ . The transversal coupling  $g_{\epsilon,j}$  changes correspondingly with the qubit frequency, yet is otherwise fixed by the bare coupling  $g$ . The behaviour of the phase shift tuned over a qubit-resonator resonance in dependence on the dephasing  $\Gamma_\varphi$  and the number of qubits  $n$  is studied in the following.

### 2.2.3 Analysis of the resonant behaviour

In the experiments discussed in chapter 4, the resonator is weakly probed directly at its resonance frequency. The frustration  $\Phi$  of the qubit system is the main parameter to be varied. It sets the qubit frequency  $\omega_{q,j}/2\pi$

according to Equation (2.17). Here, the interest lies on the resonant interaction between the qubit system and the resonator, which is centrally symmetric in respect to the degeneracy point. In order to understand the behaviour of the system in different parameter ranges, the phase transmitted directly at the resonator frequency  $\omega_r/2\pi$  is analysed in detail in the vicinity of a resonant mode between the qubit system and the resonator by using the semiclassical Equation (2.30). When crossing such a resonance in dependence on the frustration, the phase shifts to negative values relative to its off-resonant value. In the case of crossing the resonance from lower frequencies, the phase reappears from positive values, which is due to a jump of the phase at the resonance.

The dependence of the shape of the resonant phase shift on the dephasing rate  $\Gamma_\varphi$  (see Figure 2.6 (a)) is of great interest. Further it yields: the higher the dephasing rate  $\Gamma_\varphi$ , the lower the magnitude of the phase signal, scaling approximately with  $1/\Gamma_\varphi$  (see Figure 2.6 (b)). The peak-to-peak width of the phase shift, defined as the distance in the qubit energy from minimum to maximum of the phase signal, behaves linearly with the dephasing rate  $\Gamma_\varphi$ . Note, that the width of the resonant phase shift is almost completely given by the dephasing rate, the small remaining offset arrives from the number of qubits  $n$ .

Next, the dependence of the resonant phase shift on the number of qubits  $n$  is analysed (see Figure 2.7 (a)). Obviously, the magnitude increases with the number of qubits. Yet, it is important to note, that it scales linearly with  $n$  for small qubit numbers, but not with  $\sqrt{n}$  (see Figure 2.7 (b)). The width of the resonant mode depends only very weakly on the number of qubits  $n$ . An increase of about 40 MHz occurs between 1 and 10 qubits. Therefore, it can be concluded, that the width is given by the dephasing rate  $\Gamma_\varphi$ , whereas the magnitude results from a product of the number of qubits  $n$  and dephasing rate  $\Gamma_\varphi$ . Out of the resonance  $\delta > \Gamma_\varphi$ , the remaining dispersive phase shift is dominated by the number of qubits  $n$ . In consequence, for not too many qubits,  $n$  and  $\Gamma_\varphi$  are independent of one another in certain regions.

In an authentic experiment not all qubits will be identical. Therefore, it is important to study the conditions in which collective resonant modes are formed. In Figure 2.8 the behaviour of three non-identical qubits equally coupled to a single cavity is analysed. The qubits possess the same

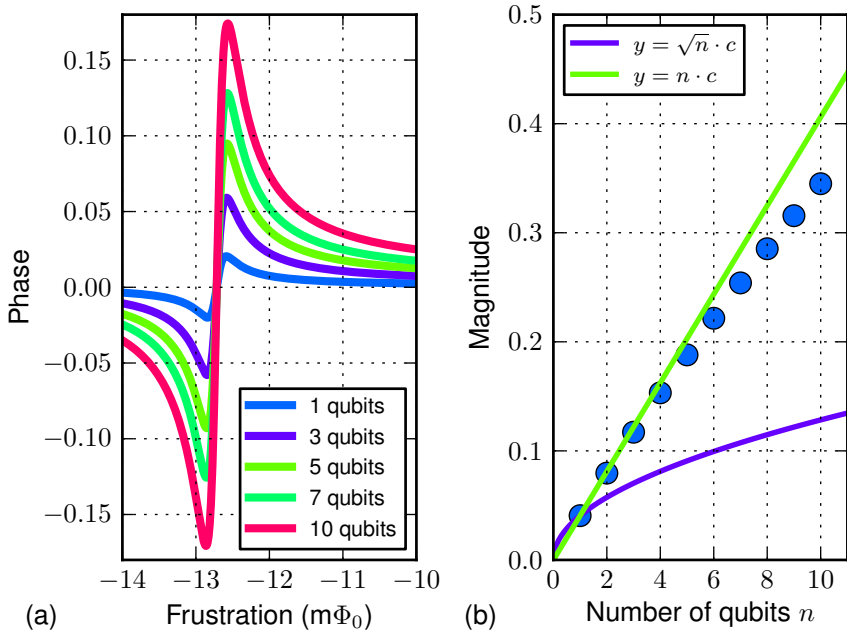


**Figure 2.7:** The resonant mode in dependence on the number of qubits  $n$ . Panel (a) shows the resonant phase shift for an increasing number  $n$  of identical qubits, whereas their magnitude is extracted in (b). Here, the solid lines show the expectation if the magnitude is enhanced either linearly or by  $\sqrt{n}$ .

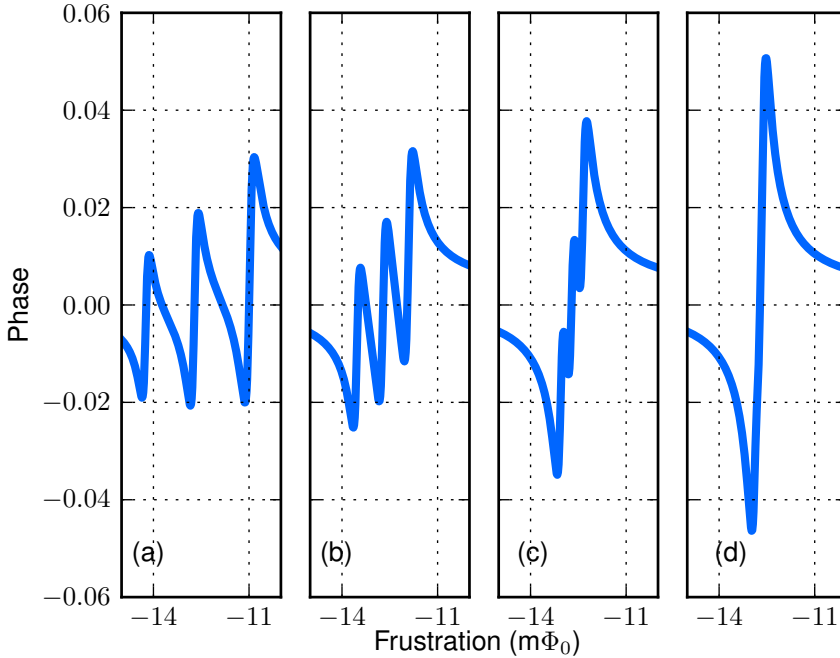


**Figure 2.8:** Three qubits with different detunings between each other. In panel (a) the detuning of the two outer qubits relative to the middle qubit at its resonance to the resonator is  $\delta_{qq} = 13 \cdot \Gamma_\varphi$ . Three individual phase shifts are visible. In panel (b) the detuning is reduced to  $\delta_{qq} = 6.5 \cdot \Gamma_\varphi$ . In panel (c), for a detuning of  $\delta_{qq} = 3.25 \cdot \Gamma_\varphi$ , the phase shifts merge, yet the resonances of each qubit are distinguishable. Once the detuning equals the dephasing  $\delta_{qq} = \Gamma_\varphi/2\pi$ , the three qubits form a collective resonant mode (see panel (d)). Please note, that the curves shown here were calculated numerically from Equation (2.27).

persistent current, but different gaps  $\Delta_j$ . Relative to the center qubit 1, both outer qubits 0 and 2 feature a lower and a higher gap, respectively. The detuning of qubits 0 and 2 at the resonance to the resonator  $\omega_{q,1} = \omega_r$ ,  $\delta_{qq} = |\omega_{q,1} - \omega_{q,(0,2)}|$  is the parameter varied between the panels. For a detuning  $\delta_{qq} = 13 \cdot \Gamma_\varphi$  the qubits form independent resonant modes (see Figure 2.8 (a)). The different peak-to-peak magnitudes of the resonant phase shifts result from the different effective coupling  $g_\epsilon$  which depends on the qubit-resonator detuning  $\delta_{qr}$ . When  $\delta_{qq}$  is reduced, the shape of the phase shift is altered, yet the qubits still act independently (see Figure 2.8 (b)). Once  $\delta_{qq}$  reaches the order of the dephasing  $\Gamma_\varphi$ , the magnitude of the phase shift is enhanced and the three individual modes appear almost as one single resonant mode (see Figure 2.8 (c)). Note, that  $\Delta_0$  and  $\Delta_2$  are 360 MHz detuned. A single collective resonant mode with maximum magnitude is formed in the case, that the detuning is equal or less than the dephasing  $\Gamma_\varphi$  (see Figure 2.8 (d)). Here, the spread in the gaps of the qubits is still allowed to be in the range of 100 MHz.

### 2.2.4 Dispersive regime

If the qubits and the resonator are detuned from each other,  $\delta > g_\epsilon, \Gamma_\varphi$ , no energy exchange will occur between them. Still, the coupling is present and therefore resonator and qubit influence each other dispersively. The effects become visible when transforming the Tavis-Cummings Hamiltonian (2.19) to [ZRK+09]:

$$\begin{aligned}
 H_{disp} = \hbar \left( \omega_r + \sum_{i=1}^n \frac{g_\epsilon^2}{\delta_j} \sigma_z^i \right) a^\dagger a + \sum_{i=1}^n \frac{\hbar}{2} \left( \omega_{q,i} + \frac{g_\epsilon^2}{\delta_j} \right) \sigma_z^i + \\
 + \hbar \sum_{i>j}^n J_{ij} \left( \sigma_-^i \sigma_+^j + \sigma_+^j \sigma_-^i \right). \tag{2.31}
 \end{aligned}$$

Here, a Haussdorff expansion to second order in the small parameter  $\lambda_i = g_{\epsilon,i}/\delta_i$  with the generator  $S = \exp(\sum_i \lambda_i \sigma_-^i a^\dagger - \sigma_+^i a)$  has been applied to Hamiltonian (2.19) [BGW+07]. The last term in the dispersive

Hamiltonian  $H_{disp}$  reveals a direct interaction between the qubits with a coupling strength of

$$J_{ij} = g_{\epsilon,i} g_{\epsilon,j} \left( \frac{1}{\delta_i} + \frac{1}{\delta_j} \right). \quad (2.32)$$

In principle, this can be used to couple the qubits dispersively over the resonator [MCG+07]. However, the effect is inverse proportional to the qubit-resonator detuning, which reduces the off-resonant coupling significantly in the multi-qubit system presented in chapter 4. In the case of ultra-strong coupling, when the counter-rotating terms have to be taken into account, the effective qubit coupling will change qualitatively to the Ising type [ZRK+09].

The first term in  $H_{disp}$  shows that the cavity frequency acquires a shift which depends on all qubits  $\sum_{i=1}^n \frac{g_{\epsilon}^2}{\delta_j} \sigma_z^i$  and their states. This dispersive shift of the resonator frequency is called AC-Stark, or in this case, AC-Zeeman shift, because the coupling is based on magnetic interaction. In this thesis, it will be referred to as dispersive shift. It will be analysed experimentally for a single qubit (see subsection 3.2.2) and for a multi-qubit system (see subsection 4.2.3).

Analogously, as revealed by the second term in  $H_{disp}$ , the qubit transition frequencies are individually shifted by  $2g_{\epsilon}^2/\delta$  per cavity photon. For zero photons this corresponds to the so-called Lamb shift induced by the vacuum fluctuations, whereas it is called AC-Zeeman shift in the case of  $N$  photons. The linear dependence on the photon number  $N$  will be demonstrated for a single qubit in subsection 3.4.2. Using the AC-Zeeman shift, the qubit energies can be tuned, which will be applied to the multi-qubit system in a sophisticated way (see subsection 4.4.2).



### 3 Dressed state amplification

*One of the unique features of circuit QED compared to cavity QED is that all parameters of the system can be defined in a precise way and that the number of atoms is constant. For superconducting qubits coupling a single atom to a cavity is common [BHW+04], whereas it has been a big achievement in cavity QED [RBH01]. In this chapter, the focus lies on a system containing a single qubit embedded into a high-Q cavity on the edge of the strong coupling regime. For flux qubits, the regime  $g > \kappa$  is readily achieved as this depends mainly on the photon loss rate  $\kappa$  of the resonator and the coupling  $g$  between qubit and resonator which can be controlled by design. The coupling between qubit and resonator and the resulting avoided level crossing is observable regardless of the coherence of the qubit [OPM+10]. The regime  $g > \Gamma_{\downarrow}$  is also easily achievable for flux qubits, yet the dephasing time of flux qubits degrades quickly when biased away from the symmetry point. The dephasing rate  $\Gamma_{\varphi}$  typically exceeds 100 MHz outside the degeneracy point. In order to be truly in the strong coupling regime  $g > \Gamma_{\varphi}, \kappa$  the coupling needs to exceed  $\Gamma_{\varphi}$ , which can be achieved either by coupling the qubit at its symmetry point [FFM+10], thus minimizing  $\Gamma_{\varphi}$ , or by increasing  $g$  [FDLM+10]. In this work,  $g$  is of the order of and even less than  $\Gamma_{\varphi}$ . This bears the advantage that the system can be strongly driven without the avoided level crossing to be the dominating effect.*

*In the first part of this chapter, section 3.1, the sample design is outlined briefly and the measurement setup is discussed in detail. Subsequently, in section 3.2, the experiments performed on the interaction of a single qubit and a resonator are presented. Along the way the measurement setup which has been used throughout this thesis, unless noted differently, is introduced. The system is characterized using spectroscopic and ground state measurements. A similar set of experiments will be used later on to reconstruct the parameters of the multi-qubit sample. The coherence of the qubit is estimated from the spectroscopy peak. Afterwards, the temperature*

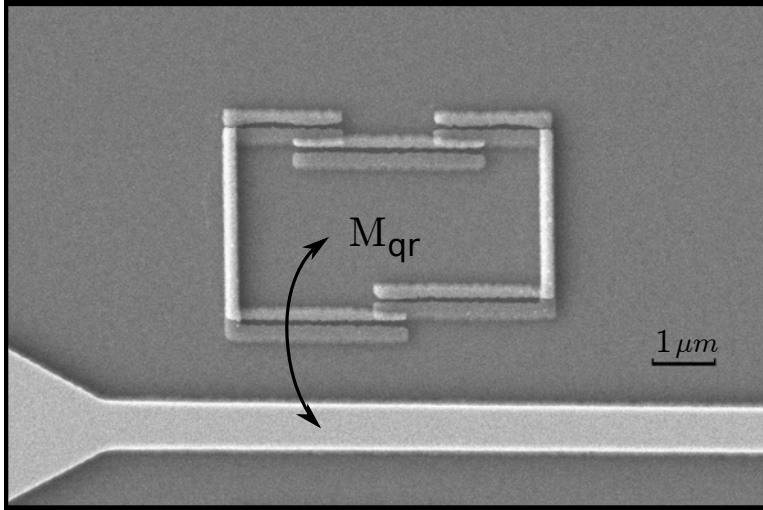


**Figure 3.1:** A scanning electron micrograph of the sample showing the central part of the coplanar waveguide resonator where the qubit is situated. The qubit is coupled to the resonator by the mutual inductance  $M_{qr}$ .

*dependence of the system is reported (see section 3.3). In section 3.4 the possibilities of tuning the parameters of the qubit through dressing the states with an additional photon field are investigated and the main result of these experiments, the demonstration of amplification directly at the Rabi frequency of the driven qubit, is shown [OMA+13].*

## 3.1 The sample and experimental setup

The sample consists of a single qubit coupled to a coplanar waveguide resonator (CPWR). Its geometry and design are presented in subsection 3.1.1. In this thesis, steady state transmission experiments of the resonator-qubit systems are performed. The measurement setup used throughout this thesis is outlined in subsection 3.1.2.

### 3.1.1 The sample

The sample consists of a CPWR containing a single flux qubit. An electron micrograph of the qubit next to the central line of the resonator is shown in Figure 3.1. The length of the resonator's central line is 23 mm, its width is  $50 \mu\text{m}$ , and the gap between the central line and the ground plane is  $30 \mu\text{m}$  resulting in a wave impedance of  $50 \Omega$ . In the middle of the resonator the central line is tapered to a width of  $0.8 \mu\text{m}$  for a length of  $30 \mu\text{m}$  with a  $9 \mu\text{m}$  gap which provides better qubit-resonator coupling and a small impedance mismatch to detune the harmonics of the resonator. The separation between the multiple of the fundamental mode frequency and the third harmonic is about 25 linewidths. Otherwise, the properties of the resonator remain unchanged, as the tapered section is much smaller than the wavelength. The symmetric gap capacitors have a width of  $90 \mu\text{m}$ , putting the resonator in the undercoupled regime. The fundamental mode frequency is  $\omega_{r,1}/2\pi = 2.59 \text{ GHz}$  with a linewidth of only  $\kappa_1/2\pi = 21.5 \text{ KHz}$  (see Figure 3.2 (a)). The quality factor is  $Q_1 = \omega_{r,1} / \kappa_1 = 1.2 \cdot 10^5$ . The inductance of the resonator is calculated using finite element electromagnetic simulation on the complete geometry of the resonator and is found to be  $L_r = (11.0 \pm 0.4) \text{ nH}$ .

The resonator was fabricated by e-beam lithography, which guarantees an accurateness of the dimensions of better than  $0.2 \mu\text{m}$ . After exposure of the resist, the  $200 \text{ nm}$  thick niobium film deposited on a high-resistivity silicon substrate was patterned by  $\text{CF}_4$  reactive-ion etching. The three-junction flux qubit was deposited in a second step at the center of the resonator using conventional two-angle shadow evaporation technique [Dol77].

The coupling between the resonator and the qubit is purely inductive and can be either calculated numerically or analytically, see subsection 4.1.2 for details of the procedure. The mutual inductance is  $M_{qr} = (0.92 \pm 0.02) \text{ pH}$ .

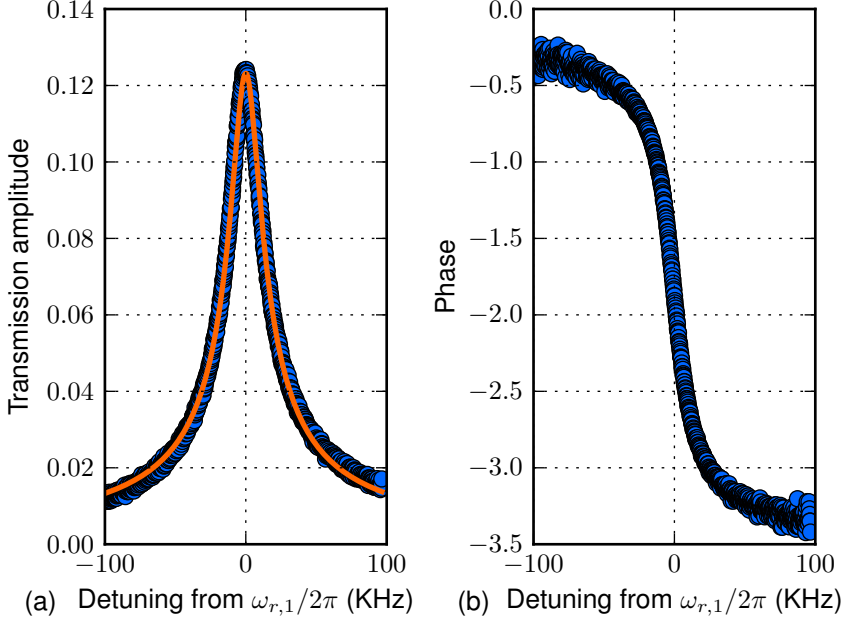


**Figure 3.2:** The properties of the resonator. The transmitted amplitude (a) and phase (b) around the fundamental mode frequency  $\omega_{r,1}/2\pi$ . The solid line shows the Lorentzian fit, which is used to extract the resonator parameters.

#### 3.1.2 Experimental setup

##### Cryogenic environment

In the experiments presented here, low temperatures are needed for two reasons. Firstly, the working principle of the flux qubit is based on superconductivity. The qubit is made of aluminium with a critical temperature of  $T_c \approx 1.2$  K. For the circuit to work in a stable regime a temperature below the critical temperature must be reached, where all quasi particle effects are saturated. This temperature typically is  $T_c/10$ . The superconducting resonators are made of niobium with  $T_c \approx 9$  K.

Secondly, the reason why even lower temperatures are necessary evolves from the quantum nature of the objects of interest. The resonators

used in the different experiments feature a fundamental mode frequency of about 2.5 GHz which corresponds to a temperature of 120 mK. In order to reach the ground state of the resonator the temperature of the environment must be less than the eigenenergies of the system. Natural quantum systems are only weakly coupled to the environment and do not require this condition in order to reach the ground state. Yet, superconducting qubits as macroscopic quantum systems are easily thermalized making a sufficiently low temperature necessary to reach the ground state. Interestingly, with increasing coherence times of superconducting qubits [PSB+11]; [RGP+12], additional tools have to be applied in order to reach the ground state in a reasonable time [RJH+10]; [GLP+13]. Once the system is in its ground state, the coherence times of qubits depend only weakly on temperature [LLA+07], which is consistent with the report that low-frequency noise seems to be temperature independent [YBG+12]. However, not only the superconducting qubits will be in their ground state, but also other quantum mechanical systems with similar level splitting will relax to a lower quantum state, resulting in additional loss mechanisms for superconducting qubits [MCM+05] and resonators [MPO+10]. Ubiquitous microscopic two level systems influence the properties of qubits and resonators at low temperatures. They have also been reported to be present in flux qubits [GYB+12]; [LBD+09].

In order to reach millikelvin temperatures the samples are installed on the mixing chamber stage of a dilution refrigerator. The base temperature of the dilution refrigerator is about 10 mK and the cited cooling power at 100 mK is about 400  $\mu$ W. The left hand side of Figure 3.3 shows the design drawing of the system used throughout this thesis, indicating the different temperature stages, installed microwave elements (cables are not shown) and sample holders. The numbers in brackets refer to the designations in Figure 3.3. The essential elements of the dilution unit are the condensing line, in which the mixture of He-3 and He-4 is pre-cooled in the 1 K bath (3), and heat exchangers at the different temperature stages. The mixing chamber (7) is the place where the two phases - one with He-3 diluted phase of super-fluid He-4 and one of pure He-3 - are separated. He-3 is pumped through the still (5), which is typically heated up to 600 mK. Three complete test setups are installed consisting of input lines, sample holders (9, 10 and 12) and output lines with

cryogenic circulators (6,8) at the 20 mK and 50 mK stage and cryogenic high-electron-mobility transistor (HEMT) amplifiers (1, 2) at the 1.6 K and 4 K stage. The samples are magnetically shielded by one or two cryoperm shields, which allows for a cool down of the sample in near zero magnetic field. Any remaining magnetic field is frozen by an additional superconducting lead shield. For thermometry the cryostat control unit is used, which has been verified by a calibrated RuO<sub>2</sub> thermometer. The external magnetic field for the qubits is provided by two superconducting coils for each setup made of 400 turns of niobium titanium wire on PVC cylinders with a diameter of 0.5 cm. A Keithley 2600 serves as differential current source.

#### **Microwave setup**

The right hand side of Figure 3.3 provides an overview of the microwave setup. The room temperature (RT) part and the input lines are the same for all measurement setups. The probe signal from port 1 of a network analyzer is combined with a second tone from a microwave generator and attenuated subsequently. The input lines are additionally attenuated at the 1 K pot stage (4) and the mixing chamber stage (11) with 20 dB each in order to thermalize the line and to prevent room temperature noise from reaching the sample. The dissipation at the last attenuator limits the power which can be applied at the input of the sample. If it exceeds the cooling power of the refrigerator the system will start warming up. Three sample holders are installed, two of them (9, 10) hold an approximately 3 cm long rectangular copper box. This sample compartment contains the chips studied in this thesis. The chips are placed directly in the sample compartment without using a printed circuit board (PCB). Directly below the chip, there is a cut-out to ensure the microwaves travel mainly in the substrate of the chip. On both ends, the input and the output line of the chips are connected to the pins of the connectors to the microwave cables using silver conductive grease. A third sample holder (12) for the round sample holder design from Karlsruhe contains smaller chips connected to a PCB. The output lines consist of flexible superconducting aluminium cables leading to circulators either at the 20 mK (8) or 50 mK (6) stage. Superconducting niobium cables connect the circulators to the cryogenic

### 3.1 The sample and experimental setup

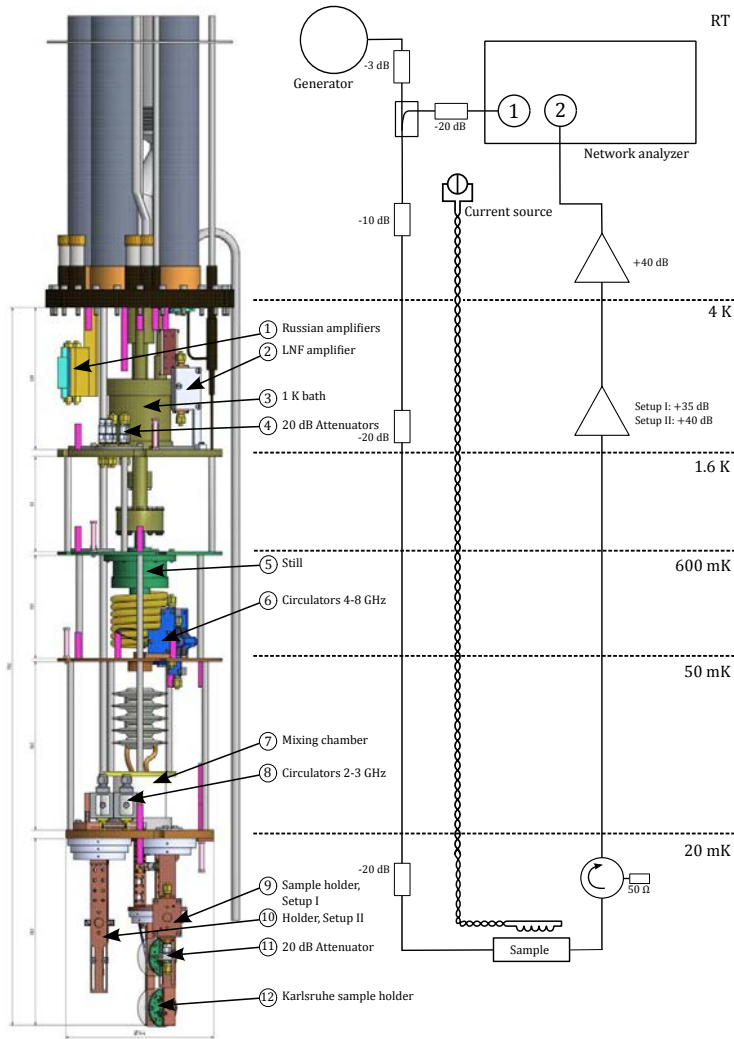


**Figure 3.3:** Sketch of the experimental setup used throughout this thesis. A design drawing (by Thomas Wagner *et al.*) of the dilution refrigerator is shown on the left hand side. The microwave setup is shown on the right hand side. For a complete description of the system, please refer to the main text.

HEMT amplifiers. Measurement setup I uses an amplifier (1) with a noise temperature of about  $T_n = 14$  K, a gain of 35 dB and a circulator with a bandwidth of 2-3 GHz. This measurement setup has been implemented twice. Measurement setup II utilizes an amplifier from Low Noise Factory (LNF) (2) with a noise temperature of about  $T_n = 5.4$  K, a gain of 40 dB and two circulators from Channel Microwave with a bandwidth of 4-8 GHz. The working frequency band is the main difference between the two measurement setups. The returning signal is further amplified at room temperature before reaching port 2 of the network analyzer. In the experiments the forward transmission coefficient  $S_{21}$  is measured. Figure 3.2 shows the phase and amplitude of the  $S_{21}$  parameter in dependence on the frequency around the fundamental resonance of the CPWR. The transmission is maximal directly in resonance and follows a Lorentzian line shape. In the following experiments, the transmission is always probed directly at the resonance of the resonator. There, the phase signal is most sensitive to changes of resonator properties like its resonance frequency. If the resonator's frequency is shifted due to a change of the system, this can be observed as a phase shift in the transmitted signal.

## 3.2 A single qubit and a resonator

In the first part of this section, the results of a two-tone spectroscopy on a single flux qubit are presented (see subsection 3.2.1). Here, the resonator is monitored continuously while a second tone probes the transition frequency of the qubit. In combination with a measurement of the resonator-qubit system in its ground state, which results in the so-called dispersive shift, all parameters of the sample are determined (see subsection 3.2.2). In the end, the dephasing time of the qubit is estimated from the linewidth of the spectroscopy peak (see subsection 3.2.3).

### 3.2.1 Spectroscopy

The phase of the transmitted signal, measured as a function of the qubit's level spacing, exhibits a dip in the vicinity of the degeneracy point, when the minimal transition frequency of the qubit, the gap  $\Delta$ , is above the en-

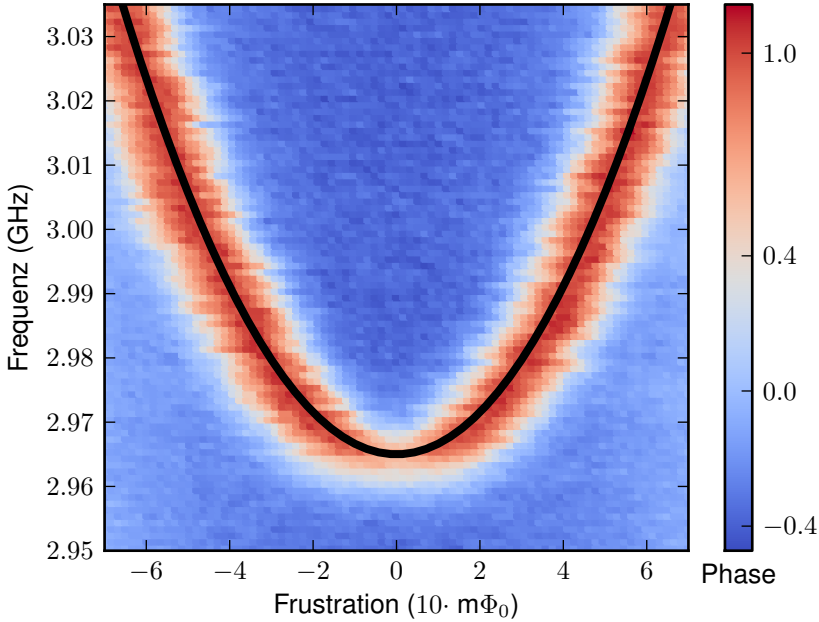


**Figure 3.4:** The spectrum of a single flux qubit around its symmetry point. The frequency of a strong excitation tone is swept while the phase at the probe frequency is continuously monitored. The solid line shows a fit to the hyperbolic qubit spectrum with the parameters  $\Delta = 2.96$  GHz and  $I_p = 158$  nA.

ergy of the resonator. This dip, originated from the shift of the resonance frequency of the resonator-qubit system, is usually called a dispersive shift. Moreover, this shift depends on the state of the qubit. Therefore, the level spacing of the qubit can be identified by performing a two-tone spectroscopy experiment. In practice, the resonator is continuously probed at the fundamental mode frequency  $\omega_{r,1}/2\pi$  and a second microwave tone is directly applied to the input of the resonator. When the second microwave tone and the qubit are in resonance, the population of the qubit is changed and a peak is observed in the signal of the transmitted phase. Figure 3.4 shows the spectrum around the symmetry point. The solid line is a fit to the hyperbolic qubit spectrum from which the

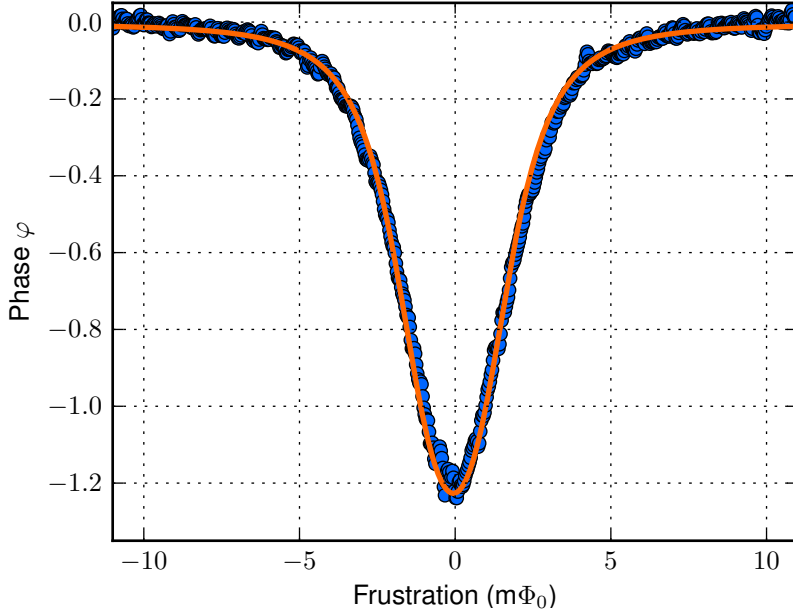


**Figure 3.5:** The dispersive shift of the transmitted phase through the resonator at the fundamental mode frequency in dependence on the frustration of a single qubit. The solid line shows a fit according to Equation (3.1).

parameters  $\Delta = 2.96$  GHz and  $I_p = 158$  nA are extracted. From this the coupling to the fundamental mode follows to be  $g_1 = (2.7 \pm 0.2)$  MHz.

### 3.2.2 Ground state measurement

Here, the probe signal is the only tone applied. The phase of the transmitted signal is measured in dependence on the qubit frustration (see Figure 3.5). As said before, the system is in the fully dispersive regime  $\Delta > \omega_{r,1}$ , where a dip is observed, which corresponds to a shift of the cavity frequency. It depends on the detuning between qubit and resonator

frequency  $\delta = \omega_q - \omega_r$  and the transversal coupling  $g_\epsilon$ . The dispersive shift for a single flux qubit coupled to a resonator follows

$$\tan \varphi = -\frac{2g_\epsilon^2}{\kappa\delta}. \quad (3.1)$$

From fitting the observed dispersive phase shift to Equation (3.1), the coupling between qubit and resonator can be extracted. The best fit is obtained for  $g = 3$  MHz (see solid line in Figure 3.5). This experimental value and the expected one are in fair agreement.

### 3.2.3 Estimation of coherence times

From the spectrum (see Figure 3.4) the coherence times of the qubit can be estimated. The linewidths of the spectroscopic peaks (see Figure 3.6 (a)) allow the extraction of the dephasing time  $T_2$ . For a weak probe signal with a photon number smaller than unity, the line shape is Lorentzian and the linewidth corresponds directly to the dephasing rate  $\Gamma_\varphi = 1/T_2$ . For higher photon numbers the linewidth will be homogeneously broadened [SWB+05]. Here, a driving signal of less than one photon has been applied. The spectroscopic peaks in and out of the symmetry point are shown in Figure 3.6 (a), where the so-called sweet spot of the flux qubit is clearly visible. In the symmetry point, the linewidth is much narrower than out of it. The solid lines show fits to Lorentzians from which  $T_2$  is extracted. In Figure 3.6 (b) the fit results are shown. The minimal dephasing rate is 29 MHz, which corresponds to a dephasing time of 35 ns. Even though the dephasing time is somewhat lower than expected, it is comparable to the results of measurements in the time domain on qubits from the same fabrication run [Jer09]. There, a spin-echo measurement yields 41 ns. The phase coherence follows a linear dependence on the detuning from the symmetry point similar to the one observed by Kakuyanagi *et al.* [KMS+07].

Note, that the dephasing rate exceeds the coupling strength while the coupling exceeds the photon loss rate, placing the system in the intermediate coupling regime.

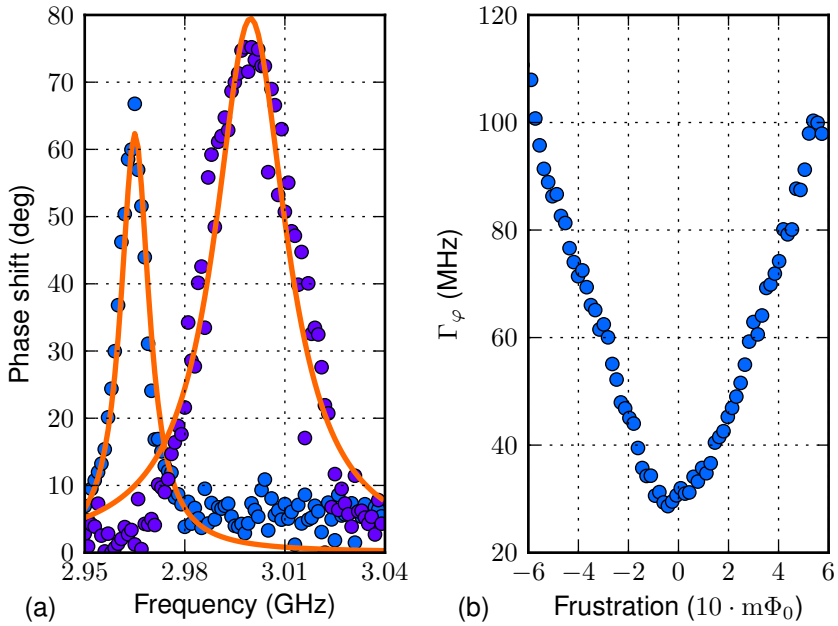


**Figure 3.6:** From the linewidths of the spectroscopy peaks the phase coherence of the qubit can be estimated. (a) Two peaks at different qubit bias points. The peak with smaller linewidth is taken at the symmetry point, the one with higher linewidth out of the symmetry point. The solid lines show the Lorentzian curves used to extract the dephasing rate. (b) The dependence of the dephasing rate  $\Gamma_\varphi$  on the qubit frustration.

### 3.3 Temperature dependence

In this section, the temperature dependence of the system is studied. In subsection 3.3.1 the shape of the dispersive shift is analysed, which behaves as expected. More surprisingly, the symmetry point of the flux qubit appears at different bias points for different temperatures. Indeed, it is seen, that the periodicity of the flux qubit changes (see subsection 3.3.2). Here, the periodicity refers to the external magnetic flux needed to generate one flux quantum in the qubit loop. The only reported shift similar to this one has been observed in SQUIDS and has been related to the relaxation of paramagnetic spins on the surface of the superconductor [SHK+08].

#### 3.3.1 Dispersive shift

The dispersive shift as discussed in subsection 3.2.2 is measured in dependence on the mixing chamber temperature. The results for different temperatures are shown in Figure 3.7. The magnitude of the dispersive shift is reduced with increasing temperature. This is a direct consequence of the thermal excitation of the qubit. The population difference between ground and excited state of the qubit in thermal equilibrium depends on the temperature  $T$  as

$$\tanh\left(\hbar\omega_q/(2k_B T)\right) . \quad (3.2)$$

The dispersive shift as described by Equation (3.1) is modified by this factor. The expected phase shifts are in good agreement with the data (see solid lines in Figure 3.7). For higher temperatures a deviation occurs. Not only the population of the qubit changes, but also the persistent current is reduced with increasing temperature. Therefore, the dip becomes wider and smaller than expected when only considering the thermal excitation.

#### 3.3.2 Change of flux bias

The change of the flux threading the qubit loop in dependence on the temperature is monitored by measuring the periodicity. Two different runs (Set 1 and Set 2) have been performed, showing reproducible results.

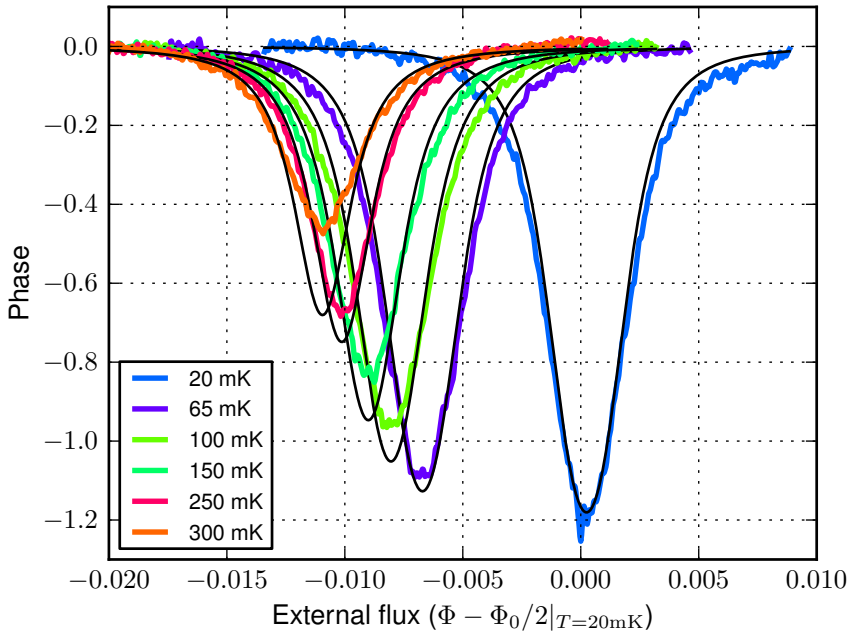


**Figure 3.7:** The dispersive shift at the fundamental mode of the resonator in dependence on the mixing chamber temperature. The magnitude of the shift is reduced, which is related to an increased population of the excited qubit state due to excitation from the environment. The black lines show the theoretical curves. In addition, the bias point of the qubits is shifting.

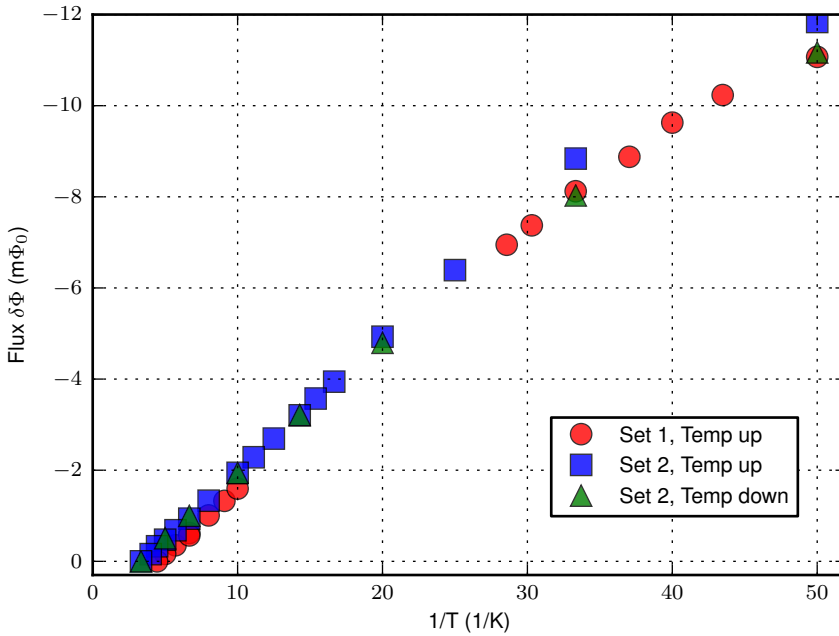


**Figure 3.8:** Temperature dependence of the flux threading a single superconducting flux qubit. Three different data sets are shown. The measurement was performed twice for increasing temperature (Set 1 and Set 2, Temp up) and once for decreasing temperature (Set 2, Temp down). The different set numbers refer to different cool downs of the cryostat.

The periodicity increases with increasing temperature, consequently the magnetic field required to provide one flux quantum increases as well. The magnitude of the effect is reproducible for different cool downs and therefore does not depend on the specifics of the cool down procedure. There is no hysteretic behaviour, since the measurements in Set 2 prove no significant difference between increasing and decreasing the temperature.

The change of the flux threading  $\delta\Phi$  is recalculated by normalizing the periodicity, given in the current  $I_{\text{per}}$  used to generate the magnetic flux through the external coil, to the one measured at the highest temperature (225 mK and 300 mK, respectively),  $\delta\Phi = (I_{\text{per}} - I_{\text{per, max}}) / I_{\text{per, max}}$ . A clear inverse proportional dependence on the temperature is observed (see Figure 3.8). The Curie-like dependence indicates a paramagnetic origin of the effect. On the reason for the paramagnetic behaviour, whether it is due to paramagnetic spins or the effect of other paramagnetic residuals in the environment, can not be concluded, yet. This issue requires further study.

## 3.4 Dressed states

Dressed states are of growing importance for quantum information processing. Quite early there has been the idea to use dressed states for quantum gates [RBD05] or as tunable coupling mechanism [LSN06], yet only recently they are experimentally investigated in the field of superconducting qubits. For example, the coherence in a strongly driven system has been studied [WJD+10]. Recently, the renormalized decay rates in the dressed system have been used for cooling the qubit [MVZ+12]. At the end of this section, the renormalized decay rates in the dressed system will be used to amplify the signal passing the cavity.

Here, the system is studied under the influence of a strong driving signal. In the first experiment the driving and probing signals are identical. A dependence on the power of the probing field at  $\omega_{r,1}$  is shown in Figure 3.9. The lowest power shown is already exceeding the single photon limit leading to the appearance of resonances on top of the dispersive shift. Those resonances result from multiphoton transitions and are discussed in subsection 3.4.1. With increasing photon number the

dispersive shift gets distorted. This results from the renormalization of the qubit spectrum by the AC-Zeeman shift (see subsection 3.4.2).

In a second set of experiments, two microwave tones are applied: One weak probe signal at the fundamental mode with a photon number less than unity and a strong driving signal to dress the qubit at the third harmonic of the resonator. Figure 3.10 shows the dependence of the phase and amplitude transmitted at the weak probe field on the frustration versus the photon number of the driving field. Besides the dispersive shift, which is also visible in the amplitude, an additional resonance appears. The shape of this resonance differs from the resonances observed due to an excitation of the qubit. Indeed, it is the result of resonant interaction between the dressed qubit states and the probe signal. Interestingly, the amplitude transmitted in the resonance exceeds the transmission corresponding to an amplification. This so-called Rabi resonance will be discussed in subsection 3.4.3.

### 3.4.1 Multiphoton transitions

The qubit may not only absorb one resonant photon, but can also be excited by simultaneously absorbing two or more photons. In sum, the photons need to accord with the transition frequency of the qubit. The two-photon transition can be used in order to access otherwise forbidden side band transitions [WSB+07]. This non-linear process appears at high-photon numbers. Figure 3.11 shows the results for two different photon numbers. First, the two-photon resonance appears already at photon number  $N < 1 \cdot 10^3$ , where the resonance position corresponds to a qubit transition frequency of  $\omega_q = 2 \cdot \omega_{r,1}$ . The second resonance occurs at a qubit transition frequency of  $\omega_q = 3 \cdot \omega_{r,1}$  and therefore relates to a three-photon excitation process. The suppression of the dispersive shift and the peak at the degeneracy point results from the re-normalization of the qubit spectrum by the AC-Zeeman shift discussed in the next subsection.

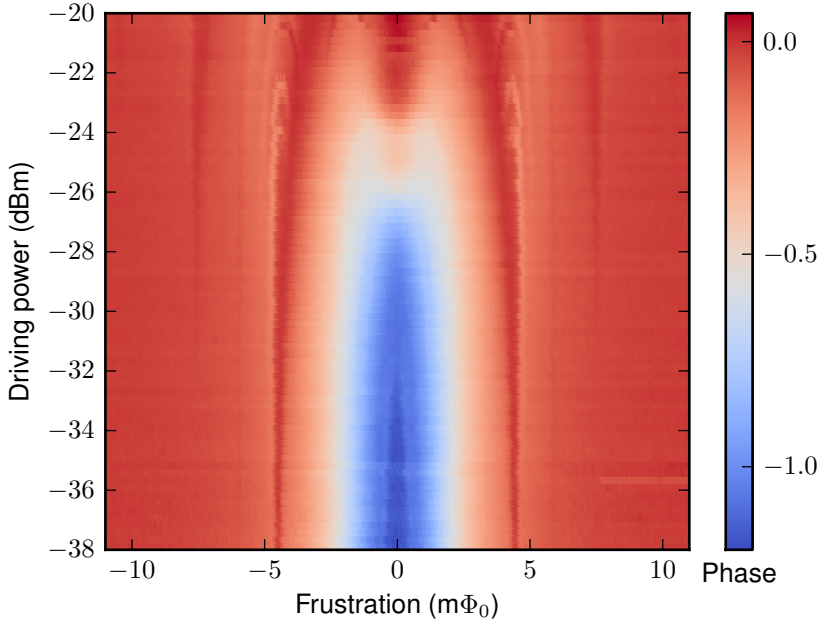


**Figure 3.9:** The system is probed at the fundamental mode frequency  $\omega_{r,1}/2\pi$ . The shading shows the transmitted phase in dependence on the power of the probe signal and the qubit frustration. At low signals the dispersive shift as discussed before is dominating, whereas at higher power clear two- and three-photon resonances appear. Furthermore, the dispersive shift changes its shape due to the shift of the qubit frequency in dependence on the photon number  $N$ . The small resonances, which appear in the vicinity of the two-photon resonance at a drive power of -25 dBm and at the degeneracy point at about -21 dBm have not been explained, yet.

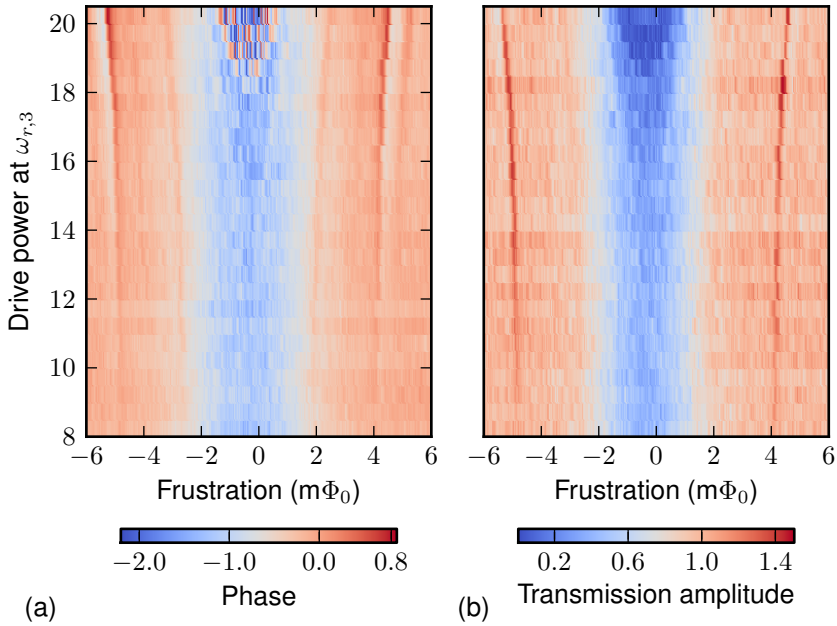


**Figure 3.10:** The system is weakly probed at the fundamental mode frequency  $\omega_{r,1}/2\pi$ , while a second driving tone is applied at the third harmonic frequency  $\omega_{r,3}/2\pi$ . The dependence of the phase (a) and amplitude (b) on the driving power and the frustration is shown. The second tone dresses the qubit. When the level splitting of the dressed states equals the frequency of the fundamental mode, the Rabi resonance can be observed.

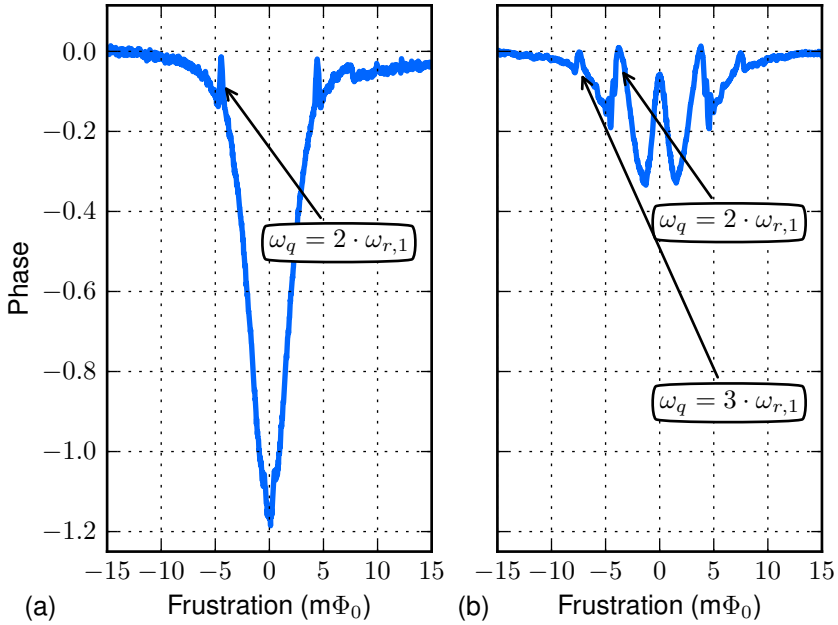


**Figure 3.11:** Multiphoton transitions in a single flux qubit. (a) The two-photon resonance shown for a photon number of  $N = 0.7 \cdot 10^3$ . (b) At a higher photon number the three-photon excitation of the qubit becomes also visible, here shown for  $N = 39 \cdot 10^3$ . The peak at the symmetry point is due to the AC-Zeeman shift.

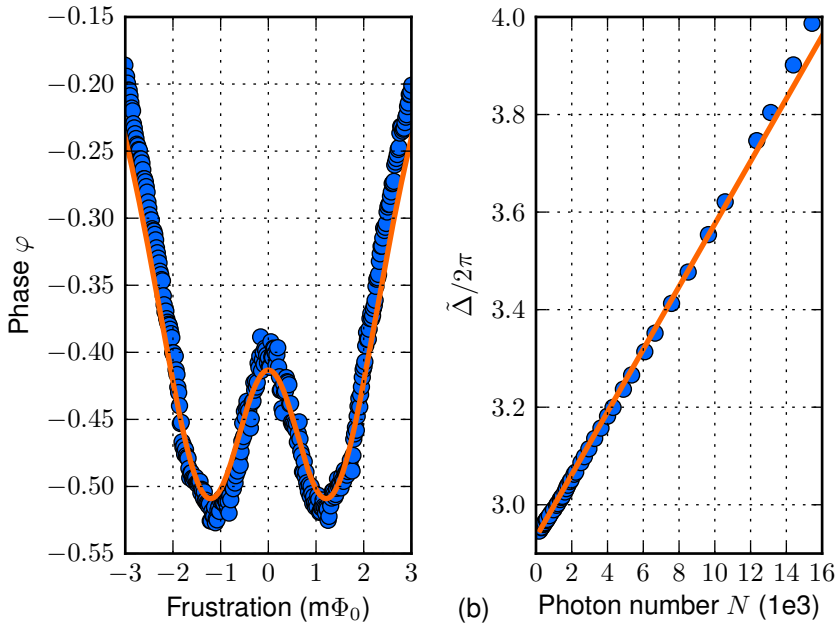


**Figure 3.12:** (a) The dispersive shift measured at a photon number of  $N = 16 \cdot 10^3$ . The solid line shows a fit according the combined Equations (3.3) and (3.1). (b) The dependence of the minimal qubit frequency  $\tilde{\Delta}$  on the photon number  $N$ . The solid line shows the expected linear dependence.

#### 3.4.2 AC-Zeeman shift

Not only the qubit shifts the resonator frequency, but also the frequency of the qubit is altered by the resonator. The resulting shift is known as the AC-Zeeman shift and the qubit frequency changes linearly with the photon number  $N$  in the cavity:

$$\tilde{\omega}_q = \omega_q + 2 \frac{N \cdot g_\epsilon^2}{\omega_q - \omega_r}. \quad (3.3)$$

With increasing photon number the qubit transition is shifted to higher frequencies.

On the one hand, when fitting the dispersive shift with the gap  $\Delta$  as only free parameter, the renormalized transition frequency at the symmetry point of the qubit  $\tilde{\Delta}$  can be extracted from the data shown in Figure 3.9. This method can be applied only as long as the dispersive shift does not get distorted too much, especially when no peak occurs at the degeneracy point. The peak at high photon numbers is a consequence of the non-linearity of the AC-Zeeman shift. The shift depends on the coupling between qubit and resonator which is fully transversal and therefore maximal at the symmetry point. Out of the symmetry point the coupling is reduced. Consequently, at high photon numbers, the qubit frequency at the symmetry point is no longer the minimal transition frequency of the qubit. On the other hand, using the renormalized qubit frequency according to Equation (3.3) in Equation (3.1) for fitting the data, the photon number  $N$  can be extracted. This method works as long as the multiphoton resonances do not dominate the transmitted phase. The curve resulting from fitting at a photon number of  $N = 16 \cdot 10^3$  compared the measurement data is shown Figure 3.12 (a). Here, the qubit frequency has been shifted for about 1 GHz to 4 GHz at the symmetry point. The dependence of  $\tilde{\Delta}$  on the photon number  $N$  is shown in Figure 3.12 (b). The extracted data shows a clear linear dependence on the photon number. The possibility to change the qubit spectrum by a continuous drive will be applied later in order to tune the multi-qubit system (see subsection 4.4.2).

### 3.4.3 Rabi resonance and level inversion

When the qubit is driven strongly, its levels are splitted. In the quantum mechanical picture this is a direct result of the photon ladder created by the driving field and the coupling between the resulting degenerate states, which is proportional to the driving strength (see Figure 3.13 (a)). The frequency of the splitting in the resonantly driven system is called on-resonance Rabi frequency  $\Omega_{R0}^N = 2g_\epsilon\sqrt{N}$ . The resulting dressed states are an equal superposition of  $|g, N + 1\rangle$  and  $|e, N\rangle$ . The system becomes more complex, when the frequency of the driving field  $\omega_D/2\pi$  is detuned from the qubit transition frequency by  $\delta = \omega_D - \omega_q$ . For a negative detuning  $\delta$ , the energy of  $|g, N + 1\rangle$  is lowered by  $\delta$  compared to  $|e, N\rangle$  (see Figure 3.13 (b)). The splitting is increased, where

$$\Omega_R^N = \sqrt{\delta^2 + (\Omega_{R0}^N)^2} \quad (3.4)$$

is the generalized Rabi frequency. Therefore, the dressed states are no equal superpositions anymore. In the general case, the dressed states are [CTDRG98]

$$\begin{aligned} |1N\rangle &= \sin \Theta |g, N + 1\rangle + \cos \Theta |e, N\rangle, \\ |2N\rangle &= \cos \Theta |g, N + 1\rangle - \sin \Theta |e, N\rangle, \end{aligned}$$

where  $\tan 2\Theta = -\Omega_{R0}^N/\delta$ .

For large  $N$  and small deviations from the average photon number  $\langle N \rangle$  of the driving cavity field,  $\Omega_R^N$  can be substituted by the constant value  $\Omega_R = \Omega_R^{\langle N \rangle}$ . Consequently, the dressed states  $\{|1\rangle, |2\rangle\}$  can be taken as effective two level system with a transition frequency  $\Omega_R$ . In the case of  $\delta < 0$ , the excited state  $|1N\rangle$  is mainly formed by  $|e, N\rangle$ . As the qubit is in its ground state, the dressed system will remain in its ground state as well. This is different for a positive detuning  $\delta$ , where the energy of  $|e, N\rangle$  is lowered by  $\delta$  compared to  $|g, N + 1\rangle$  (see Figure 3.13 (c)). Now, the excited state  $|1, N\rangle$  is dominated by  $|g, N\rangle$ . Hence, when the qubit relaxes, the dressed system gets excited. Such, there is a population inversion for the dressed system. Its energy diagram is depicted in Figure 3.13 (d). For a rigorous derivation of the renormalized relaxation rates in the dressed system, refer to [HFH+08] or [OMA+13].

### 3 Dressed state amplification

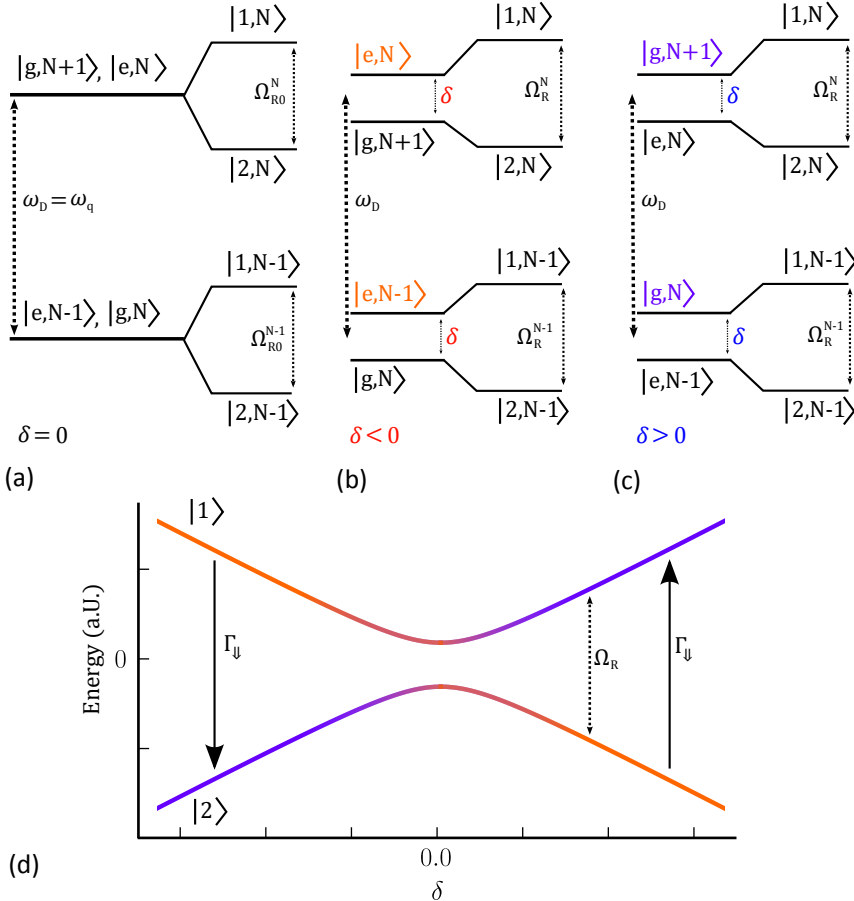


**Figure 3.13:** Energy level diagrams for the different cases of strongly driving the qubit. (a-c) show the dressed qubit system in the photon ladder of the driving field for different detunings  $\delta = \omega_D - \omega_q$ . (following [CTDRG98]) (d) After tracing over the photon number  $N$  an effective two-level system, denoted with states  $|1\rangle$  and  $|2\rangle$ , is obtained. Both the sign and strength of the relaxation (excitation) in this system depend on the detuning.

If the resonator  $\omega_{r,1}$  is tuned in resonance with the dressed system, it will either lose photons due to absorption ( $\delta < 0$ ) or win photons due to spontaneous or stimulated emission ( $\delta > 0$ ). If the photons in the cavity possess a lifetime of  $1/\kappa$  longer than the energy relaxation of the qubit  $T_1$ , which is the case for the system presented here ( $47 \mu\text{s} > \approx 10 \mu\text{s}$ ), the condition for stimulated emission will be formally fulfilled. In order to optimize the process the relaxation rate of the qubit may be artificially enhanced. In a second sample this has been successfully realized by using a resistive gold film close to the qubit. In that case, the relaxation time of the qubit has been estimated to be only 12.5 ns [OMA+13]. Yet, in order to rigorously prove lasing, the photon field generated in the resonator has to be characterized. A lasing process would create a coherent state with a Poisson distribution in the photon number contrary to the incoherent state following a Bose-Einstein distribution [HFA+08].

In the experiment presented here, the qubit is driven at the third harmonic frequency  $\omega_D = \omega_{r,3}$ , because this provides optimal coupling strength of the driving signal to the qubit. In the weak probing signal the signature of resonant coupling (see Figure 3.14 (a)) is visible, which is the Rabi resonance

$$\omega_{r,1} = \Omega_R . \quad (3.5)$$

Indeed, at the resonance a clear amplification of the transmitted signal of up to 40 % is observed (see Figure 3.14 (b)). The position of the Rabi resonance has been extracted from Figure 3.10. Its dependence on the driving strength is shown in Figure 3.15. The data is in good agreement with the theoretical dependence according to Equation (3.5).

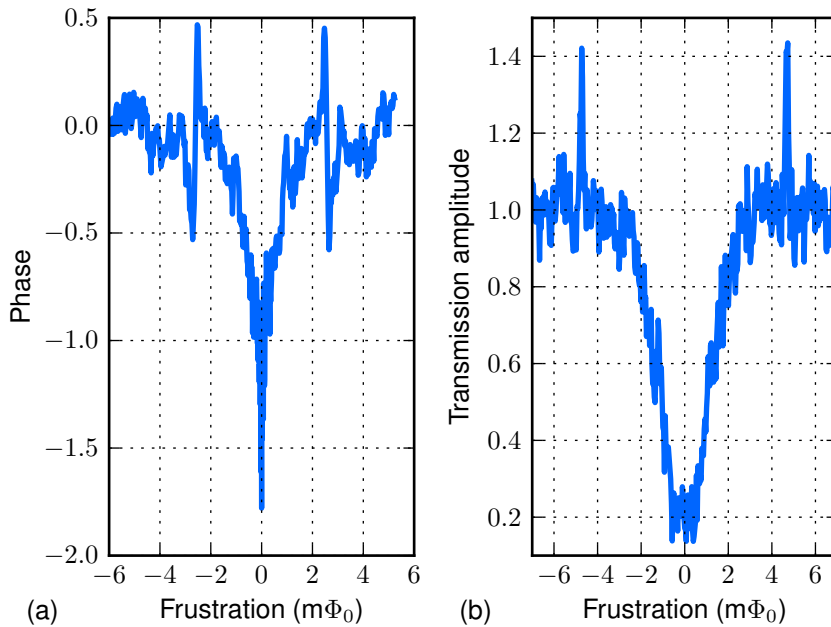


**Figure 3.14:** Individual traces taken from Figure 3.10. The phase (a) and amplitude (b) of the transmitted signal at the fundamental mode frequency while continuously driven in the third harmonic. In the phase signal a resonant phase shift is visible, whereas the transmitted amplitude is amplified in this point.

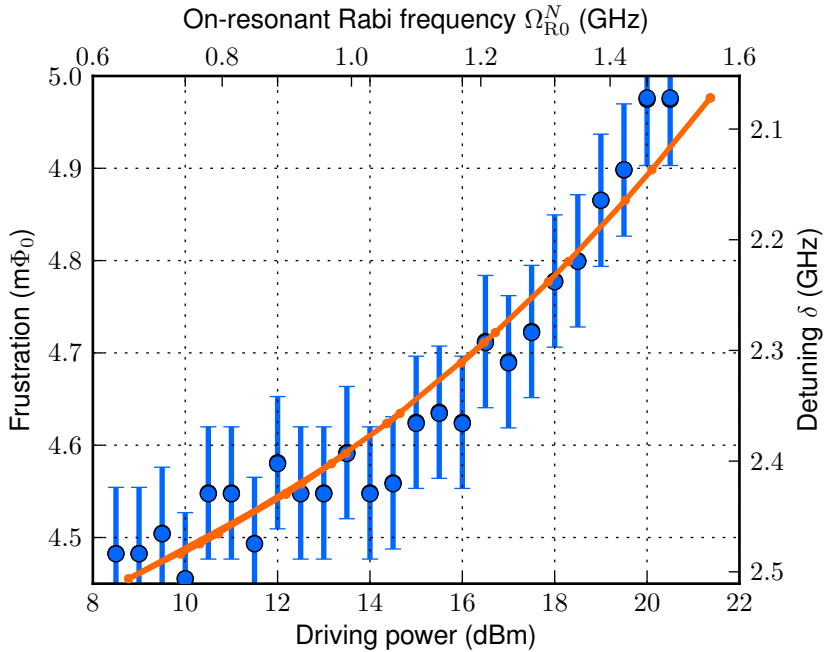


**Figure 3.15:** The dependence of the Rabi resonance on the driving strength. The experimental positions have been extracted from Figure 3.10 (closed circles), the error is estimated to be twice the flux resolution. From the resonance condition the on-resonance Rabi frequency can be calculated. The orange solid line shows the theoretical position of the Rabi resonance, obtained independently from the qubit parameters.



## 4 Implementation of a quantum metamaterial

*In the previous chapter the interaction of a single qubit and a resonator has been studied. Next, the system is expanded to a higher number of qubits. Such a system forms a metamaterial in the sense, that many artificial atoms couple to an electro-magnetic wave with a wavelength much larger than the atom dimension. In reference to the field of metamaterials [ZK12]; [RZS+08], this constitutes the first implementation of a truly quantum metamaterial. The transmission through the metamaterial is not studied directly, but by making use of a resonator that exhibits a standing wave. The photon field in the resonator is localized and consequently the coupling is well defined. All qubits are coupled individually to the resonator while the qubit-qubit coupling is designed to be negligible leaving the system in an uncoupled (disordered) paramagnetic ground state, if far detuned from the resonator. The coupling to the resonator is chosen in such a way, that only collective effects are expected to be visible. In resonance, when the level spacing of the qubits equals the frequency of the resonator, the degeneracy between their states is lifted and an avoided level crossing (anticrossing) in the spectrum of the resonator is observed in the absence of decoherence. In the collective case of  $n$  mutually non-interacting qubits [Dic54], an enhancement by a factor of  $\sqrt{n}$  compared to a single-qubit anticrossing is predicted. This has been demonstrated for up to 3 qubits [FSS+10]. Nonetheless, no experiment has yet been reported involving many superconducting qubits coupled to a resonator.*

*The first section of this chapter introduces the design properties of the sample (4.1). Thereafter, the first set of experiments is presented. When the qubits can be detuned from each other, spectroscopic or ground state measurements reveal all parameters of the system at once [IPS+08]. With no means to individually control the qubits, the ensemble parameters can*

only be extracted by employing several complementary measurements. In section 4.2, the fundamental properties of the metamaterial are extracted by the means of spectroscopy, analysis of the resonances between qubits and resonator modes as well as the phase shift in the fully dispersive regime. The spectroscopy provides only a rough estimate of the qubit parameters and suffices for a first insight into the properties of the metamaterial. The phase shift in the fully dispersive regime gives an estimate of the total number of qubits. The effective parameters for the qubit metamaterial are extracted from its resonances with the different modes of the resonator. The main result - the demonstration of resonant interaction of up to 8 qubits and the resonator - is presented in section 4.3. The resonant phase shift between the qubit system and the resonator is quantitatively analysed. Interestingly, the system exhibits two stable states, whose time evolution concludes this subsection. Subsequently, an additional microwave drive is employed in order to tune the metamaterial via the AC-Zeeman shift of the qubits and observe additional resonances, such as multiphoton transitions (see section 4.4).

### 4.1 The sample

So far, there have been only few attempts to fabricate samples containing many coupled superconducting qubits [Paa09]. For flux qubits the lowest transition frequency  $\Delta$  depends exponentially on the ratio  $\alpha$  making the fabrication of qubits with similar parameters challenging. This is of special importance when realizing arrays of coupled qubits. If one qubit is off, the array might be interrupted by this defect and the experiment is likely to fail. In order to overcome this pitfall, the photon field of a resonator is used to mediate the coupling between the qubits rather than relying on direct qubit-qubit interaction. In principle, the coupling of each qubit to the resonator is uniform and does not depend on the relative position of the qubits.

The sample studied contains 20 flux qubits embedded into a single cavity (see Figure 4.1). It was fabricated in the clean room facilities of the IPHT Jena. The qubits and the resonator are galvanically decoupled, making the qubit fabrication independent on the resonator fabrication.

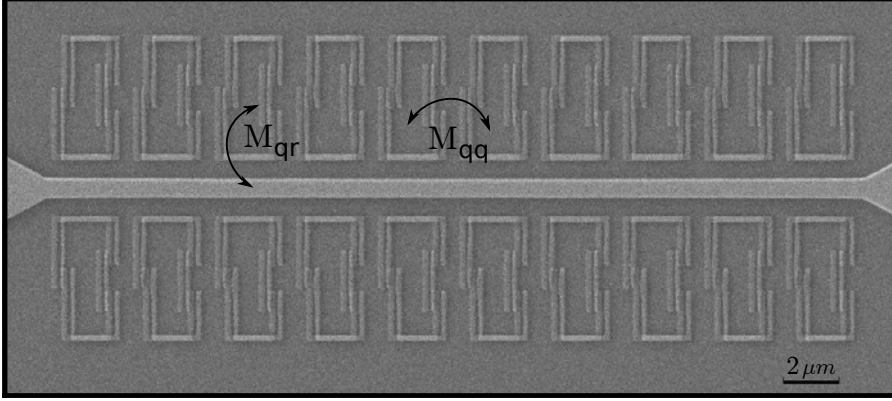


**Figure 4.1:** Scanning electron micrograph of the sample showing the central part of the coplanar waveguide resonator where the qubits are situated. Each qubit is individually coupled to the resonator by the mutual inductance  $M_{qr}$  and to its neighbour by  $M_{qq}$ . In the current system the qubit-qubit coupling is negligible.

They were fabricated in two separate steps. In the following the sample design and the fabrication process are discussed. Moreover, the coupling constants are calculated from geometry, and from the junction sizes first estimations of the qubit parameters are made.

#### 4.1.1 The resonator

A coplanar waveguide resonator (CPWR) of similar geometry as in chapter 3 is used. Contrary to lumped-element resonators, the CPWR has higher harmonics  $\omega_{r,m} \approx m \cdot \omega_1$ , which are accessible through the measurement setup up to  $m = 5$  (see Figure 4.2). This feature has already been exploited for strong driving of a single qubit (see section 3.4). Here, the harmonics are not only used for strong driving, but also to probe resonant interaction at different frequencies. The fundamental mode frequency is  $\omega_{r,1}/2\pi = 2.594$  GHz and its quality factor  $Q_1 = \omega_{r,1}/\kappa_1 = 47 \cdot 10^3$ . The quality factors vary roughly 10 % from cooldown to cooldown. This indicates a good magnetic shielding and that only few vortices are frozen in the superconducting film.

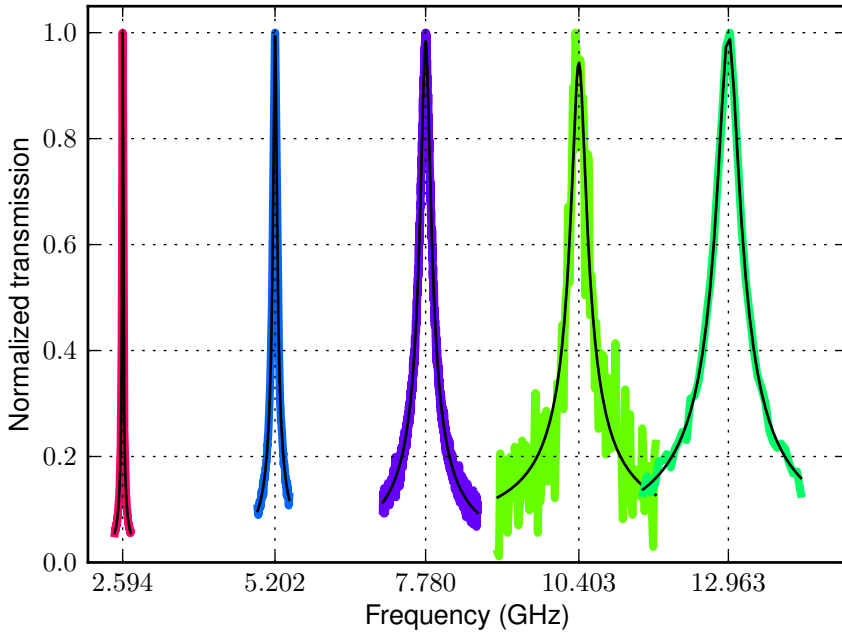


**Figure 4.2:** The fundamental mode and the first four harmonics of the resonator. The black lines are fits to Lorentzians. The resonance frequencies  $\omega_{r,m}/2\pi$  (GHz) are 2.594, 5.202, 7.780, 10.403 and 12.963. The linewidths are  $\kappa_m/(2\pi)$  (KHz) 55.5, 216, 715, 950 and 1400.  $\kappa_m$  are the photon loss rates of the resonator. The curves are scaled over the frequency axis to a factor of 250 to ensure visibility over this large frequency range. The relative linewidth is to scale. Please note, that only  $\omega_{r,1}$ ,  $\omega_{r,2}$  and  $\omega_{r,3}$  are within the band of the cold amplifiers and the corresponding isolators. Therefore, the signal to noise ratio in  $\omega_{r,4}$  and  $\omega_{r,5}$  is relatively low, but nevertheless resolvable.

The resonator has been fabricated by e-beam lithography and dry etching of a 200 nm thick Nb film deposited on a high-resistivity silicon substrate. The length of the resonator's central line is 23 mm, its width is 50  $\mu\text{m}$ , and the gap between the central line and the ground plane is 30  $\mu\text{m}$  resulting in a wave impedance of 50  $\Omega$ . In the middle of the resonator the central line is tapered to a width of 0.8  $\mu\text{m}$  for a length of 30  $\mu\text{m}$  with a 9  $\mu\text{m}$  gap which provides better qubit-resonator coupling. The resulting impedance mismatch detunes the harmonics of the resonator. Otherwise the taper is not expected to alter the properties of the modes themselves significantly, as its length is much smaller than the wavelength. The difference to the resonator used in chapter 3 are the gap capacitors, whose width are reduced to 5  $\mu\text{m}$ . This reduces the insertion loss of the resonator and decreases the quality factor slightly. The inductance of the resonator  $L_r = (11.0 \pm 0.4)$  nH is calculated using finite element electromagnetic simulation in FastHenry [Whi01] and Sonnet [Son] for the full geometry. The latter includes the effect of the kinetic inductance, yet at an estimated 0.1 pH/sq it only accounts for 0.05 nH. The main contribution to the resonator's inductance arrives from the geometric inductance. The zero-point currents  $I_{r,m} = \sqrt{\hbar\omega_m/L}$  of the odd-resonator modes  $I_{r,m}$ ,  $m = (1, 3, 5)$  result as  $(12.5 \pm 0.5)$  nA,  $(21.6 \pm 0.8)$  nA and  $(28 \pm 1)$  nA.

The sample does neither contain additional microwave lines nor DC-bias lines for manipulating the qubits. The resonator acts as filter which suppresses out-of-band signals by approximately  $1/Q$ , which influences the driving strength when manipulating the qubit by off-resonant microwaves directly applied to the resonator. In practice, only a small signal reaches the qubits because of the relatively high  $Q$ -factors.

### 4.1.2 The qubits

#### Junction parameters

The 20 three-junction flux qubits are placed at the center of the resonator. The target area of the two identical junctions of each qubit is  $700 \times 200$  nm at a design critical current density of about 200 A/cm<sup>2</sup> and a junction capacitance of 4.9 fF. They are fabricated using conventional two-angle

#### 4 Implementation of a quantum metamaterial

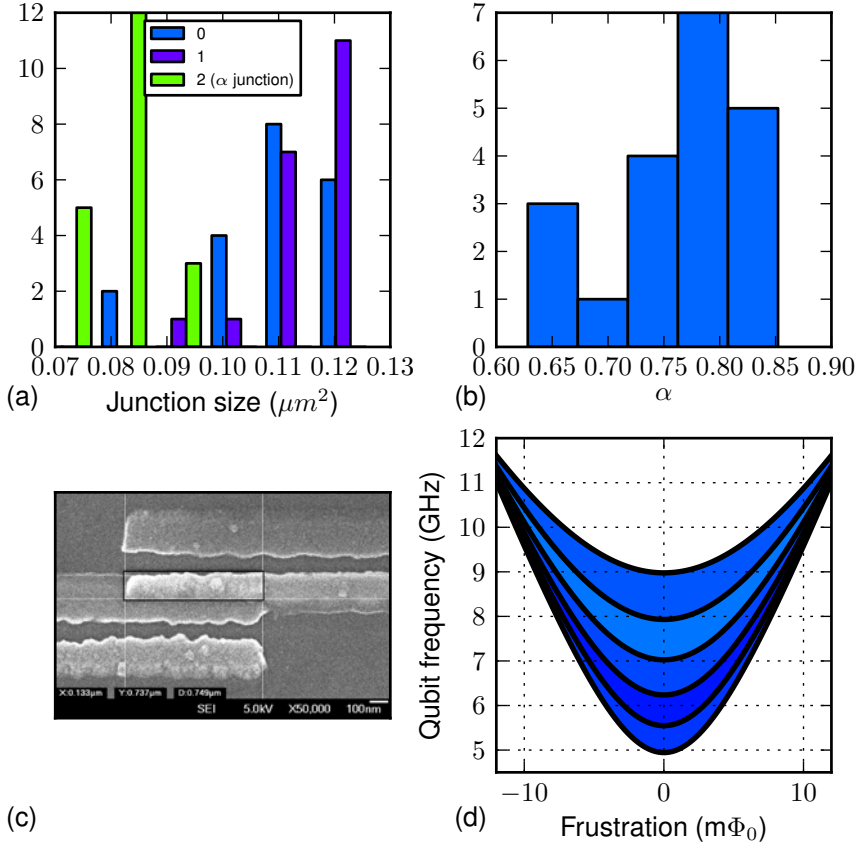


**Figure 4.3:** (a) Histogram of the junction areas for the three junctions of the flux qubit. 0 and 1 are the two bigger junctions, whereas 2 refers to the  $\alpha$  junction. (b) Histogram of the corresponding ratios  $\alpha$ . (c) An electron micrograph of a single Josephson junction, from which the junction size - the black-rimmed area - was extracted. The two shadows from the fabrication technique appear on the right and left side of the junction. (d) Expected qubit spectra for the  $\alpha$  value distribution in (b). The shaded areas in between two black lines correspond to the bins in (b), the number of qubits expected in each such region from the lowest to the highest frequency is 5, 7, 4, 1 and 3.

shadow evaporation technique [Dol77]. By making use of e-beam lithography two layers of photo resist are prepared forming a mask above the substrate. Subsequently, two layers of aluminium are deposited under opposite angles at a rate of 1.8 nm/s. Before evaporation of the second layer, the surface of the first aluminium film is oxidized in an oxygen atmosphere of  $10^{-2}$  mbar for 6.5 min. In the finalizing step the photo resist is lifted off leaving a superconductor–insulator–superconductor tunnel junction on the chip. The evaporation in two opposing angles using a two-slit mask results in three lines of aluminium, forming two separate layers due to the oxidation step. Both layers are overlapping on the central line (see Figure 4.3 (c)).

The areas for each junction and each qubit were extracted from electron micrographs of a second chip processed in the same run as the one described in this chapter. During an electron micrograph static charges are accumulated, which can alter the junction properties. This is why a second chip was used. The histogram of the areas for each junction is shown in Figure 4.3 (a), where the bin size reflects the uncertainty in the junction area, which is about 10 %. Each junction has a well pronounced maximum containing up to 12 similarly sized junctions. This translates into a similar distribution of  $\alpha$  values, the ratio between the size of the smallest junction and of the larger junctions, in the range of [0.6, 0.9]. Here, the uncertainty in  $\alpha$  is as large as two bins. Still, from Equations (2.13) and (2.11) the qubit parameters can be estimated. The Josephson energy is  $E_j \approx 81$  GHz and the charging energy  $E_c \approx 4$  GHz. The resulting qubit spectra are shown in Figure 4.3 (d). About 16 qubits are expected to possess a gap  $\Delta$  below the third harmonic  $\omega_3$  of the resonator. The mean value is 6.8 GHz at a standard deviation of 1.4 GHz. The relative spread of about 20 % is consistent with the results previously obtained for the fabrication process [JPM+11]. The two regions containing most qubits ( $n = 5, 7$ ) have a width of only 0.6 GHz. The expected persistent current  $I_p$  is of the order of 100 nA.

The low ratio of  $E_j/E_c \approx 20$  might result in a sensitivity to gate charges. As a consequence the gap is under the influence of charge fluctuations, which might be the reason for the time dependent variation of the parameters of the metamaterial discussed in subsection 4.3.3.

### Qubit-resonator coupling

The bare coupling between the qubits and the resonator results from the persistent current  $I_{p,j}$  in the qubit loop and the zero-point current of the resonator  $I_{r,m}$ . The coupling energy is then  $\hbar g = M_{qr} I_{p,j} I_{r,m}$ , where  $M_{qr}$  is the mutual inductance between the qubit and the resonator. The value of  $M_{qr} = 0.51$  pH has been numerically calculated using FastHenry [Whi01].

It is also possible to estimate the mutual inductance by assuming a rectangular loop with height  $h$  and length  $l$  placed in a distance  $x$  next to an infinite wire carrying the zero-point current  $I_{r,m}$ . According to the Biot–Savart law the magnetic field at the loop is  $B = \mu_0 I_{r,m} \frac{1}{2\pi x}$ . The flux  $\Phi$  threading the loop is obtained by integration over its area. The mutual inductance results from

$$M_{qr} = \frac{\Phi}{I_{r,m}} = \frac{\mu_0 l}{2\pi} \ln\left(\frac{x+h}{x}\right). \quad (4.1)$$

The qubit's dimensions are  $l = 1.6 \mu\text{m}$  and  $h = 4.3 \mu\text{m}$ . Its distance to the central line of the resonator is  $1.1 \mu\text{m}$ . Equation (4.1) results in an inductance  $M_{qr,e} = 0.51$  pH, which is identical to the numerical calculation. This is surprising, because the influence of the currents in the ground plane have not been taken into account.

Yet, this can easily be accomplished by simplifying the ground plane to a one-dimensional wire as well. The distance of each qubit to the ground plane is  $4.5 \mu\text{m}$ . The total mutual inductance will be the sum of the contribution of the central line and of the ground plane  $M_{qr,e} = 0.51 \text{ pH} + 0.2 \text{ pH} = 0.71 \text{ pH}$ .

That value is again consistent with the result of an implementation of this idealized case in FastHenry, which yields  $0.71$  pH. If the ground plane on the opposite side of the central wire is taken into account, the idealized simulation already results in  $0.55$  pH. The fact, that the central wire accounts for the full mutual inductance implies that the effects from the ground planes effectively annihilate each other. As a consequence, Equation (4.1) can be used in order to calculate the coupling of the qubit from its geometry. This allows for a propagation of uncertainty.

The uncertainty for the dimensions extracted from the micrograph are  $\pm 0.03 \mu\text{m}$ , which leads to  $\Delta M_{qr} = \pm 0.02 \text{ pH}$ .

Now, it is possible to give a first estimate of the coupling strength. The coupling of the qubits to the resonator is of the order of  $g_{qr}/2\pi \approx \cdot 1 \text{ MHz}$ .

### Qubit-qubit coupling

The mutual inductance between two neighbouring qubits is  $M_{qq} = 0.13 \text{ pH}$ . This leads to a qubit-qubit interaction strength of  $g_{qq} = M_{qq}(I_p)^2$ . For the parameters in the system the qubit-qubit coupling is of the order  $2\pi \cdot 2 \text{ MHz}$ , leading to  $g_{qq} \approx 0.002 \cdot \Delta \ll \omega_q$ , leaving the system in its paramagnetic ground state [Tia10]. For such a small coupling, only the qubits' effective transition frequencies are shifted a few MHz (see subsection 2.1.3). The spread in parameters further decreases the effective coupling. The distribution of parameters is not expected to be uniform among qubits, that is why identical qubits are unlikely to be nearest neighbours. Thus, the qubits are effectively uncoupled, when detuned from the resonator modes.

## 4.2 Characterization of parameters

Spectroscopy is the standard procedure for obtaining information on the level structure of a multi-atom system. Despite the weak coupling to off-resonant<sup>1</sup> microwave radiation, performing a spectroscopic analysis in the fully dispersive regime  $\omega_{r,m} < \Delta_{q,j}$  was possible and several sets of parameters were identified. As the qubit-qubit coupling is weak no deviations from the hyperbolic single-qubit spectrum, such as qubit-qubit anticrossings, are observed. Several parameter sets can be extracted, yet no information on the number of qubits taking part in each set could be obtained (see subsection 4.2.1). The number of qubits in the parameter sets will be resolved through the analysis of the resonant regime  $\omega_{r,m} \approx \omega_{q,j}$  (see next section 4.3). The resonant case between the resonator modes and qubits is used in order to extract effective sets of parameters for the resonant modes of the qubit metamaterial (see

---

<sup>1</sup>to the resonator modes

subsection 4.2.2). At the end of this section the dispersive shift opposed on the resonator by the qubit metamaterial is analysed, which yields the total number of qubits in a working parameter range (see subsection 4.2.3).

### 4.2.1 Spectroscopy

In order to gain a first impression of the qubit parameters a two-tone spectroscopy experiment is performed. The resonator is continuously probed by a weak signal directly at the fundamental mode frequency  $\omega_{r,1}/2\pi$ . The phase of the signal is recorded while a second microwave tone  $\omega_s$  is applied at the input of the resonator. The frequency of the second tone  $\omega_s/2\pi$  is swept in the area range of the expected qubit transition frequencies.

The phase of the transmitted probe signal, measured as a function of the external magnetic flux controlling the qubit level spacing, exhibits a dip in the vicinity of the degeneracy point  $\Phi = 0$ , when the gaps  $\Delta_j$  are above the energy of the resonator. This dip, originated from the shift of the resonance frequency of the resonator-qubits system, is usually called a dispersive shift. It is analysed in detail in subsection 4.2.3. The dispersive shift is directly proportional to the state of qubit  $j$ , the expectation value of  $\sigma_z^j$ . When the additional driving signal is resonant with a qubit transition frequency,  $\omega_s = \omega_{q,j}$ , the expectation value of  $\sigma_z^j$  becomes zero, resulting in the disappearance of the shift for the excited qubits. In the strong coupling regime, this is applied in order to dispersively readout the state of the qubits [BHW+04].

Figure 4.4 shows the dispersive shift and overlying spectroscopy peaks for two different excitations frequencies. Compared to the result in subsection 3.2.1, where a clear spectroscopy signal was observed, the coupling of the out-of-band microwave signal is much weaker. The peaks are small compared to the overall shift, because not all qubits are involved in their formation and because the excited qubits might not be fully saturated due to the weak drive. In Figure 4.4 (a) several parallel spectroscopy peaks at a fixed excitation frequency are shown. In order to reconstruct the spectrum symmetric peaks around the degeneracy point are taken, which can be followed over at least two consequential excitation

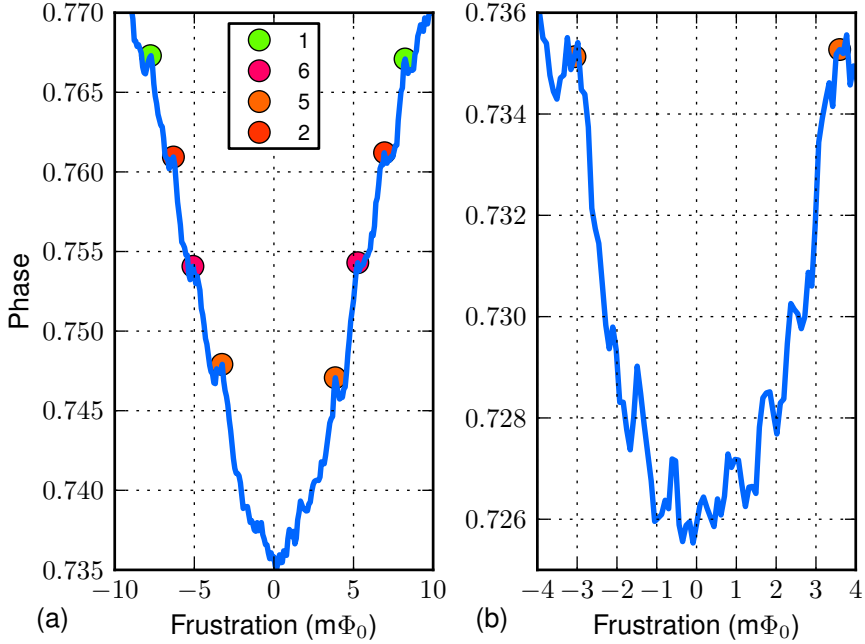


**Figure 4.4:** Spectroscopic measurement of the qubit system. (a) The left panel shows the dispersive shift of the phase transmitted at the fundamental mode frequency  $\omega_{r,1}/2\pi$  with resonances  $\omega_s = \omega_{q,j}$  on top at an excitation tone of  $\omega_s/2\pi = 6.15$  GHz. The closed circles correspond to the different qubit sets as introduced in Figure 4.5. (b) The right panel shows the area around the symmetry point at an excitation tone of  $\omega_s/2\pi = 6.1$  GHz. The resonances around the degeneracy point arrive from qubits, which could not be assigned unambiguously to a qubit set.

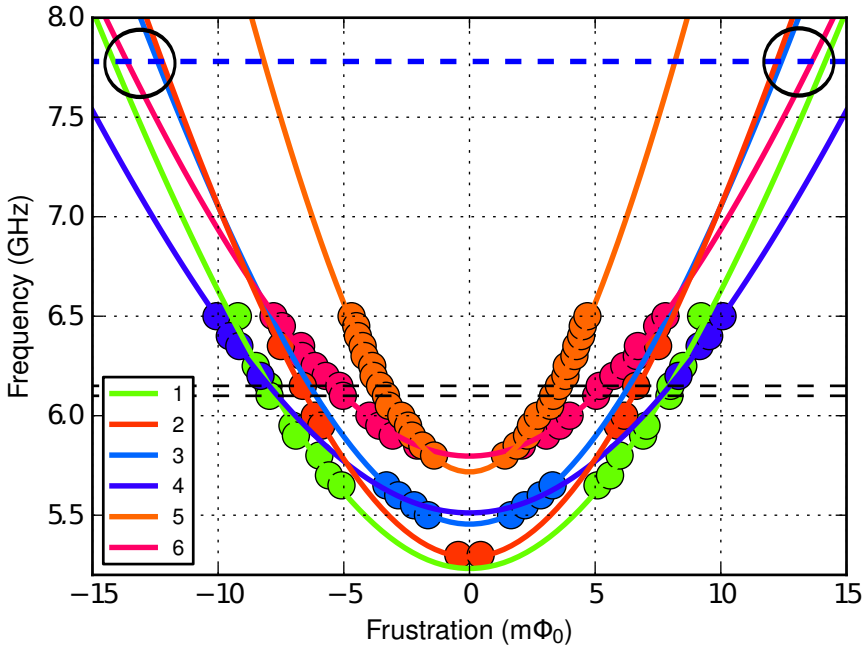


**Figure 4.5:** The two-tone spectroscopy shows several resonances through which individual sets of qubits can be identified. The data points (closed circles), extracted from single traces as shown in Figure 4.4, allow the distinction of 6 different sets. The solid lines show fits to the hyperbolic qubit spectra. The horizontal dashed line in blue corresponds to the frequency of the third harmonic. The black circles show the region where resonant interaction of several qubits and the resonator is expected. The lower dashed lines correspond to the two excitation frequencies for the traces shown in Figure 4.4.

frequencies. If a resonance peak satisfies this condition it is assigned to an individual set of parameters. The data points of the set are fitted to the hyperbolic frequency dependence on a flux qubit. Symmetric resonances which appear on the extrapolation of the fit are added to the set. It does not appear to be possible to unambiguously follow all peaks and assign them to individual sets of qubits. One example are the resonances around the degeneracy point which start at about 6 GHz (see Figure 4.4 (b)).

The final results of these measurements and their analysis is presented in Figure 4.5. In total, 6 different sets could be identified. The solid lines are fits for each set  $j$  to hyperbolic qubit spectra  $\omega_{q,j} = \sqrt{\Delta_{q,j} + (2I_{p,j}\Phi/(\hbar\Phi_0))^2}$ . A summary of the parameters can be found in the first part of Table 4.1. In principle, they are consistent with those expected from the junction properties (see subsection 4.1.2). The mean gap  $\Delta$  is about 5.5 GHz with a standard deviation of 0.2 GHz. However, this does not account for the resonances with a gap of about 6 GHz. The full spread might be close to 0.8 GHz as previously reported for the fabrication technology [JPM+11]. The mean persistent current is 71 nA with a standard deviation of 17 nA. This is slightly less than expected, yet of the same order of magnitude. The error margin for the persistent current  $I_{p,j}$  is at least  $\pm 1.5$  nA, whereas the gaps are exact to about  $\pm 100$  MHz. The coupling of the qubits to the third harmonic is expected to be about 1 MHz.

### 4.2.2 Reconstruction from higher harmonics

In this experiment, the resonator is probed at the center frequencies of the harmonics  $\omega_{r,3}$ ,  $\omega_{r,4}$  and  $\omega_{r,5}$ . No additional microwave tone is applied. The phase at the probe frequency is monitored while the frustration is varied.

The symmetric features appearing most prominently in the third harmonic correspond to a resonant mode between the qubits and the resonator (see Figure 4.6). They are discussed in detail in section 4.3. Here, the fact that the transition frequency of qubit ensemble  $j$  is equal with the frequency of resonator mode  $m$ ,  $\omega_{q,j} = \omega_{r,m}$ , is used in order to reconstruct the ensemble parameters. Fitting those resonance points (closed

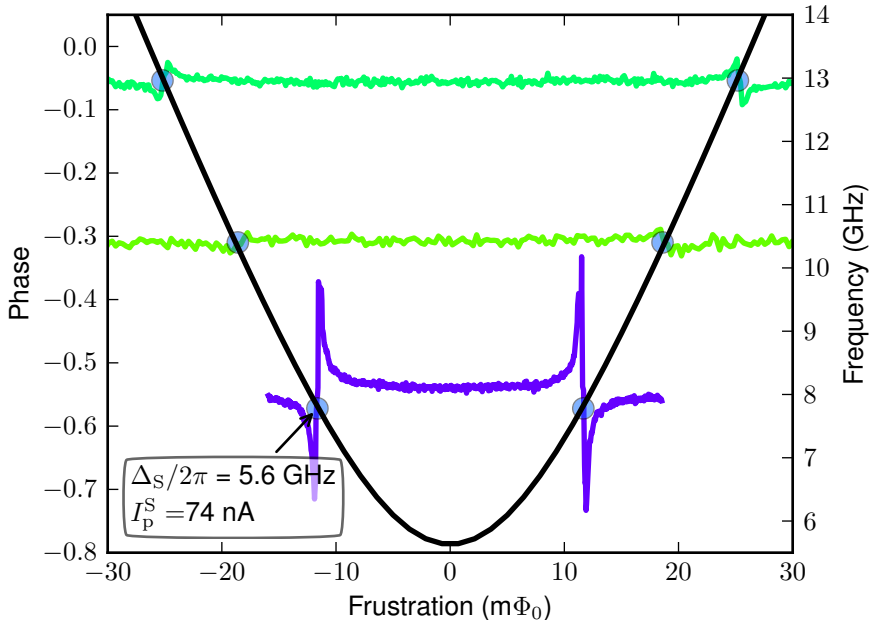


**Figure 4.6:** The transmission through the system at the 3rd, 4th and 5th harmonic frequency in dependence on the qubit transition frequencies (frustration) in state 1 of the system. The curves are separated in phase by an offset, in a way that their position corresponds to the probe frequency indicated on the right y-axis. This axis also shows the qubit frequencies of effective parameter set S (solid line) which is extracted from the resonance points (closed circles).

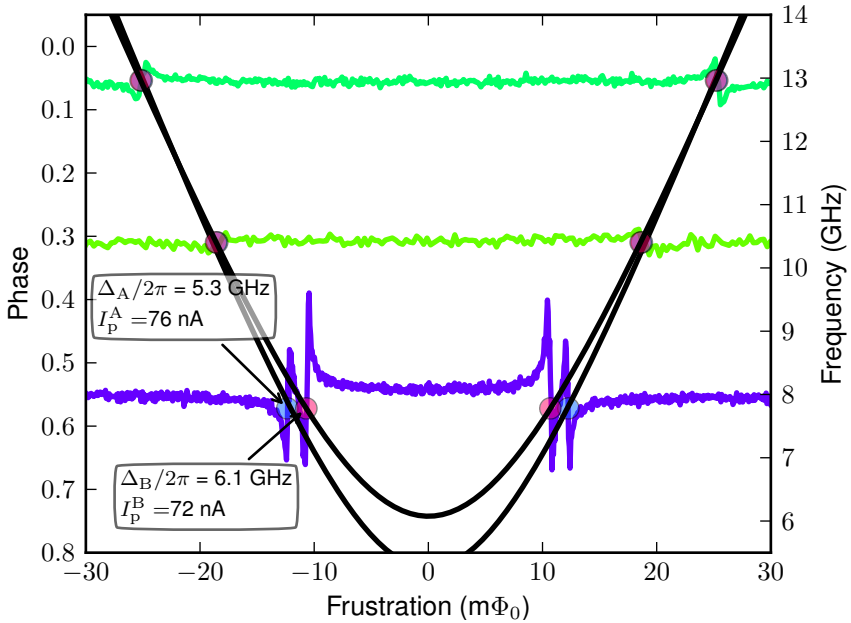


**Figure 4.7:** The transmission through the system at the 3rd, 4th and 5th harmonic frequency in dependence on the qubit transition frequencies (frustration) in state 2 of the system. The curves are separated in phase by an offset, in a way that their position corresponds to the probe frequency indicated on the right y-axis. This axis also shows the qubit frequencies of the two effective parameter sets A and B (solid lines) which are extracted from the resonance points (closed circles).

Set	$\Delta_j/2\pi$ [GHz]	$I_{p,j}$ [nA]	$g_{j3}/2\pi$ [MHz]
1	5.2	70	1.1
2	5.3	74	1.2
3	5.5	70	1.1
4	5.5	55	0.9
5	5.7	103	1.6
6	5.8	61	1
Mean	5.5	71	1.2
Std	0.2	17	0.2
Set A	5.26	76	1.2
Set B	6.08	72	1.2
Set S	5.63	74	1.1

**Table 4.1:** The parameter sets extracted from the spectroscopy (Figure 4.5, sets 1-6) and resonant interaction (Figures 4.6 and 4.7, sets A, B and S). Sets 1-6 are ordered according to ascending  $\Delta_j$ .  $g_{j3}$  is the coupling to the third harmonic for a single qubit calculated from  $I_{p,j}$ . For sets 1-6, the error in  $I_{p,j}$  is  $\pm 1.5$  nA and the resulting error in the coupling to the third harmonic is  $2\pi \cdot 0.1$  MHz. The spectroscopy yields no information on the number of qubits responsible for one resonance. The errors for sets A, B and S are  $\Delta I_{p,j} = \pm 1$  nA and  $\Delta \Delta_j < \pm 2\pi \cdot 50$  MHz. The error in the coupling is  $\pm 2\pi \cdot 0.1$  MHz, calculated for the uncertainty in the inductance of the resonator of  $\Delta L_r = \pm 0.4$  nH and in the mutual inductance  $\Delta M_{qr} = \pm 0.02$  pH. Anticipating the quantitative analysis in subsection 4.3.1 it is known, that ensembles A and B consist of 4 qubits each. Ensemble S comprises 8 qubits.

circles, Figure 4.6) to the hyperbolic dependence on the transition frequency of a flux qubit yields  $\Delta_S/2\pi = 5.63$  GHz and  $I_{p,S} = 74$  nA. This agrees well with the average values from sets 1-6. The individual coupling of the qubits in this mode to the resonator is  $g_{j3} = 2\pi \cdot (1.2 \pm 0.1)$  MHz. This is state 1 of the metamaterial, referring to the one resonant mode.

The system exhibits two stable states with a different number of resonant modes (see subsection 4.3.3). In the second state two distinct resonant phase shifts appear, whereas in the higher harmonics again only one resonant phase shift is visible (see Figure 4.7). The single resonance

at higher harmonics is expected as ensembles with similar persistent current converge at high frustration. Yet, the signal-to-noise ratio in  $\omega_{r,4}$  would not allow to distinguish between two close lying resonant modes. By fitting the resonance points to the hyperbolic dependence on the transition frequency of a flux qubit, two sets of effective parameters can be extracted. Set A ( $\Delta_A = 2\pi \cdot 5.26$  GHz,  $I_{p,A} = (76 \pm 1)$  nA) is close to the average values of the parameters found in the spectroscopy (see subsection 4.2.1). The position of the resonance points matches within the error of  $I_{p,j}$  the region where sets 1,2,3 and 6 converge. The second set B ( $\Delta_B = 2\pi \cdot 6.08$  GHz,  $I_{p,B} = (72 \pm 1)$  nA) presumably arises from those qubits whose gaps were found to be in the range of 6 GHz in the spectroscopy. The individual coupling of the qubits in modes A and B to the resonator is  $g_{j3} = 2\pi \cdot (1.2 \pm 0.1)$  MHz. All parameters are summarized in Table 4.1. Note, that the parameters of ensemble S correspond to the average values of ensembles A and B. This hints, that ensemble S is formed by some kind of overlap of A and B, an assumption that will be further supported later on.

### 4.2.3 Ground state measurement

When all the qubit gaps  $\Delta_j$  are higher than the resonator frequency no resonant interaction occurs. A frequency shift - the so-called dispersive dip - of the resonator is observed while tuning the frustration. It can be understood as a consequence of the AC-Zeeman shift, the pull of the cavity frequency by all qubits of  $\pm g_\epsilon/\delta$  for each qubit in dependence on its state, where  $\delta = \omega_q - \omega_r$  is the qubit-resonator detuning. If the system remains in the ground state at all times, the cavity shift depends solely on the qubit-resonator detuning. Similarly, it may also be interpreted in terms of a change of the susceptibility of the qubits with their frustration, which inductively influences the resonance frequency. The susceptibility of the qubits follows the curvature of their ground state. Here, no resonant interaction occurs, therefore the system remains in its ground state at all times. Hence, this subsection is called ground state measurement.

For frequencies below 5.3 GHz, the qubit metamaterial is in the full dispersive regime, when probing the resonator at the fundamental mode  $\omega_{r,1}/2\pi$  frequency and at the second harmonic  $\omega_{r,2}/2\pi$  frequency. In

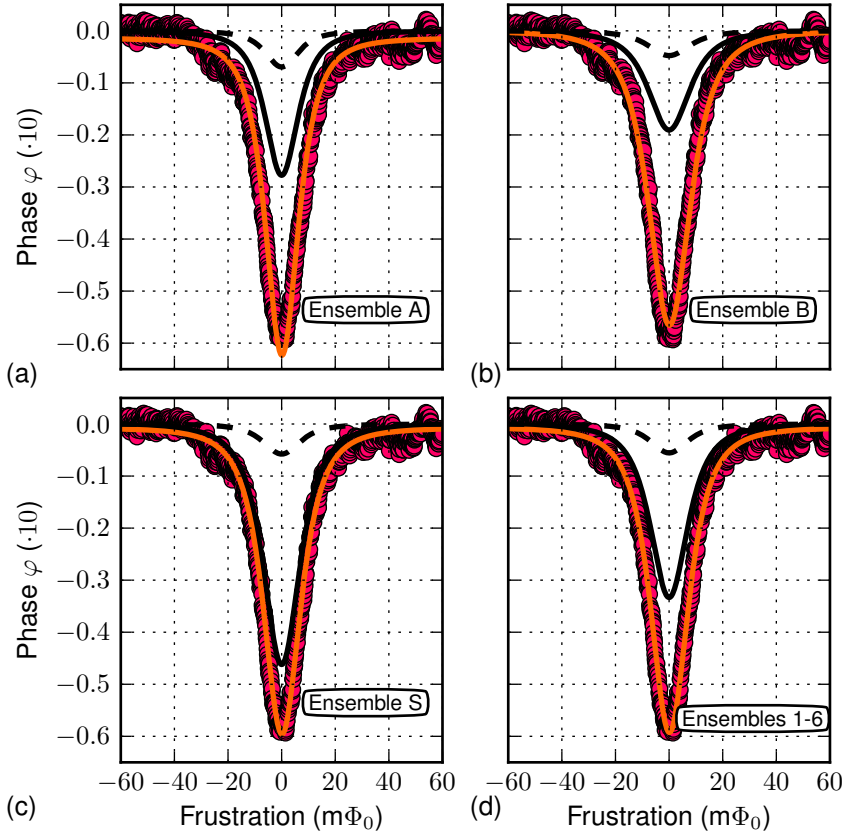


**Figure 4.8:** Dispersive shift at the fundamental mode frequency induced by all qubits in dependence on their frustration. In each panel, the black dashed line shows the expected curve for a single qubit. The black solid lines are the theoretical phase shifts for ensembles A, B and S, where the number of qubits  $n$  is known. For ensembles 1-6 it is assumed, that each set contains a single qubit. No ensemble accounts for the full shift by itself. The orange solid lines show fits to Equation (4.2) with  $n$  as only fitting parameter.

this regime the detuning between qubits and resonator  $\delta_{jm}$  is always above the dephasing  $\Gamma_\varphi$ . The formula for the transmitted phase through the metamaterial consisting of  $n$  atoms, Equation (2.30), consequently simplifies to

$$\tan \varphi = -\frac{2ng_{jm,\epsilon}^2}{\kappa\delta}, \quad (4.2)$$

where  $g_{jm,\epsilon} = g_{jm}\Delta_j/\epsilon_j$  is the transversal coupling.

### The fundamental mode

Figure 4.8 shows the dispersive shift measured at the fundamental mode frequency  $\omega_{r,1}/2\pi$ . The experimental data is compared to the expected shifts for the different qubit ensembles extracted before. Note, that the shift induced by a single qubit (black dashed lines) is always much weaker than the one actually observed. For further discussion specific results from the following section must be anticipated. Parameter sets A and B constitute 4 qubits each. The orange dashed line shows the theoretical dispersive shift for each ensemble independently (see Figure 4.8 (a) and (b)). As expected, they do not amount for the full magnitude of the shift. The same is true for set S with 8 qubits in total (see Figure 4.8 (c)). When fitted to Equation (4.2) with the ensemble parameters A, B, S (orange dashed lines) and  $n$  as a free parameter, best fits are obtained for 9, 12 and 10 qubits, respectively. The fit to the parameters for set A slightly overshoots while the one for set B is slightly smaller. In contrary, the fit using the parameters of set S agrees well to the data, which indicates that those parameters reflect the distribution of the qubit system well. This is also the case for the average values from sets 1-6. Here, the best fit is obtained for 10 qubits.

The number of qubits is in principle consistent with the analysis of the junction areas (see subsection 4.1.2). However, some outliers are unavoidable. The dominating influence arrives from the qubits in the resonant modes, which have a minimal detuning to the fundamental mode. The remaining qubits can have a high gap (low  $\alpha$ ) resulting in a negligible contribution to the dispersive shift which is proportional to  $1/\omega_q^3$ . Another explanation may be a very low persistent current or a very small gap, both resulting in a negligible coupling and therefore a

negligible contribution to the dispersive shift. That said, the number of qubits extracted by the fit to the fully dispersive shift constitutes a lower bound on the total number of working qubits.

In general, the observation of a smaller shift than expected might indicate the occurrence of qubit-qubit entanglement, which leads to a reduction of the dispersive shift as a result of the reduced energy of the frustrated state compared with the uncoupled one [IGI+04]. Yet, the coupling between qubits far away from the resonance with the resonator is expected to be negligible (compare with subsection 2.1.3).

### The second harmonic

In the second harmonic, the standing wave in the resonator possesses a minimum in the current and a maximum in the voltage. The coupling of qubits to the resonator is governed by the capacitance between both. The coupling constant is unknown, but can be determined experimentally from the dispersive shift measured in  $\omega_{r,2}$  (see Figure 4.9). Considering the fit with the coupling as free parameter and the mean values from sets 1-6 as well as an effective qubit number of  $n = 10.5$ , a coupling of  $g_{j2} \approx 0.4$  MHz is obtained. The fit deviates from the data, as it appears to be somewhat steeper and deeper. Ensemble A with a minimal splitting  $\Delta_A = 2\pi \cdot 5.26$  is fairly close to the second harmonic frequency  $\omega_{r,2} = 2\pi \cdot 5.202$  GHz. Although still in the dispersive regime, those qubits lie close to the resonant regime, because the detuning between qubits and resonator is of the same order as the dephasing. This could be the reason for the observed deviation.

## 4.3 Resonant interaction

In the preceding section the basic properties of the metamaterial have been characterized and several sets of parameters have been extracted. Yet, except for a lower bound on the total number of qubits, no further information on the number of qubits taking part in each set has been revealed. This question will be addressed from the data showing resonant interaction with the resonator. Resonant modes are observed in the

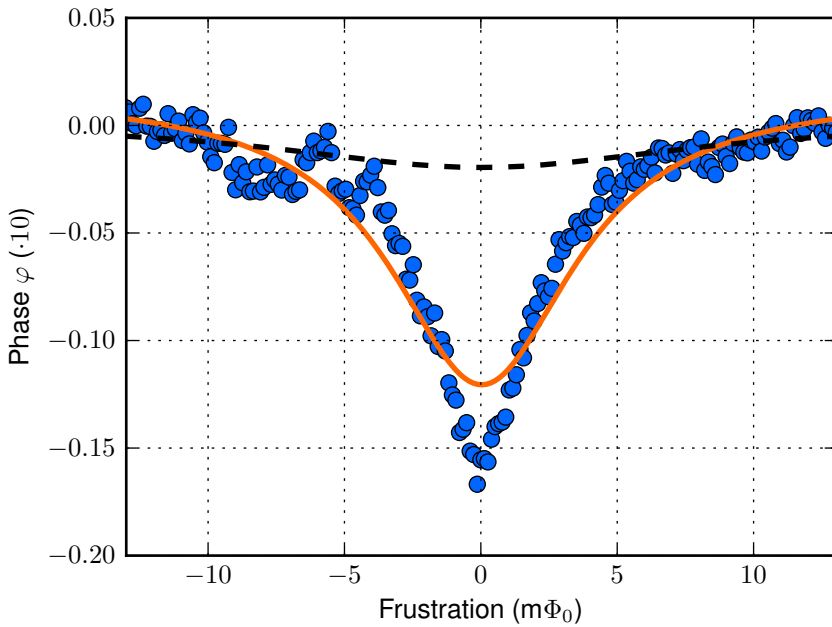


**Figure 4.9:** Dispersive shift of the phase transmitted at the second harmonic frequency in dependence on the frustration induced by all qubits. Using the parameters of set S, the data is fitted and an estimate of the coupling to the second harmonic is extracted. The black solid line shows the expected shift for a single qubit with this coupling.

regime  $\Delta_j < \omega_{r,m}$ . Consequently, the first crossing between the qubits and the resonator is expected at the third harmonic (blue dashed line in Figure 4.5), where several fits from the spectroscopy converge at a frustration of about  $11 \text{ m}\Phi_0$ . The average coupling to the third harmonic is about 1 MHz. This places the parameters of the system on the edge of the strong-coupling limit, close to the intermediate regime where  $g_{jm} > \kappa_m$ , but  $g_{jm} \approx \Gamma_\varphi$  [OPM+10], with  $\Gamma_\varphi$  being the qubit dephasing rate. Here, the two vacuum-Rabi peaks of a qubit-resonator anticrossing can not be resolved, but the signature of the anticrossing is still visible. Single qubit interactions fall in the regime  $g_{qr} \leq \kappa_3$ , which leads to the disappearance of single qubit anticrossings [OSG+10]. With the collective coupling of  $n$  qubits the regime  $\kappa_3 < \sqrt{n}g_{j3}$  is reached again. Note, that for small  $n$  the magnitude of the phase signal scales linearly with  $n$ .

The quantum metamaterial exhibits two states, one with two resonant modes and one with a single resonant mode, which will be analysed in the following subsection 4.3.1. By fitting the two resonant modes observed in the transmitted phase at the third harmonic frequency, the number of qubits in sets A and B is obtained. Equally treating the data of the single resonant mode reveals the number of qubits in set S. Furthermore, the single resonant phase shift observed in the higher harmonics can be described theoretically using the previously extracted values (see subsection 4.3.2).

As already denoted, the system undertakes a transition from those two resonant modes to one single resonant mode. The time dependence and stability of this process is described in subsection 4.3.3.

### 4.3.1 Analysis of the resonant modes

In state 1 of the metamaterial, a single resonant mode appears in the phase transmitted at the third harmonic signal (see Figure 4.10 (a)). First, the phase shifts to negative values relative to its off-resonant value. When crossing the resonance from lower frequencies the phase reappears from positive values, which is due to a jump of the phase at the resonance. If no dephasing occurred, the phase curve would be singular. Hence, the finite width of this effect is a result of the dephasing  $\Gamma_\varphi$  in the system. Out of this resonance the resonator is dominated by the dispersive shift, similarly

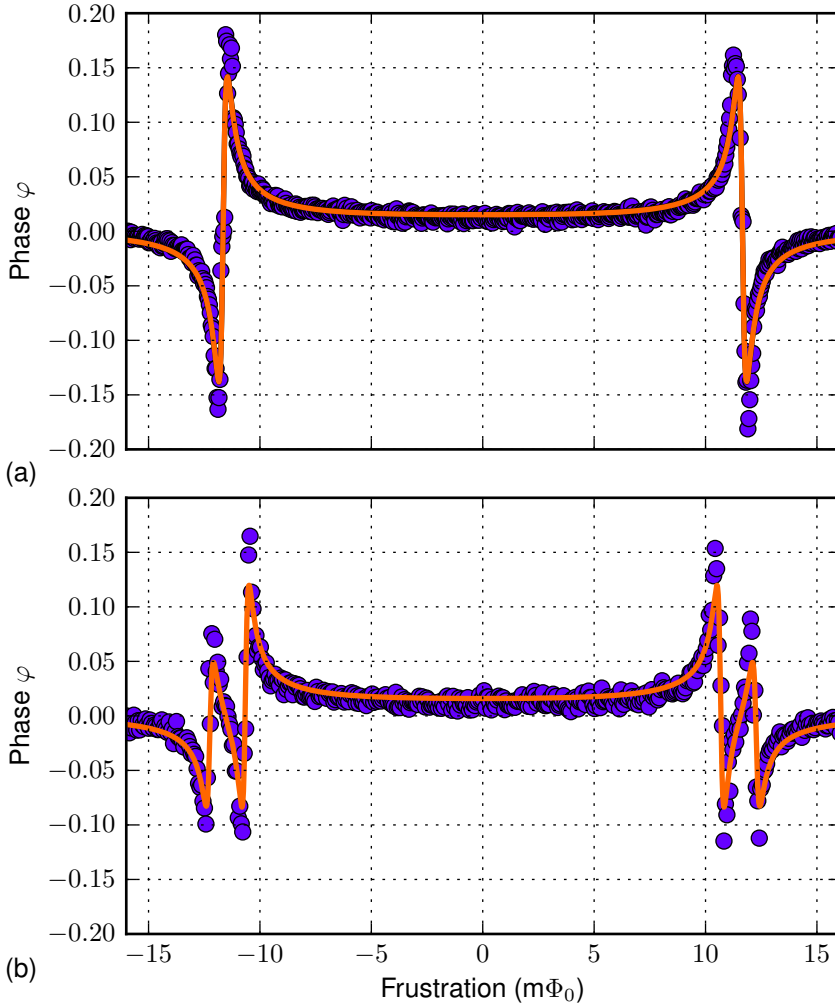


**Figure 4.10:** The measurement of the transmitted phase at the third harmonic signal  $\omega_3$  in the two states of the qubit system. The upper panel (a) shows state 1 with a single resonant mode. The data (closed circles) is fitted using Equation (2.30) (solid line). The best fits yields 8 qubits. The lower panel (b) shows data (closed circles) in state 2 with two resonant modes. The best fits for the outer and inner mode yields 4 qubits each.

as characterized in subsection 4.2.3. The sign of the shift depends on the qubit-resonator detuning  $\delta$  and has opposite signs inside and outside the resonances. In state 2 of the metamaterial, two distinct resonant modes appear in the phase transmitted at the third harmonic frequency of the resonator (see Figure 4.10 (b)).

### The model and fitting

The energy relaxation  $\Gamma_{\downarrow}$  has no significant influence on the resonant phase shift, the photon loss rate  $\kappa_m$  is defined by the linewidth of the resonator and the qubit parameters have been determined as sets A, B and S, respectively. The remaining parameters of the system are the number of qubits  $n$  and the dephasing rate  $\Gamma_{\varphi}$ .

In order to model the system the Tavis-Cummings Hamiltonian is utilized, i.e. the model Hamiltonian for  $n$  mutually non-interacting qubits coupled to a single bosonic mode. The phase transmitted through the resonator corresponds to the argument of the expectation value for the annihilation operator of the resonator. An analytical formula in the semi-classical limit for a weakly driven system has been developed in subsection 2.2.1, resulting in Equation (2.30). Note, that the theoretical phase shift quantitatively corresponds to the one measured in the experiment, without any normalization or calibration factor. Cables and amplifiers contribute as a constant offset to the measured phase, yet they do not influence the phase shift itself. Furthermore, it has been shown (see subsection 2.2.3), that dephasing and qubit number dominate different regimes. The dephasing is responsible for the width of the resonant mode, whereas the dispersive shift out of resonance is independent on the dephasing. Therefore,  $n$  and  $\Gamma_{\varphi}$  can be regarded as independent parameters in certain regions. Still, the magnitude is a result of both of them.

The best fit for the single resonant mode yields  $n_S = 8$  and  $\Gamma_{\varphi,S} = 2\pi \cdot 53$  MHz (see solid line Figure 4.10 (a)). The dephasing rate corresponds to a phase coherence time of several ns which is expected. In order to fit the two resonant modes, it is assumed that they are detuned from each other, and hence can be treated independently. The total phase shift results from the individual phase shifts of ensemble A and ensemble B,

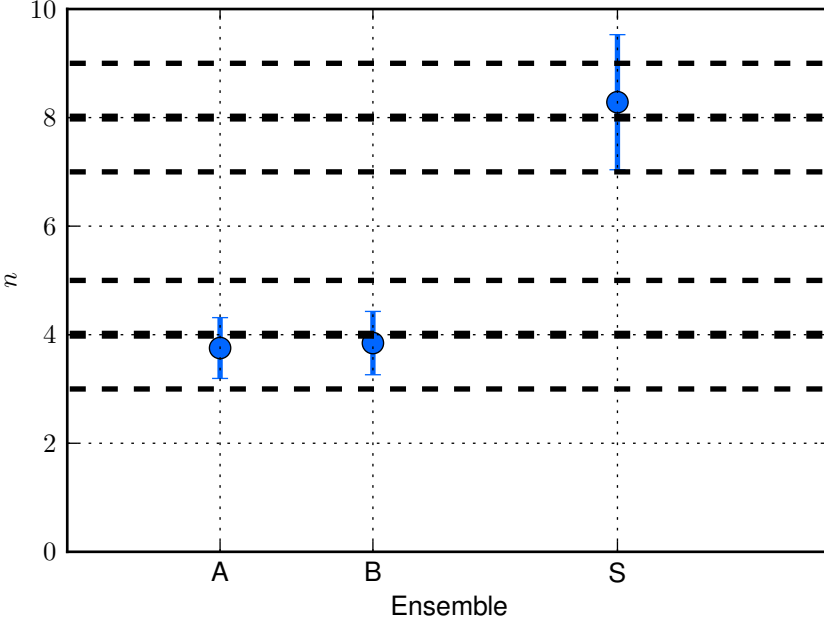


**Figure 4.11:** Visualization of the uncertainty in the results from fitting the resonant phase shifts in the two-mode and single-mode regime. The exact fit results are  $n_{A,B} = 3.8 \pm 0.6$  and  $n_S = 8.3 \pm 1.2$

respectively. The best fit for the two resonant modes results in  $n_A = 4$  and  $\Gamma_{\varphi,A} = 2\pi \cdot 54$  MHz, and  $n_B = 4$  and  $\Gamma_{\varphi,A} = 2\pi \cdot 41$  MHz (see solid line Figure 4.10 (b)). Again, the dephasing time is of the order of several ns. The number of qubits is half the number for each resonant mode compared to the single resonant mode. With high probability, the ensemble of the single resonant mode is formed by the overlapping of ensembles A and B.

### Error estimation

By varying the fixed parameters  $g_{j_3}$  and  $\Delta_j$  within their error bounds while fitting, an estimate of the error for  $n$  can be given (see Figure 4.11). Note, that the dephasing rate is insensitive to such variation of the fixed

parameters, once again showing that dephasing and number of qubits are independent to a certain degree. The uncertainty for ensembles A and B is  $\pm 0.6$ , therefore it can be considered as sure that those ensembles contain 4 qubits each. The uncertainty for ensemble S is slightly higher, resulting in  $n_S = 8 \pm 1$ . Yet, as the number for A and B is fixed and ensemble S is assumed to result from merging of ensembles A and B, it can be concluded that  $n_S = 8$ .

### Inhomogeneous broadening

In the model describing the system it is assumed that the ensembles consist of identical spins. It has been shown, that the spread directly in resonance is allowed to be within the range of the dephasing rate in order to form a single resonant mode. Here, the dephasing was found to be 50 MHz. The spread in the gaps of the qubits within one ensemble is allowed to be higher, in this case in the range of 100 MHz. If it is equal to or exceeds this value, the resonance will be broadened, as it occurs in the data directly in resonance (see Figure 4.12). The theoretical curve appears to be slightly narrower and lower in amplitude than the experimental data, which is a direct consequence of the assumption of identical qubits. The two resonant modes show less broadening, still the theoretical curve does not account for the whole magnitude of the resonant phase shift.

### 4.3.2 The higher harmonics

Even in state 2 only a single resonant mode is observed in the higher harmonics. This results from the convergence of A and B for high critical currents  $I_p$ . The coupling to the 5th harmonic is  $g_{j5} = 2\pi \cdot (1.56 \pm 0.14)$  MHz. The coupling is higher than the coupling to the third harmonic, because of the higher zero-point current. However, the effective coupling of the qubits in the resonant mode is reduced by  $\Delta_j/\omega_{q,j}$  making the coupling identical. The magnitude of the phase shift is still reduced, which results from the higher dephasing of the qubits, which increases with the detuning from their symmetry point. Applying the same procedure as before, fitting the resonant phase shift with  $n$  and  $\Gamma_\varphi$  as free parameters

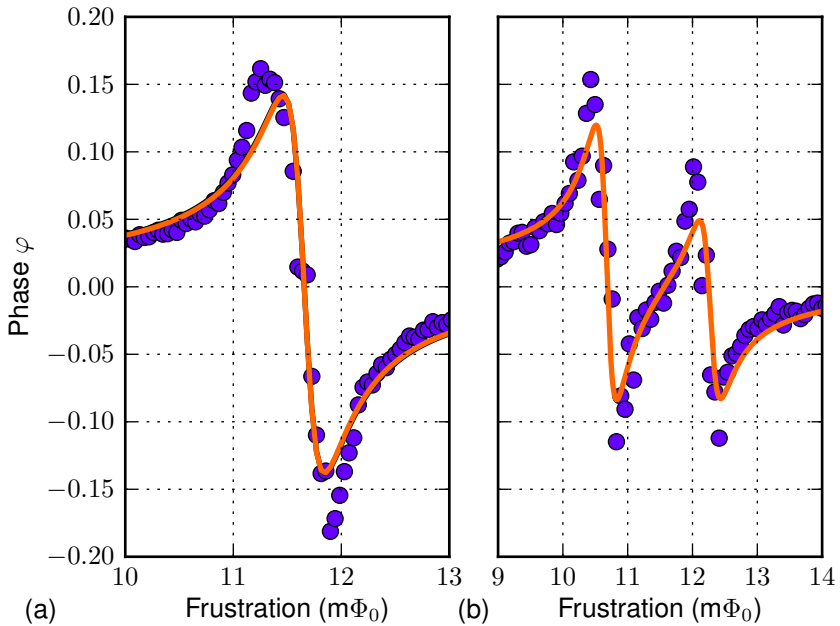


**Figure 4.12:** Close up of the single resonant mode (a) and the two resonant modes (b) taken from Figure 4.10. The fitted curves (solid lines) deviate directly in the resonance. This is a consequence of the spread of parameters in the qubit system, which is not reflected in the current model.

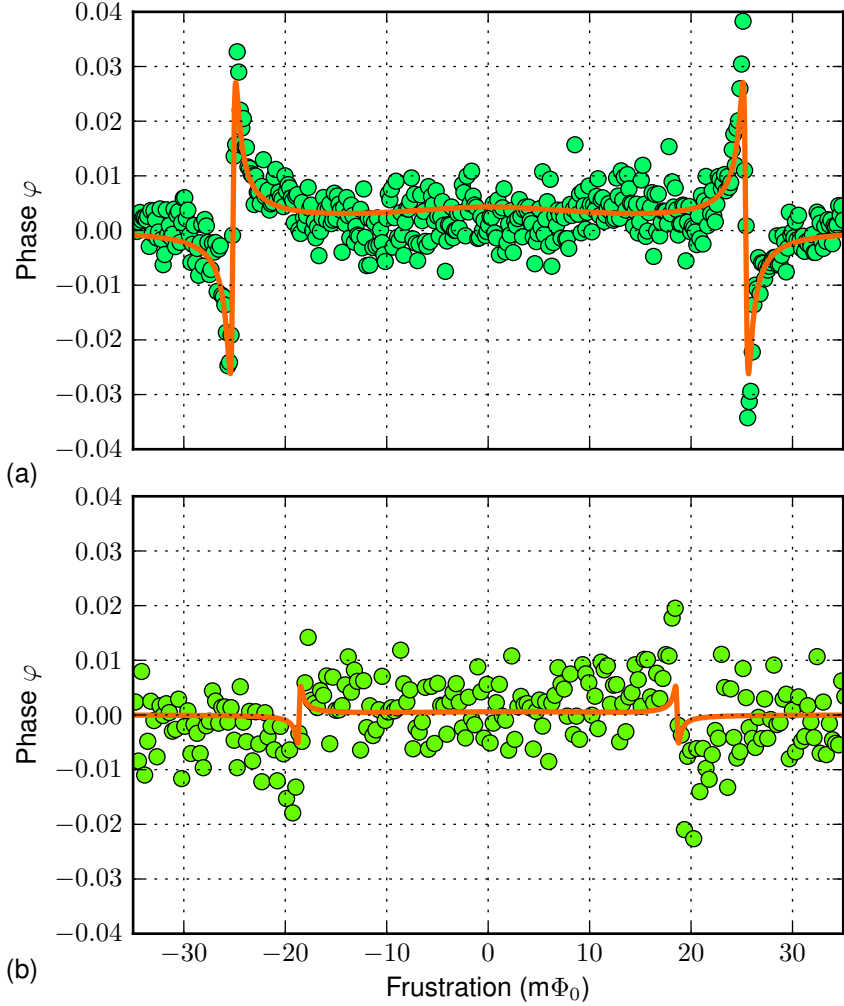


**Figure 4.13:** (a) The resonant phase shift between the qubits and the 5th harmonic of the resonator. The solid line shows the theoretical curve for ensemble S. (b) The resonant phase shift between the qubits and the 4th harmonic of the resonator. The solid line shows the theoretical curve for 8 qubits.

yields  $n = 9$  and  $\Gamma_\varphi = 2\pi \cdot 109$  MHz (see Figure 4.13 (a)). The uncertainty in  $n$  is  $\pm 1.5$ , so it is likely that again 8 qubits participate in this resonant mode.

The data taken for the transmission at the 4th harmonic frequency  $\omega_{r,4}/2\pi$  has a low signal-to-noise ratio (see Figure 4.13 (b)). Nonetheless, the position of the resonant mode can be detected. Note, that the magnitude is more than one order of magnitude less than for the phase shift observed in  $\omega_5$ . Fitting the data is not useful. Instead, the theoretical curve with a dephasing  $\Gamma_\varphi = 2\pi \cdot 82$  MHz and  $n = 8$  is shown. The coupling is  $g_{j5} \approx 0.6$  MHz.

### 4.3.3 Two stable states

The system exhibits two stable states, formerly referred to as state 1 and state 2. Here, the dependence on time is described and the stability over time of those two states is shown.

In principle, the system is stable in one of those two states over hours and days. A couple of times during a measurement run a transition from the one resonant mode to two resonant modes is observed or vice versa. This is what is meant by referring to two different states of the system.

Figure 4.14 (top panel) shows the development of the system over time. The phase at the third harmonic signal frequency was continuously monitored around a fixed frustration point. In the beginning of the measurement the system is in the state of a single resonant mode. Each single trace is averaged over a period of 3 minutes. The cryostat and the test setup are left undisturbed and no parameters are varied. After about 45 min the transition starts.

First, the magnitude of the resonant mode is reduced. Subsequently, the qubits start to decouple from each other and a state of several resonances is reached. At the end, the system settles in the state of two resonant modes. The full process takes several minutes, such being very short compared to the overall time scale (see Figure 4.14 (bottom panels)). Once the transition is completed the system is again stable over time.

There are two possible reasons for the occurrence of this transition. The properties of the qubit ensemble may change either due to local changes in the magnetic environment or due to a non-magnetic influence of the

qubit-parameters. The time dependence could be a very slow drift in a non-uniform magnetic field-gradient over the area of the qubit array. This gradient shifts the two sub ensembles A and B together when present. As long as the detuning between the two sub ensembles A and B is less than the dephasing rate they form a collective system. Yet, the effect of trapping vortices at such low temperatures is rather unlikely, and rearranging the qubits from ensembles A and B by a single magnetic field in such a way, that they overlap symmetrically, is not possible. Non-magnetic changes to the gap of the qubits could arrive from its sensitivity to charges, for small ratios of  $E_j/E_c$  the gap depends on the voltage across the smallest junction. It is currently under investigation to which degree the gap might change due to charge noise. An important question is, whether the change arrives from several qubits changing their parameters simultaneously or a single qubit which mediates an effective coupling between ensembles A and B and therefore leads to their collective interaction.

### 4.4 Strong driving and tuning the metamaterial

So far, the probe signal amplitude was kept sufficiently small to guarantee that the average number of photons in the resonator is below unity. Here, the behaviour of the metamaterial in dependence on the probe or driving power, i.e. in dependence on the photon number  $N$ , is studied. In the first and last part of this section the dependence on the probe power is analysed. Multiphoton transitions induced by the strong probe signal are discussed. The data confirms certain properties of the qubit system in an independent measurement (see subsection 4.4.1). The last part reveals the occurrence of photon number dependent resonances around the degeneracy point of the qubits (see subsection 4.4.3).

As already seen in subsection 4.2.1, off-resonant microwave radiation couples only weakly to the qubits. Thus, the harmonics are exploited in order to strongly drive the metamaterial. In subsection 4.4.2 two-tone experiments, in which one signal is used to dress the system (similar to section 3.4), are discussed. This method allows for additional control over the metamaterial and underlines the quantum nature of the system.

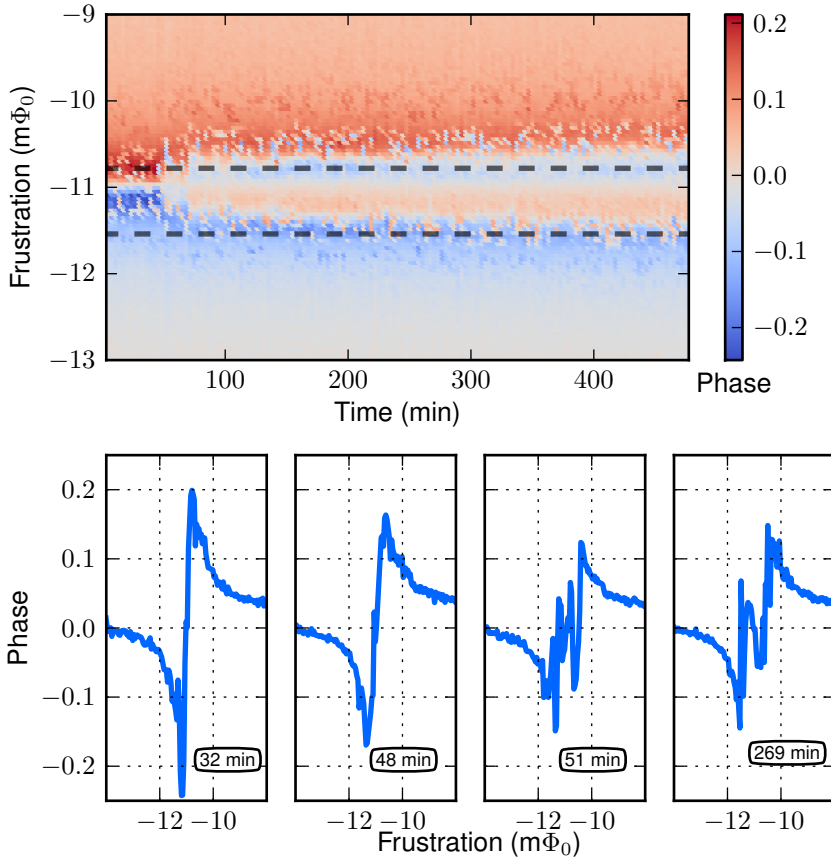


**Figure 4.14:** (top panel) The two states of the system over a time of 7 hours. A transition from the state of a single resonant mode to the state of two resonant modes is observed. The black dashed lines are guides to the eyes. (bottom panels) Single traces from the time dependence. At  $t = 0$  min (very left) and  $t = 323$  min (very right) the two stable states are shown. The two traces in the middle demonstrate the transition from a single resonant mode (left) to two resonant modes (right).

For instance, the metamaterial can be tuned in and out of resonance with the harmonics of the resonator.

The rotating wave approximation (RWA), which is used for the analysis of the data presented here, is valid up to the critical photon number  $N_{crit} = (\Delta_j/2g_{jm})^2$  [BHW+04]. In dependence on the harmonic of the resonator used for driving the system, this can be up to several million photons, before deviation from the RWA could be observed.

### 4.4.1 Multiphoton processes

In the following experiment the probe power is increased in order to populate the resonator with a higher photon number. Figure 4.15 (a) displays the dispersive shift while the system is probed strongly at the fundamental mode frequency  $\omega_{r,1}/2\pi$ . The two resonances which appear correspond to an excitation of ensembles A and B. The first transition of this kind appears at a qubit transition frequency of  $\omega_q = 3 \cdot \omega_{r,1}$ . The two-photon resonance does not occur, because the qubit gaps are above  $2 \cdot \omega_{r,1}$ . The full dependence on the probe power is shown in Figure 4.16. Above a certain probe power the excitation of the qubits by a combination of  $m \omega_1$  photons is observed. The theoretical curves for the resonances are plotted for ensembles A and B. It is possible to follow the three-photon resonance at lower powers, whereas the resolution is too low to distinguish between several overlapping resonances at higher powers. Some features, like the disappearance of resonances and appearance of strong resonances can be explained by following the theoretical curves. The principle occurrence of higher order multiphoton transitions is visible.

In the next step, the resonator is still driven at the fundamental mode frequency  $\omega_{r,1}/2\pi$ , yet weakly probed at the third harmonic frequency  $\omega_{r,3}/2\pi$  (see Figure 4.15 (b)). In addition to the resonant modes  $\omega_{q,A,B} = \omega_{r,3}$  discussed before, secondary resonant phase shifts appear at higher frustration due to the population of  $\omega_{r,1}$  photons. Their position corresponds to  $\omega_{q,A,B} = 4 \cdot \omega_{r,1}$ . The qubit ensembles are excited due to multiphoton transitions, which can be observed in the probe signal, as the phase shift depends on the qubits states. Here, in contrary to the experiment where the transmission at  $\omega_{r,4}$  was measured directly, two

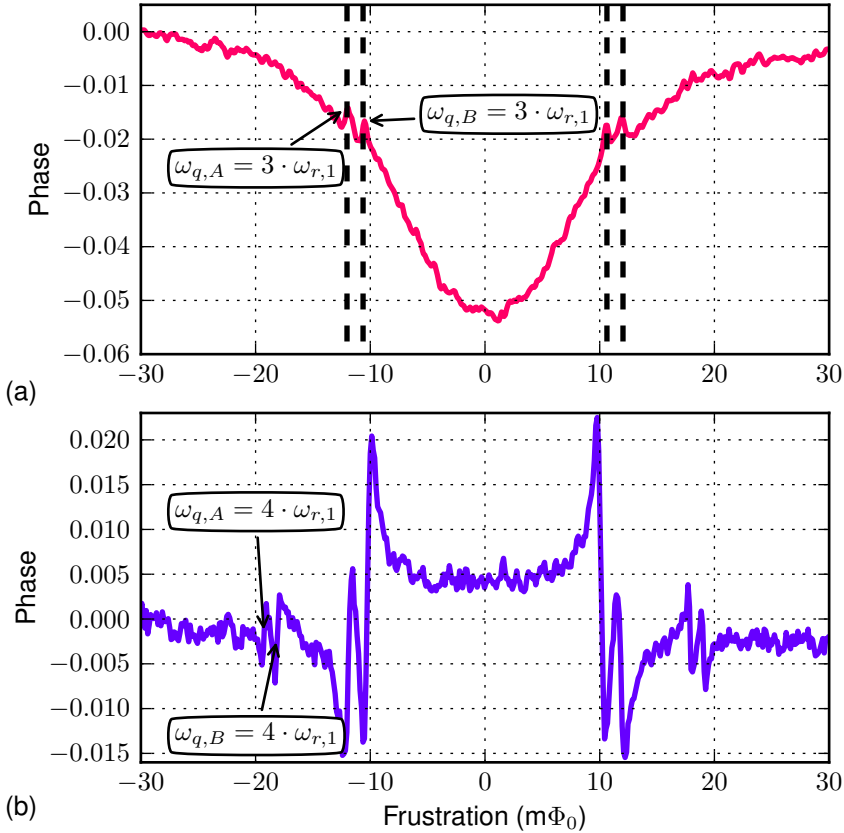


**Figure 4.15:** (a) In the upper panel the system is probed and driven at the fundamental mode frequency  $\omega_{r,1}/2\pi$ . The driving power yields a photon number high enough in order to induce multiphoton transitions. The two resonances marked by the dashed black lines appear at the transition frequencies  $\omega_{q,A,B} = 3 \cdot \omega_{r,1}$ . (b) The system is driven at  $\omega_{r,1}$  and weakly probed at the third harmonic frequency  $\omega_{r,3}$ . The outer resonant phase shifts appear at transition frequencies  $\omega_{q,A,B} = 4 \cdot \omega_{r,1}$ .

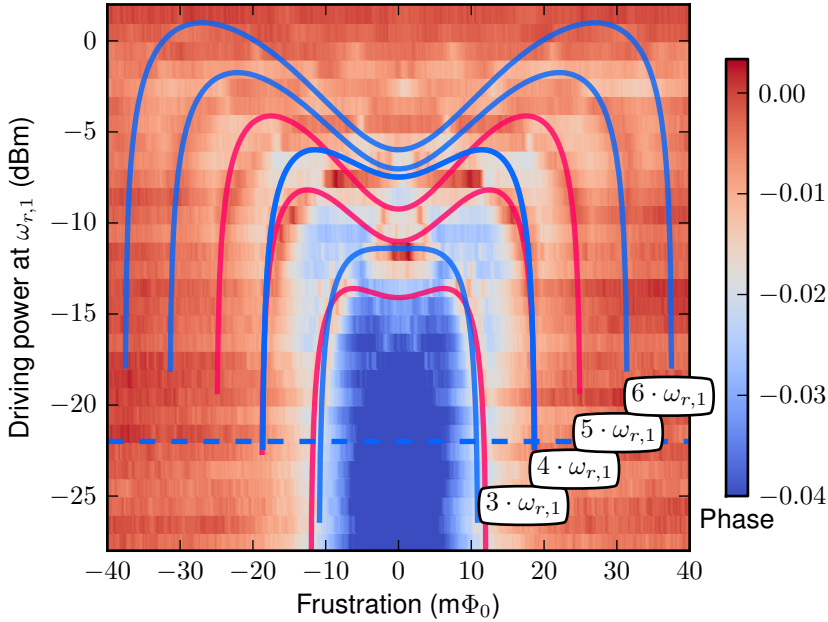


**Figure 4.16:** The dependence of the dispersive shift at the fundamental mode frequency on the probe power. The shading corresponds to the phase signal. The solid lines show the theoretical dependence on the multiphoton resonances for ensembles A (red) and B (blue). The damping in the line at the fundamental mode frequency is extracted to be 67.5 dB. The blue dashed line indicates the single trace taken for Figure 4.15 (a).

separate resonances are observed at  $4 \cdot \omega_{r,1}$ . Yet, this possibility has already been included in the error margin of the ensemble parameters, and if taken into account, does not modify but confirm the ensemble spectra extracted in subsection 4.2.2. The question remains, whether the ensembles are excited collectively or not.

#### 4.4.2 Tuning of the qubit ensembles

By driving the metamaterial in an additional mode  $m$  the transition frequencies acquire a pull which depends on the photon number  $N$ . This

is comparable to the AC-Zeeman shift, which is the only possibility to tune natural occurring spin ensembles [PRW+13]. In this thesis, it has already been discussed for a single qubit in subsection 3.4.2 and theoretically for a multi-qubit system in subsection 2.2.4. The shift is opposed on each qubit individually while the qubit frequencies are shifted in dependence on the sign of the qubits-resonator detuning  $\delta_{jm} = \omega_{q,j} - \omega_{r,m}$  to either higher or lower frequencies. The driving process can be separated from the probing process. First, the system is considered to be under drive by  $N_m$  photons at the driving frequency, which shifts the qubit parameters by the AC-Zeeman shift as

$$\tilde{\omega}_q = \omega_q + 2 \frac{N_m \cdot g_{\epsilon,m}^2}{\omega_q - \omega_m}. \quad (4.3)$$

Subsequently, the re-normalized system is probed and, depending on the regime, a dispersive shift or resonant modes at the probe frequencies can be observed.

#### Transition from the dispersive regime to the resonant regime

While strongly driving the system at the third harmonic frequency  $\omega_{r,3}/2\pi$  and weakly probing at the second harmonic frequency  $\omega_{r,2}/2\pi$  at small photon numbers, the pure dispersive shift is observed, as all qubit splittings are above the resonator mode. The qubits-resonator detuning  $\delta_{qr}$  is negative. Consequently, the qubit energies decrease with increasing driving strength. As soon as  $\tilde{\omega}_q < \omega_{r,2}$  is reached, a resonant mode appears (see Figure 4.17 (a)). This happens at first for ensemble A. At higher driving powers a second resonant mode corresponding to ensemble B appears (data not shown). The position of the resonant phase shift follows the resonance condition  $\omega_{r,2} = \tilde{\omega}_{q,A}$  (see Figure 4.18). The axis on the left-hand side indicates the power in dBm of the driving signal at the generator, the damping in the line has been extracted from the comparison to the theoretical curve to be 82.2 dB, which is in accordance with the estimation from the calibration of the measurement setup. Consequently, the photon number in the resonator can be extracted, as shown on the right y-axis. In Figure 4.17 (b) a scheme of the energy level for two different photon numbers is shown. At low driving power, the transition

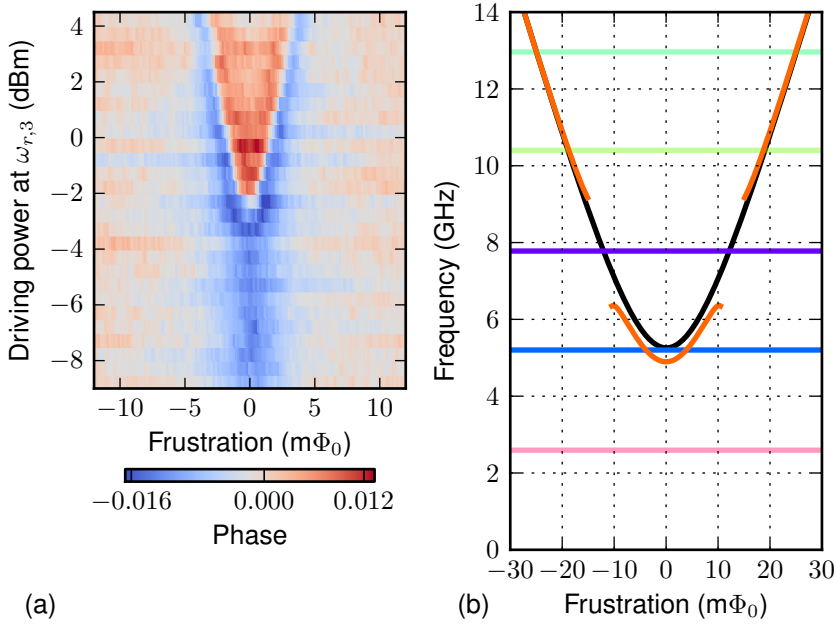


**Figure 4.17:** (a) The phase of the transmission (shading) in dependence on the driving power at a frequency of  $\omega_{r,3}/2\pi$  and a probe frequency of  $\omega_{r,2}/2\pi$ . At low driving powers the metamaterial is in the fully dispersive regime, whereas at higher powers two resonant modes appear. A single trace of the resonant mode is depicted in Figure 4.19. (b) The level diagram of the system. The horizontal lines correspond to the harmonics of the resonator. In its initial condition, the qubit ensemble is above the second harmonic frequency (black line). While driven with  $N_3 = 300 \cdot 10^3$  photons at the third harmonic frequency the qubit ensemble is shifted below the second harmonic mode (orange line).

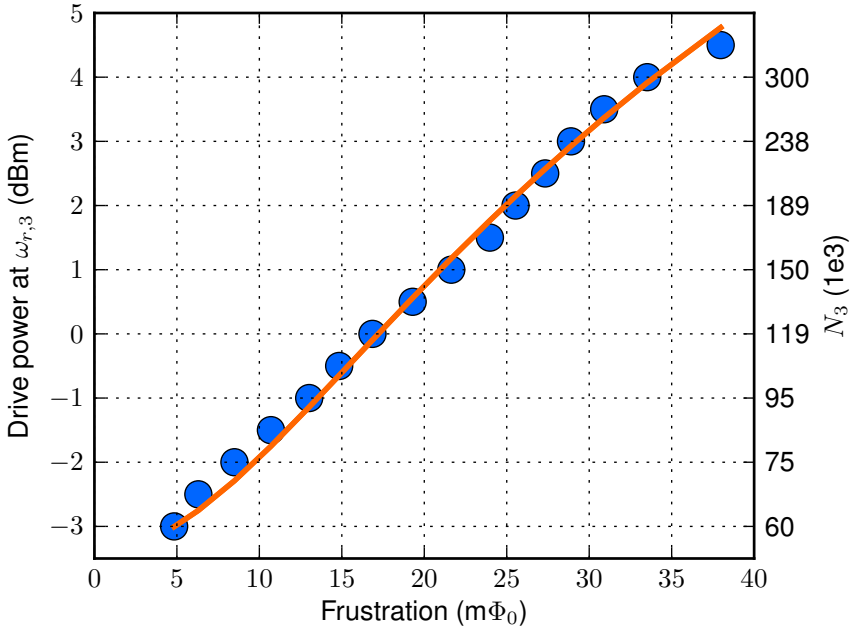


**Figure 4.18:** The position of the resonant phase shift in the second harmonic signal in dependence on the driving power in the third harmonic frequency  $\omega_{r,3}/2\pi$  as extracted from Figure 4.17 (a). The solid line shows the theoretical curve following the resonance condition  $\omega_{r,2} = \tilde{\omega}_{q,A}$ . The right y-axis indicates the corresponding photon number  $N$  in the driving field.

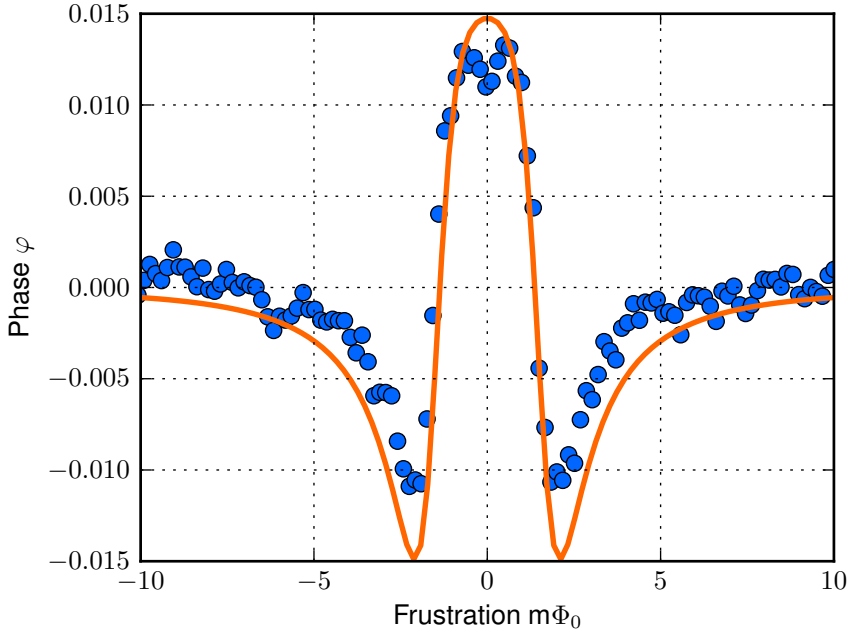


**Figure 4.19:** The resonant mode observed in the phase transmitted at the second harmonic frequency  $\omega_{r,2}/2\pi$ . The metamaterial is continuously driven at the third harmonic frequency  $\omega_{r,3}/2\pi$  with a photon number  $N_3 = 75 \cdot 10^3$ . The solid line shows the theoretical curve. The data is taken from the cross-section from Figure 4.17 (a) at a driving strength of -1 dBm.

frequency of the ensemble is still undisturbed. At a photon number of  $N_3 = 300 \cdot 10^3$  the minimal transition frequency lies below the second harmonic frequency. So, the ensemble is crossing the resonator mode and a resonant phase shift can be observed. Note, that the shift is only valid in the dispersive regime of the driving field. Therefore, the line of the shifted system is interrupted around the driving frequency. A resonant mode of the system at the second harmonic is depicted in Figure 4.19. The qubit ensemble is continuously driven at a photon number  $N_3 = 75 \cdot 10^3$ . All parameters of the system are known, there are no free parameters. The agreement between data and theoretical curve, as calculated from Equations (4.3) and (2.30), for ensemble A continuously driven at  $N_3$  is good. Hence, the previously extracted parameters can be considered as confirmed by this measurement, as there are the ensemble parameters (see subsection 4.2.2), the number of qubits (see subsection 4.3.1) and the coupling to the second harmonic  $g_{j2}$  (see subsection 4.2.3).

#### Transition from the resonant to the dispersive regime

When the system is driven at the fundamental mode frequency  $\omega_{r,1}/2\pi$  and probed at third harmonic frequency  $\omega_{r,3}/2\pi$ , the effective qubit frequencies  $\tilde{\omega}_q$  increase with increasing driving power. As a consequence, the two resonant modes approach until they converge and disappear. At that point the qubit frequencies excess  $\omega_{r,3}/2\pi$  (see Figure 4.20 (a)). The position of the resonant phase shift follows the resonance condition  $\omega_{r,3} = \tilde{\omega}_{q,j}$ . Figure 4.21 shows the measurement data in comparison to the theoretical curve for ensemble B. The axis on the left-hand side indicates the power of the driving signal at the generator, the damping in the line has been extracted to be 68 dB. This is in good agreement with the estimation from the measurement setup. In Figure 4.20 (b) a scheme of the energy levels for two different photon numbers is shown. At low driving power, the transition frequencies of the ensembles are still undisturbed. At a photon number of  $N_1 = 16 \cdot 10^6$  the minimal transition frequency lies above the third harmonic frequency. Therefore, there is no crossing between the qubits and the resonator mode and the resonant phase shift disappears.

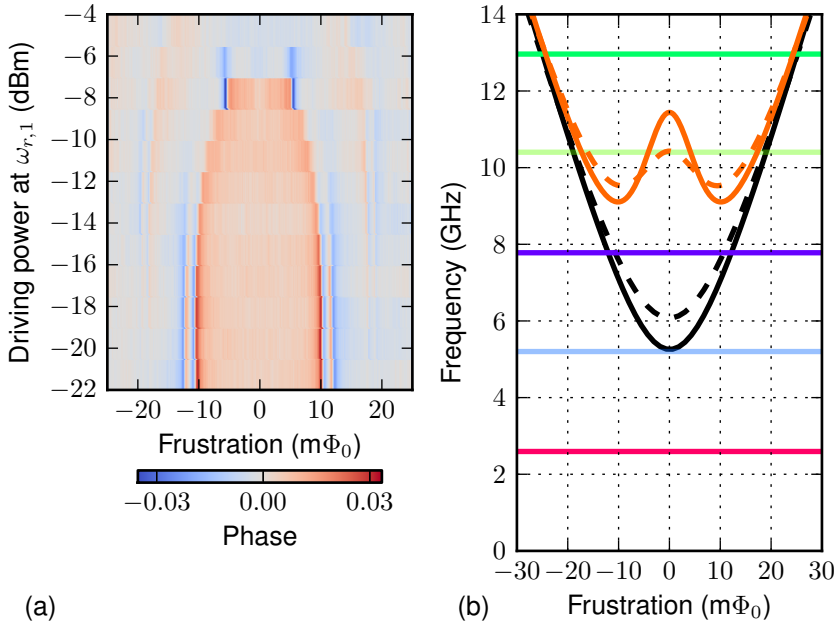


**Figure 4.20:** (a) The phase of the transmission (shading) in dependence on the driving power at a frequency of  $\omega_{r,1}/2\pi$  and a probe frequency of  $\omega_{r,3}/2\pi$ . The single trace shown in Figure 4.15 (b) is taken from this data set. At low driving powers the metamaterial is in the resonant regime exhibiting two resonant modes. At the highest driving power, the resonant modes disappear and the metamaterial is in the fully dispersive regime. (b) The horizontal lines correspond to the harmonics of the resonator. In its initial condition the qubit ensembles are below the third harmonic frequency (black lines). At a photon number of  $N_1 = 16 \cdot 10^6$  in the driving field, which corresponds to a driving power of  $-5$  dBm, the lowest transition frequencies of both ensembles are clearly above the third harmonic frequency (orange lines).

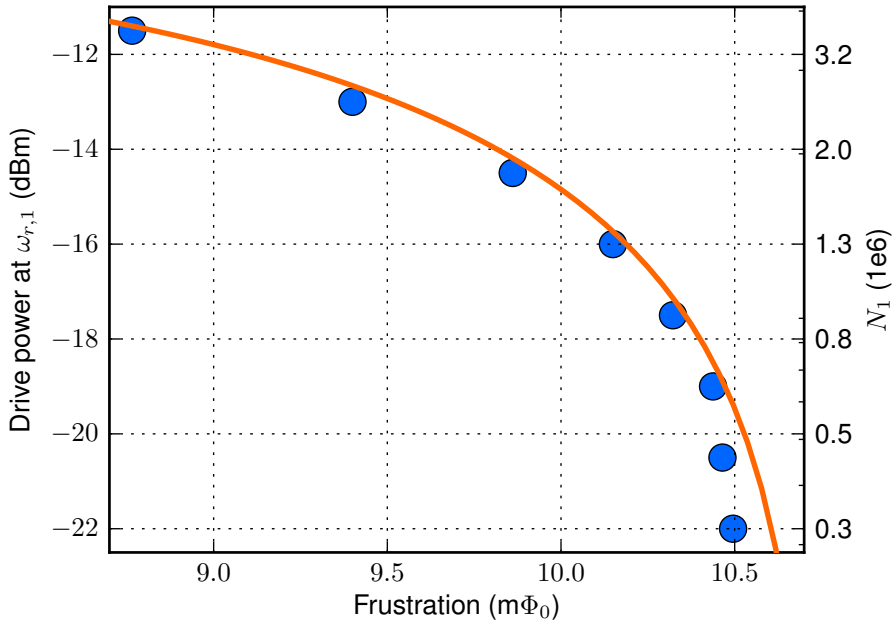


**Figure 4.21:** The position of the inner resonant mode (ensemble B) in  $\omega_{r,3}$  in dependence on the driving power in  $\omega_{r,1}$  extracted from Figure 4.20 (a). The solid line shows the theoretical curve following the resonance condition  $\omega_{r,3} = \omega_{q,B}$ . The right y-axis indicates the corresponding photon number in the driving field.

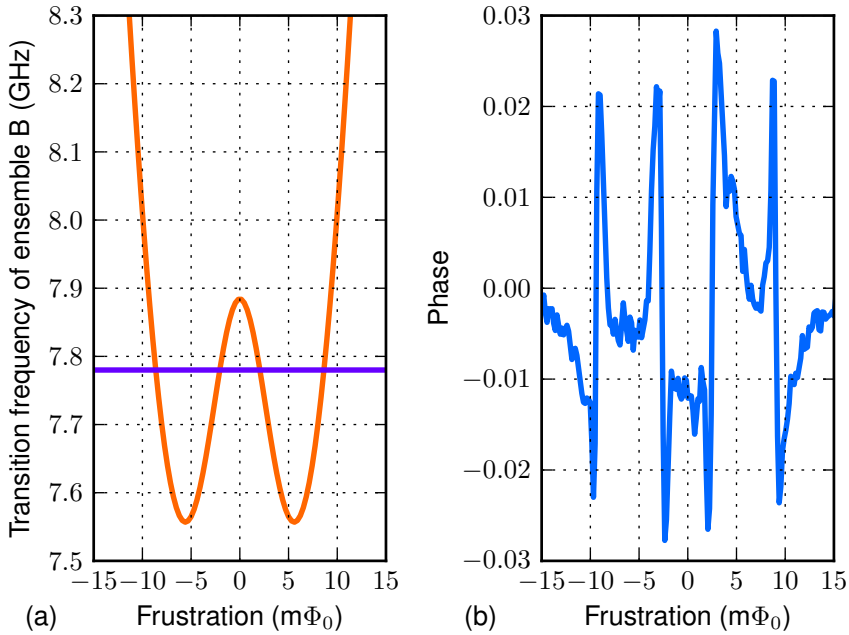


**Figure 4.22:** (a) The qubit energies of set B under continuous drive at  $\omega_{r,2}$  with a photon number of  $5 \cdot 10^6$ . The solid line corresponds to the third harmonic  $\omega_{r,3}$  which is crossed four times by the qubit ensemble. (b) The experimental curve for the case depicted in (a). Four resonant modes are observed.

### Non-linearity of the shift

The shift as described by Equation (4.3) depends on the effective coupling  $g_\epsilon$  which in turn depends on the detuning of the qubit from its symmetry point. Therefore, the frequencies are shifted non-linearly (see Figure 4.22 (a)). In the degeneracy point the shift is strongest, because there the coupling is fully transversal. Interestingly, the occurrence of four resonant modes at a certain driving strength is expected. Indeed, this could be confirmed while driving at the second harmonic frequency  $\omega_{r,2}/2\pi$  and probing the phase at third harmonic frequency  $\omega_{r,3}/2\pi$  (see Figure 4.22 (b)). The driving signal contains roughly 5 million photons.

### Conclusion

The method presented allows for additional tuning of the flux qubits beyond the limitation of their minimal transition frequency. In principle, within this section the coupling of a flux qubit ensemble close its symmetry point to a resonator has been demonstrated, which is similar as in [FFM+10]. Yet, the photon number in the driving field may fluctuate, which will lead to additional dephasing due to photon shot noise [SWB+05], which may limit the application.

### 4.4.3 Additional effects

The model developed for the transmitted phase is valid only for a small driving signal and a single excitation in the system. In order to analyse its behaviour in dependence on the driving signal and its robustness in the last experiment, the qubit metamaterial is both driven and probed at the third harmonic frequency of the resonator  $\omega_3/2\pi$ . The transmitted phase is monitored, while the probing strength, corresponding to the photon number in the resonator, is increased. Figure 4.23 shows the results in logarithmic and linear scale. The damping at the third harmonic mode was previously extracted to be 82.2 dB, here, the probe signal is attenuated by 20 dB more. This is used to recalculate the photon number in the resonator.

In the beginning, at the single photon level, the two resonant modes are observed. At higher photon numbers the magnitude of the resonant phase shifts diminishes and the curve is broadened. In the vicinity of the resonant modes additional resonances appear at a driving field of several hundreds of photons. At even higher photon numbers resonances at the degeneracy point of the qubits appear, which follow a hyperbolic-like dependence on the photon number. The origin of those resonances is still under investigation.

The quantitative description applied to analyse the resonant modes is only valid for small driving signals. Still, the data can be fitted according to Equation (2.30) for arbitrary driving strength. The product  $ng^2$  and the dephasing  $\Gamma_\varphi$  are taken as free parameters. As long as the driving field is below a single photon,  $ng^2$  is approximately constant (see Figure 4.24

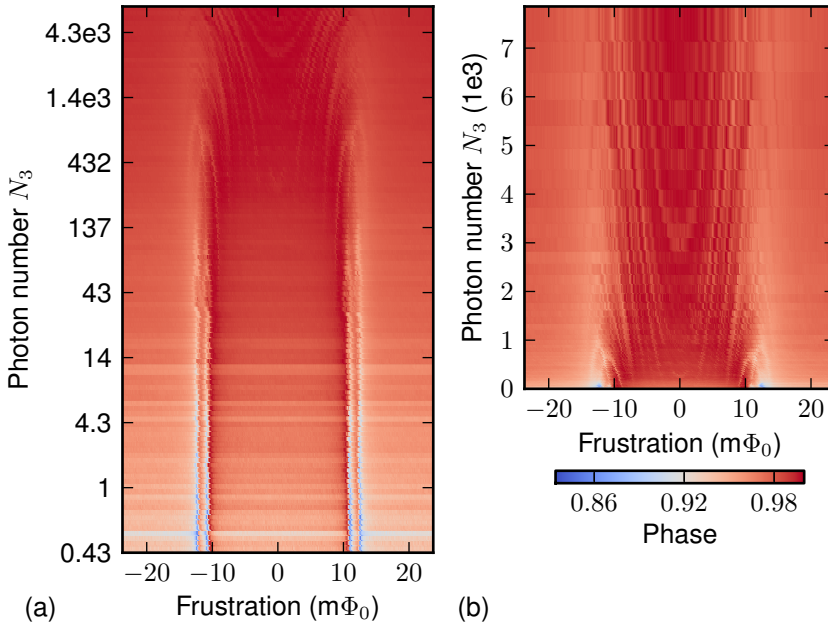


**Figure 4.23:** The phase transmitted through the system under strong drive at the third harmonic frequency  $\omega_3/2\pi$ . (a) The left panel shows the dependence on the photon number in a logarithmic scale. For low photon numbers the two resonant modes are visible. With increasing photon number they are fading away and additional resonances appear. (b) The right panel displays the same data in a linear scale, highlighting the effects at higher photon numbers.

(a)). In the region between 1 and 10 photons, the product starts deviating from its initial value. The dephasing rate shows similar characteristics, whereas it increases significantly for photon numbers above 10 (see Figure 4.24 (b)). Indeed, the model seems to be robust for small photon numbers, especially for  $N < 1$ . At higher photon numbers the model still fits the data well and the parameters extracted could be used as phenomenological values in order to describe the system. In the region between 50 and 90 photons, the two resonant modes approach, which can be seen in the correlated fit results for both ensembles in the product  $ng^2$ .

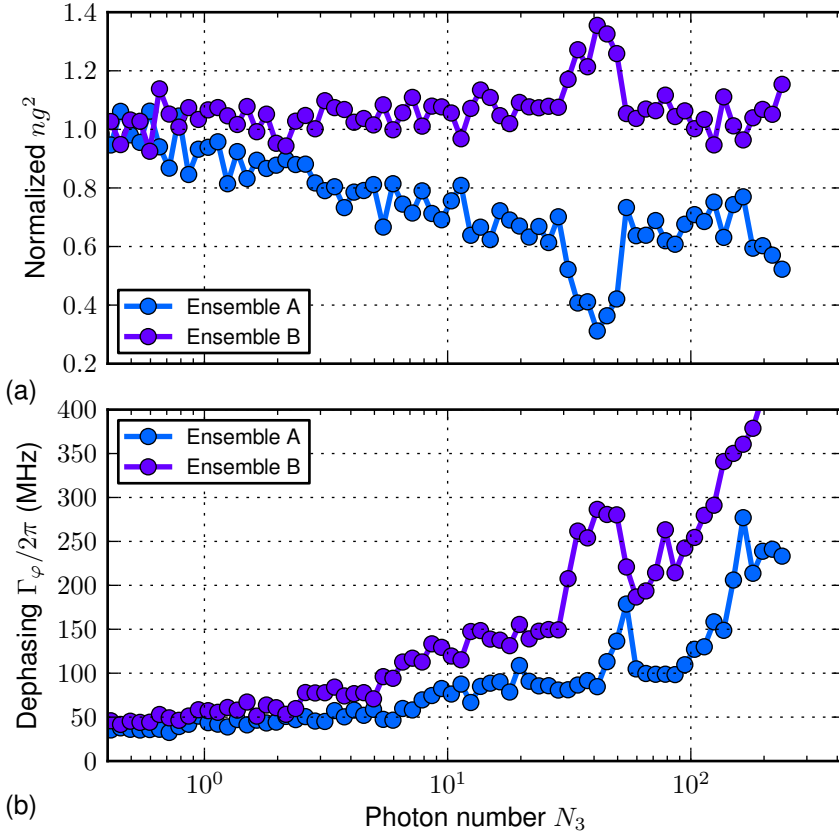


**Figure 4.24:** Fitting the measurement data from Figure 4.23 according to Equation (2.30) with the product  $ng^2$  and the dephasing  $\Gamma_\phi$  as free parameters. (a) The fitting results for  $ng^2$  normalized to its value at the lowest photon number. (b) The fitting results for the dephasing  $\Gamma_\phi$ .



## 5 Conclusion

In this thesis, superconducting quantum bits (qubits) weakly coupled to a superconducting high quality cavity have been analysed in order to systematically develop a many-qubit system to be used as a quantum metamaterial. Such a metamaterial offers the possibility to engineer the propagation of light by tuning the transition frequencies of its atoms and the atom-atom coupling either by design or *in situ* in the experiment.

Here, the weak coupling bears certain advantages. For instance, the driven qubit exhibits a level splitting, whose magnitude, the Rabi frequency, depends on the photon number of the driving field. Because of the weak coupling high photon numbers are required to strongly drive the qubit, making the difference between neighbouring photon number manifolds negligible and allowing to average over the photon number. Such, the dressed states of the driven system can be reduced to an effective two-level system, whose population depends on the detuning between the qubit and the microwave drive. This has led to the demonstration of dressed state amplification with a single superconducting flux qubit. When coupling many qubits to the cavity, the weak coupling prevents the occurrence of strong single qubit resonances and makes only collective resonances visible. Therefore, even in the presence of a spread in parameters, the system remains understandable, which is important for this first implementation of a many-qubit system, a so-called quantum metamaterial.

The first part of this thesis (see chapter 3) concentrates on the behaviour of a single flux qubit in the fully dispersive regime, where the qubit frequency is below the resonator frequency. The phase transmitted at the resonator frequency exhibits a dispersive shift in dependence on the qubit frequency and its state. This has been used to characterize the qubit and extract all relevant parameters. Subsequently, increasing the power of the probing field has been shown to induce multi-photon transitions and to

alter the qubit transition frequency by the AC-Zeeman shift. Furthermore, a second microwave field has been applied in order to dress the qubit. It has been argued, that the dressed system exhibits a level inversion in dependence on the detuning between the qubit and the microwave drive. When probing the dressed system, an amplification of the transmitted signal of up to 40 % has been observed.

In the second part of the thesis (see chapter 4), the system is extended to many qubits: 20 flux qubits have been embedded in a single superconducting resonator. This system constitutes the first implementation of a basic quantum metamaterial in the sense, that many artificial atoms are coupled to the quantized mode of a photon field. The different harmonics of the resonator are exploited in order to test the system at different frequencies. The dispersive shifts measured at the first two harmonics are induced by all qubits collectively and serve to make first estimations of the parameters of the metamaterial. It is found, that not all qubits contribute equally to the dispersive shift. By using the resonant modes observed in the higher harmonics of the resonator, the parameters of three different ensembles of identical qubits could be reconstructed. A quantitative analysis of the resonant modes has revealed that two ensembles are formed by 4 qubits each and the third by not less than 8 qubits. Indeed, the system exhibits a time dependence, where the third ensemble is formed by an overlapping of the two other ones. The metamaterial consists of artificial two-level systems similar to natural spins and just like them, their transition frequency can be tuned by the AC-Zeeman shift, as shown before. Here, this has been used to tune the quantum metamaterial in and out of the fully dispersive regime, which underlines the quantum mechanical nature of the system. The consistency of all extracted parameters could be demonstrated.

The next iteration of the quantum metamaterial will have on-chip bias lines which couple non-uniformly to the qubits and allow to locally control the frustration and therefore the transition frequency of individual qubits. Such, the number of qubits participating in the resonant modes can be tuned in a controlled way and as a consequence, the collective coupling can be tuned. Once the coupling becomes of the order of the qubits level splitting and the resonator frequency, the occurrence of a quantum phase transition is likely [NC10].

# Zusammenfassung

In dieser Dissertation wurden supraleitende Quantenbits (Qubits) untersucht, welche schwach mit einem supraleitenden Resonator hoher Güte gekoppelt sind. Die Experimente dienen der systematischen Entwicklung eines Multi-Qubit-Systems, welches als Quantenmetamaterial eingesetzt werden kann. Ein solches Metamaterial bietet die Möglichkeit, die Ausbreitung von Licht zu manipulieren, indem die Übergangsfrequenzen der Atome sowie die Atom-Atom-Kopplung entweder durch das Design oder während des Experiments *in situ* eingestellt werden.

Die schwache Kopplung im verwendeten System birgt verschiedene Vorteile, so erfährt etwa das getriebene Qubit eine Niveau-Aufspaltung, deren Stärke – die Rabi-Frequenz – von der Photonenzahl des Treibungsfeldes abhängt. Aufgrund der schwachen Kopplung sind hohe Photonenzahlen erforderlich, um das Qubit stark zu treiben. Damit wird der Unterschied zwischen benachbarten Photonenzahl Mannigfaltigkeiten in den vernachlässigbaren Bereich gedrängt. Hierdurch wird es möglich, über die Photonenzahl zu mitteln. Auf diese Weise können die bekleideten Zustände des getriebenen Systems auf ein effektives Zwei-Niveau-System reduziert werden, dessen Besetzung von der Verstimmung zwischen Qubit und Mikrowellentreibung abhängt. Die Signal Verstärkung mit Hilfe des bekleideten Zustandes konnte an einem einzelnen supraleitenden Qubit gezeigt werden. Werden mehrere Qubits mit einem Resonator gekoppelt, verhindert die schwache Kopplung das Auftreten starker Resonanzen einzelner Qubits. Nur kollektive Resonanzen sind sichtbar. Selbst bei einer starken Streuung der Parameter bleibt dadurch das System verständlich, was eine Grundvoraussetzung darstellt für die erste Realisierung eines Multi-Qubit-Systems, eines so genannten Quantenmetamaterials.

Der erste Abschnitt der Dissertation (Kapitel 3) konzentriert sich auf das Verhalten eines einzelnen Flussqubits im vollständig dispersen

Regime, in dem die Qubitfrequenz niedriger ist als die Frequenz des Resonators. Die Phase des durch den Resonator geleiteten Signals, weist eine dispersive Verschiebung auf, welche von der Frequenz des Qubits und von dessen Zustand abhängt. Das wurde ausgenutzt, um das Qubit zu charakterisieren und alle relevanten Parameter zu ermitteln. Anschließend konnte gezeigt werden, dass durch die Erhöhung der Leistung des Testfeldes Multiphotonenübergänge induziert werden und dass die Übergangsfrequenz des Qubits durch die AC-Zeeman-Verschiebung beeinflusst wird. Des Weiteren wurde ein zweites Mikrowellenfeld angelegt, um das Qubit in den bekleideten Zustand zu überführen. Das bekleidete System weist eine Besetzungsinversion auf, die von der Verstimmung zwischen Qubit und Mikrowellentreibung abhängt. Bei der Untersuchung des bekleideten Systems konnte eine Verstärkung des übertragenen Signals um bis zu 40 % festgestellt werden.

Im zweiten Abschnitt der Dissertation (Kapitel 4) wurde das System auf eine höhere Zahl von Qubits erweitert: zwanzig Flussqubits wurden in einen einzelnen supraleitenden Resonator integriert. Dieses System stellt die erste Verwirklichung eines einfachen Quantenmetamaterials dar, und zwar in dem Sinne, dass eine Vielzahl künstlicher Atome mit der quantisierten Mode eines Photonenfeldes koppeln. Die verschiedenen Harmonischen des Resonators werden ausgenutzt, um das System bei unterschiedlichen Frequenzen zu testen. Die dispersen Verschiebungen in den ersten beiden Harmonischen werden durch alle Qubits kollektiv verursacht. Sie dienen dazu, erste Abschätzungen der Parameter des Metamaterials vorzunehmen. Es wurde festgestellt, dass nicht alle Qubits im gleichen Maße zur dispersen Verschiebung beitragen. Unter Nutzung der resonanten Moden, die in den höheren Harmonischen des Resonators auftreten, konnten die Parameter dreier verschiedener Ensembles identischer Qubits rekonstruiert werden. Eine quantitative Analyse der resonanten Moden zeigte, dass zwei Ensembles aus jeweils vier Qubits bestehen und das dritte sogar acht Qubits umfasst. In der Tat zeigt das System eine Zeitabhängigkeit, wobei das dritte Qubit-Ensemble durch eine Überlappung der beiden anderen gebildet wird. Das Metamaterial besteht aus künstlichen Zwei-Niveau-Systemen, welche natürlichen Spins ähneln, und bei denen – genau wie bei letzteren – die Übergangsfrequenz durch die AC-Zeeman-Verschiebung eingestellt werden kann, wie es bereits vorher

gezeigt werden konnte. In diesem Fall wurde das ausgenutzt, um das Quantenmetamaterial in das und aus dem vollständig dispersen Regime zu schieben, was den quantenmechanischen Charakter des Systems unterstreicht. Die Konsistenz aller ermittelten Parameter konnte gezeigt werden.

In einem nächsten Iterationsschritt wird das Quantenmetamaterial Kontrolllinien auf dem Chip aufweisen, die nicht uniform an die Qubits koppeln. Dadurch ist es möglich, die Frustration und damit die Übergangsfrequenz der einzelnen Qubits zu steuern. Auf diese Weise kann die Zahl der in den resonanten Moden beteiligten Qubits kontrolliert eingestellt werden. Sobald die Kopplung die Größenordnung der Niveau-Aufspaltung der Qubits und des Resonators erreicht, ist ein Quantenphasenübergang wahrscheinlich [NC10].



# Appendix

## Experimental validation of the coupling

It has been already shown, that the theoretical mutual inductance is in good agreement with the experiment (see subsection 3.2.2). Here, the consistence between the experimentally extracted and the calculated coupling is validated one more time. The single qubit described in chapter 3 is analysed in a different measurement setup. The system is probed at the third harmonic of its resonator, in a similar way as shown for the metamaterial in subsection 4.3.1. The frequency of the third harmonic is  $\omega_3/2\pi = 7.77$  GHz and  $\kappa_3 = 0.46$  Mhz. The dimension and location of the single qubit differs from the ones used in the metamaterial, which results in a slightly higher mutual inductance  $M_{qr} = (0.92 \pm 0.02)$  pH. The gap and the persistent current are  $\Delta = 3$  GHz and  $I_p = 158$  nA. The expected coupling is  $g_{qr} = 2\pi \cdot (4.7 \pm 0.3)$  MHz. Figure .1 shows the phase of the transmission through the resonator. Similar as for the metamaterial two symmetric resonance phase shifts occur. The solid line shows a two-parameter fit with  $g_{qr}$  and  $\Gamma_\varphi$  as free parameters using Equation (2.30) for  $n = 1$ . The best fit is obtained for  $\tilde{g}_{qr} = 2\pi \cdot 4.9$  MHz and  $\Gamma_\varphi = 2\pi \cdot 141$  MHz. The experimental result for the coupling is in good agreement with the theoretical value. The higher dephasing results from the larger detuning of the flux qubit from its degeneracy point.

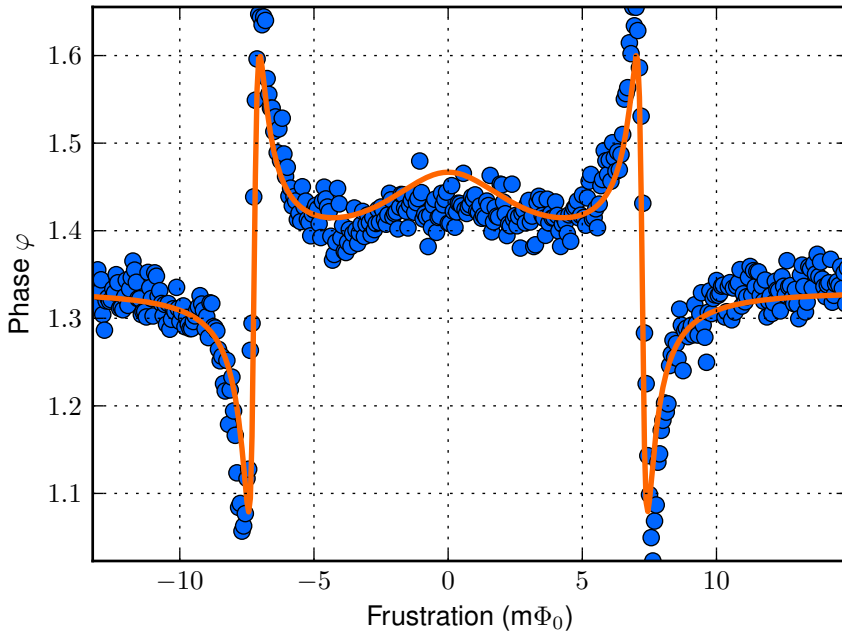


**Figure .1:** Transmitted phase through a resonator containing a single flux qubit with known parameters. In order to compare the expected coupling with the fitted coupling, the solid line shows a two-parameter fit as described in the main text. The expected coupling is  $g_{qr} = 2\pi \cdot (4.7 \pm 0.3)$  MHz, while the best fit is obtained for  $\tilde{g}_{qr} = 2\pi \cdot 4.9$  MHz.

## References

- [AAN+08] A. A. Abdumalikov, O. Astafiev, Y. Nakamura, Y. A. Pashkin, and J. Tsai. “Vacuum Rabi splitting due to strong coupling of a flux qubit and a coplanar-waveguide resonator”. In: *Phys. Rev. B* 78 (18 2008), p. 180502. DOI: 10.1103/PhysRevB.78.180502 (cit. on p. 20).
- [AB63] V. Ambegaokar and A. Baratoff. “Tunneling Between Superconductors”. In: *Phys. Rev. Lett.* 10 (11 1963), pp. 486–489. DOI: 10.1103/PhysRevLett.10.486 (cit. on p. 9).
- [Anl11] S. M. Anlage. “The physics and applications of superconducting metamaterials”. In: *Journal of Optics* 13.2 (2011), p. 024001. DOI: doi:10.1088/2040-8978/13/2/024001 (cit. on p. 4).
- [AWB+09] M. Ansmann, H. Wang, R. C. Bialczak, M. Hofheinz, E. Lucero, M. Neeley, A. D. O’Connell, D. Sank, M. Weides, J. Wenner, A. N. Cleland, and J. M. Martinis. “Violation of Bell’s inequality in Josephson phase qubits”. In: *Nature* 461.7263 (2009), pp. 504–506. DOI: 10.1038/nature08363 (cit. on p. 1).
- [AIN+07] O. Astafiev, K. Inomata, A. O. Niskanen, T. Yamamoto, Y. A. Pashkin, Y. Nakamura, and J. S. Tsai. “Single artificial-atom lasing”. In: *Nature* 449.7162 (2007), pp. 588–590. DOI: 10.1038/nature06141 (cit. on p. 2).
- [BKM+13] R. Barends, J. Kelly, A. Megrant, D. Sank, E. Jeffrey, Y. Chen, Y. Yin, B. Chiaro, J. Mutus, C. Neill, P. O’Malley, P. Roushan, J. Wenner, T. C. White, A. N. Cleland, and J. M. Martinis. “Coherent Josephson qubit suitable for scalable quantum integrated circuits”. In: *arXiv:1304.2322* (2013). URL: <http://arxiv.org/abs/1304.2322> (cit. on p. 7).

- [BGW+07] A. Blais, J. Gambetta, A. Wallraff, D. I. Schuster, S. M. Girvin, M. H. Devoret, and R. J. Schoelkopf. “Quantum-information processing with circuit quantum electrodynamics”. In: *Phys. Rev. A* 75 (3 2007), p. 032329. DOI: 10.1103/PhysRevA.75.032329 (cit. on p. 28).
- [BHW+04] A. Blais, R.-S. Huang, A. Wallraff, S. M. Girvin, and R. J. Schoelkopf. “Cavity quantum electrodynamics for superconducting electrical circuits: An architecture for quantum computation”. In: *Phys. Rev. A* 69 (6 2004), p. 062320. DOI: 10.1103/PhysRevA.69.062320 (cit. on pp. 22, 31, 68, 90).
- [BS40] F. Bloch and A. Siegert. “Magnetic Resonance for Nonrotating Fields”. In: *Phys. Rev.* 57 (6 1940), pp. 522–527. DOI: 10.1103/PhysRev.57.522 (cit. on p. 20).
- [BGA+09] J. Bourassa, J. M. Gambetta, A. A. Abdumalikov, O. Astafiev, Y. Nakamura, and A. Blais. “Ultrastrong coupling regime of cavity QED with phase-biased flux qubits”. In: *Phys. Rev. A* 80 (3 2009), p. 032109. DOI: 10.1103/PhysRevA.80.032109 (cit. on p. 20).
- [Bre09] C. F. Brennecke. “Collective Interaction Between a Bose-Einstein Condensate and a Coherent Few-Photon Field”. PhD thesis. Swiss Federal Institute of Technology Zurich, 2009 (cit. on p. 21).
- [Bri05] A. Maassen van den Brink. “Hamiltonian for coupled flux qubits”. In: *Phys. Rev. B* 71 (6 2005), p. 064503. DOI: 10.1103/PhysRevB.71.064503 (cit. on p. 10).
- [BFR+11] P. Bushev, A. K. Feofanov, H. Rotzinger, I. Protopopov, J. H. Cole, C. M. Wilson, G. Fischer, A. Lukashenko, and A. V. Ustinov. “Ultralow-power spectroscopy of a rare-earth spin ensemble using a superconducting resonator”. In: *Phys. Rev. B* 84 (6 2011), p. 060501. DOI: 10.1103/PhysRevB.84.060501 (cit. on p. 4).

- [CBIH+08] M. A. Castellanos-Beltran, K. D. Irwin, G. C. Hilton, L. R. Vale, and K. W. Lehnert. “Amplification and squeezing of quantum noise with a tunable Josephson metamaterial”. In: *Nature Physics* 4.12 (2008), pp. 929–931. DOI: 10.1038/nphys1090 (cit. on p. 4).
- [CVC+13] J. Chang, M. R. Vissers, A. D. Corcoles, M. Sandberg, J. Gao, D. W. Abraham, J. M. Chow, J. M. Gambetta, M. B. Rothwell, G. A. Keefe, M. Steffen, and D. P. Pappas. “Improved superconducting qubit coherence using titanium nitride”. In: *arXiv:1303.4071* (2013). URL: <http://arxiv.org/abs/1303.4071> (cit. on p. 1).
- [CNH+03] I. Chiorescu, Y. Nakamura, C. Harmans, and J. Mooij. “Coherent quantum dynamics of a superconducting flux qubit”. In: *Science* 299.5614 (2003), pp. 1869–1871. DOI: 10.1126/science.1081045 (cit. on p. 1).
- [CZ12] J. I. Cirac and P. Zoller. “Goals and opportunities in quantum simulation”. In: *Nature Physics* 8.4 (2012), pp. 264–266. DOI: 10.1038/nphys2275 (cit. on p. 1).
- [CW08] J. Clarke and F. K. Wilhelm. “Superconducting quantum bits”. In: *Nature* 453.7198 (2008), pp. 1031–1042. DOI: 10.1038/nature07128 (cit. on p. 1).
- [CTDRG98] C. Cohen-Tannoudji, J. Dupont-Roc, and G. Grynberg. “Atom-Photon Interactions: Basic Process and Applications”. In: *John Wiley, New York* (1998) (cit. on pp. 53, 54).
- [DS13] M. Devoret and R. Schoelkopf. “Superconducting Circuits for Quantum Information: An Outlook”. In: *Science* 339.6124 (2013), pp. 1169–1174. DOI: 10.1126/science.1231930 (cit. on p. 1).
- [Dic54] R. Dicke. “Coherence in spontaneous radiation processes”. In: *Physical Review* 93.1 (1954), p. 99. DOI: 10.1103/PhysRev.93.99 (cit. on p. 59).

## References

---

- [Dol77] G. J. Dolan. “Offset masks for lift-off photoprocessing”. In: *Appl. Phys. Lett.* 31.5 (1977), pp. 337–339. DOI: 10.1063/1.89690 (cit. on p. 65).
- [DCL06] C. Du, H. Chen, and S. Li. “Quantum left-handed metamaterial from superconducting quantum-interference devices”. In: *Phys. Rev. B* 74 (11 2006), p. 113105. DOI: 10.1103/PhysRevB.74.113105 (cit. on p. 4).
- [EW13] D. J. Egger and F. K. Wilhelm. “Multimode circuit QED with hybrid metamaterial transmission lines”. In: *arXiv:1302.5553* (2013). URL: <http://arxiv.org/abs/1302.5553> (cit. on p. 4).
- [FFM+10] A. Fedorov, A. K. Feofanov, P. Macha, P. Forn-Díaz, C. J. P. M. Harmans, and J. E. Mooij. “Strong Coupling of a Quantum Oscillator to a Flux Qubit at Its Symmetry Point”. In: *Phys. Rev. Lett.* 105 (6 2010), p. 060503. DOI: 10.1103/PhysRevLett.105.060503 (cit. on pp. 31, 101).
- [FMF+11] A. Fedorov, P. Macha, A. K. Feofanov, C. J. P. M. Harmans, and J. E. Mooij. “Tuned Transition from Quantum to Classical for Macroscopic Quantum States”. In: *Phys. Rev. Lett.* 106 (17 2011), p. 170404. DOI: 10.1103/PhysRevLett.106.170404 (cit. on pp. 1, 14).
- [FSB+11] A. Fedorov, L. Steffen, M. Baur, M. da Silva, and A. Wallraff. “Implementation of a Toffoli gate with superconducting circuits”. In: *Nature* 481.7380 (2011), pp. 170–172. DOI: 10.1038/nature10713 (cit. on p. 3).
- [FLS71] R. Feynman, R. B. Leighton, and M. Sands. “Lectures on physics. Vol. 3”. In: *Addison Wesley* (1971) (cit. on p. 8).
- [FSS+10] J. M. Fink, L. Steffen, P. Studer, L. S. Bishop, M. Baur, R. Bianchetti, D. Bozyigit, C. Lang, S. Filipp, P. J. Leek, and A. Wallraff. “Quantum-To-Classical Transition in Cavity Quantum Electrodynamics”. In: *Phys. Rev. Lett.* 105 (16 2010), p. 163601. DOI: 10.1103/PhysRevLett.105.163601 (cit. on p. 59).

- [FDLM+10] P. Forn-Díaz, J. Lisenfeld, D. Marcos, J. J. García-Ripoll, E. Solano, C. J. P. M. Harmans, and J. E. Mooij. “Observation of the Bloch-Siegert Shift in a Qubit-Oscillator System in the Ultrastrong Coupling Regime”. In: *Phys. Rev. Lett.* 105 (23 2010), p. 237001. DOI: 10.1103/PhysRevLett.105.237001 (cit. on pp. 2, 20, 31).
- [FD10] P. Forn-Díaz. “Superconducting Qubits and Quantum Resonators”. PhD thesis. Delft University of Technology, 2010 (cit. on p. 13).
- [FPC+00] J. R. Friedman, V. Patel, W. Chen, S. Tolpygo, and J. E. Lukens. “Quantum superposition of distinct macroscopic states”. In: *Nature* 406.6791 (2000), pp. 43–46. DOI: 10.1038/35017505 (cit. on p. 1).
- [GLP+13] K. Geerlings, Z. Leghtas, I. M. Pop, S. Shankar, L. Frunzio, R. J. Schoelkopf, M. Mirrahimi, and M. H. Devoret. “Demonstrating a Driven Reset Protocol for a Superconducting Qubit”. In: *Phys. Rev. Lett.* 110 (12 2013), p. 120501. DOI: 10.1103/PhysRevLett.110.120501 (cit. on p. 35).
- [GDS09] S. M. Girvin, M. H. Devoret, and R. J. Schoelkopf. “Circuit QED and engineering charge-based superconducting qubits”. In: *Physica Scripta* 2009.T137 (2009), p. 014012. DOI: 10.1088/0031-8949/2009/T137/014012 (cit. on p. 1).
- [GIP+05] M. Grajcar, A. Izmailkov, S. H. W. van der Ploeg, S. Linzen, E. Il’ichev, T. Wagner, U. Hübner, H.-G. Meyer, A. Maassen van den Brink, S. Uchaikin, and A. M. Zagoskin. “Direct Josephson coupling between superconducting flux qubits”. In: *Phys. Rev. B* 72 (2 2005), p. 020503. DOI: 10.1103/PhysRevB.72.020503 (cit. on p. 16).
- [GPI+08] M. Grajcar, S. H. W. van der Ploeg, A. Izmailkov, E. Il’ichev, H.-G. Meyer, A. Fedorov, A. Shnirman, and G. Schön. “Sisyphus cooling and amplification by a superconducting qubit”. In: *Nature physics* 4.8 (2008), pp. 612–616. DOI: doi:10.1038/nphys1019 (cit. on p. 3).

- [GYB+12] S. Gustavsson, F. Yan, J. Bylander, F. Yoshihara, Y. Nakamura, T. P. Orlando, and W. D. Oliver. “Dynamical Decoupling and Dephasing in Interacting Two-Level Systems”. In: *Phys. Rev. Lett.* 109 (1 2012), p. 010502. DOI: 10.1103/PhysRevLett.109.010502 (cit. on p. 35).
- [HFA+08] J. Hauss, A. Fedorov, S. André, V. Brosco, C. Hutter, R. Kothari, S. Yeshwanth, A. Shnirman, and G. Schön. “Dissipation in circuit quantum electrodynamics: lasing and cooling of a low-frequency oscillator”. In: *New Journal of Physics* 10.9 (2008), p. 095018. DOI: 10.1088/1367-2630/10/9/095018 (cit. on p. 55).
- [HFH+08] J. Hauss, A. Fedorov, C. Hutter, A. Shnirman, and G. Schön. “Single-Qubit Lasing and Cooling at the Rabi Frequency”. In: *Phys. Rev. Lett.* 100 (3 2008), p. 037003. DOI: 10.1103/PhysRevLett.100.037003 (cit. on pp. 3, 53).
- [HRP+06] T. Hime, P. A. Reichardt, B. L. T. Plourde, T. L. Robertson, C. E. Wu, A. V. Ustinov, and J. Clarke. “Solid-state qubits with current-controlled coupling”. English. In: *SCIENCE* 314.5804 (2006), 1427–1429. ISSN: 0036-8075. DOI: 10.1126/science.1134388 (cit. on p. 16).
- [HTK12] A. A. Houck, H. E. Türeci, and J. Koch. “On-chip quantum simulation with superconducting circuits”. In: *Nature Physics* 8.4 (2012), pp. 292–299. DOI: 10.1038/NPHYS2251 (cit. on p. 1).
- [IOI+03] E. Il’ichev, N. Oukhanski, A. Izmalkov, T. Wagner, M. Grajcar, H.-G. Meyer, A. Y. Smirnov, A. Maassen van den Brink, M. H. S. Amin, and A. M. Zagoskin. “Continuous Monitoring of Rabi Oscillations in a Josephson Flux Qubit”. In: *Phys. Rev. Lett.* 91 (9 2003), p. 097906. DOI: 10.1103/PhysRevLett.91.097906 (cit. on pp. 3, 20).
- [IGI+04] A. Izmalkov, M. Grajcar, E. Il’ichev, T. Wagner, H.-G. Meyer, A. Y. Smirnov, M. H. S. Amin, A. M. van den Brink, and A. M. Zagoskin. “Evidence for Entangled States of Two Coupled

- Flux Qubits". In: *Phys. Rev. Lett.* 93 (3 2004), p. 037003. DOI: 10.1103/PhysRevLett.93.037003 (cit. on p. 78).
- [IPS+08] A. Izmalkov, S. H. W. van der Ploeg, S. N. Shevchenko, M. Grajcar, E. Il'ichev, U. Hübner, A. N. Omelyanchouk, and H.-G. Meyer. "Consistency of Ground State and Spectroscopic Measurements on Flux Qubits". In: *Phys. Rev. Lett.* 101 (1 2008), p. 017003. DOI: 10.1103/PhysRevLett.101.017003 (cit. on p. 59).
- [Jer09] M. Jerger. "Experiments on Superconducting Qubits Coupled to Resonators". PhD thesis. Karlsruher Institut für Technologie (KIT), 2009 (cit. on p. 41).
- [JPM+11] M. Jerger, S. Poletto, P. Macha, U. Hübner, A. Lukashenko, E. Il'ichev, and A. V. Ustinov. "Readout of a qubit array via a single transmission line". In: *EPL (Europhys. Lett.)* 96.4 (2011), p. 40012. DOI: 10.1209/0295-5075/96/40012 (cit. on pp. 65, 71).
- [JPM+12] M. Jerger, S. Poletto, P. Macha, U. Hubner, E. Il'ichev, and A. V. Ustinov. "Frequency division multiplexing readout and simultaneous manipulation of an array of flux qubits". In: *Appl. Phys. Lett.* 101.4, 042604 (2012), p. 042604. DOI: 10.1063/1.4739454 (cit. on p. 3).
- [JBS+13] P. Jung, S. Butz, S. V. Shitov, and A. V. Ustinov. "Low-loss tunable metamaterials using superconducting circuits with Josephson junctions". In: *Appl. Phys. Lett.* 102.6, 062601 (2013), p. 062601. DOI: 10.1063/1.4792705 (cit. on p. 4).
- [KMS+07] K. Kakuyanagi, T. Meno, S. Saito, H. Nakano, K. Semba, H. Takayanagi, F. Deppe, and A. Shnirman. "Dephasing of a Superconducting Flux Qubit". In: *Phys. Rev. Lett.* 98 (4 2007), p. 047004. DOI: 10.1103/PhysRevLett.98.047004 (cit. on p. 41).
- [KVG88] G. Khitrova, J. F. Valley, and H. M. Gibbs. "Gain-feedback approach to optical instabilities in sodium vapor". In: *Phys. Rev. Lett.* 60 (12 1988), pp. 1126–1129. DOI: 10.1103/PhysRevLett.60.1126 (cit. on p. 3).

## References

---

- [KVL+13] G. Kirchmair, B. Vlastakis, Z. Leghtas, S. E. Nigg, H. Paik, E. Ginossar, M. Mirrahimi, L. Frunzio, S. M. Girvin, and R. J. Schoelkopf. “Observation of quantum state collapse and revival due to the single-photon Kerr effect”. In: *Nature* 495.7440 (2013), pp. 205–209. DOI: 10.1038/nature11902 (cit. on p. 2).
- [KYG+07] J. Koch, T. M. Yu, J. Gambetta, A. A. Houck, D. I. Schuster, J. Majer, A. Blais, M. H. Devoret, S. M. Girvin, and R. J. Schoelkopf. “Charge-insensitive qubit design derived from the Cooper pair box”. In: *Phys. Rev. A* 76 (4 2007), p. 042319. DOI: 10.1103/PhysRevA.76.042319 (cit. on p. 7).
- [LCJ+09] N. Lambert, Y.-n. Chen, R. Johansson, and F. Nori. “Quantum chaos and critical behavior on a chip”. In: *Phys. Rev. B* 80 (16 2009), p. 165308. DOI: 10.1103/PhysRevB.80.165308 (cit. on p. 5).
- [LT07] N. Lazarides and G. P. Tsironis. “rf superconducting quantum interference device metamaterials”. In: *Appl. Phys. Lett.* 90.16, 163501 (2007), p. 163501. DOI: 10.1063/1.2722682 (cit. on p. 4).
- [LLA+07] J. Lisenfeld, A. Lukashenko, M. Ansmann, J. M. Martinis, and A. V. Ustinov. “Temperature Dependence of Coherent Oscillations in Josephson Phase Qubits”. In: *Phys. Rev. Lett.* 99 (17 2007), p. 170504. DOI: 10.1103/PhysRevLett.99.170504 (cit. on p. 35).
- [LSN06] Y.-x. Liu, C. P. Sun, and F. Nori. “Scalable superconducting qubit circuits using dressed states”. In: *Phys. Rev. A* 74 (5 2006), p. 052321. DOI: 10.1103/PhysRevA.74.052321. URL: <http://link.aps.org/doi/10.1103/PhysRevA.74.052321> (cit. on p. 46).
- [LBC+12] E. Lucero, R. Barends, Y. Chen, J. Kelly, M. Mariantoni, A. Megrant, P. O’Malley, D. Sank, A. Vainsencher, J. Wenner, et al. “Computing prime factors with a Josephson phase qubit quantum processor”. In: *Nature Physics* (2012). DOI: 10.1038/NPHYS2385 (cit. on p. 3).

- [LBD+09] A. Lupascu, P. Bertet, E. F. C. Driessen, C. J. P. M. Harmans, and J. E. Mooij. “One- and two-photon spectroscopy of a flux qubit coupled to a microscopic defect”. In: *Phys. Rev. B* 80 (17 2009), p. 172506. DOI: 10.1103/PhysRevB.80.172506 (cit. on p. 35).
- [MPO+10] P. Macha, S. H. W. van der Ploeg, G. Oelsner, E. Ilichev, H.-G. Meyer, S. Wunsch, and M. Siegel. “Losses in coplanar waveguide resonators at millikelvin temperatures”. In: *Appl. Phys. Lett.* 96.6 (2010), pp. 062503–062503. DOI: 10.1063/1.3309754 (cit. on p. 35).
- [MCG+07] J. Majer, J. Chow, J. Gambetta, J. Koch, B. Johnson, J. Schreier, L. Frunzio, D. Schuster, A. Houck, A. Wallraff, et al. “Coupling superconducting qubits via a cavity bus”. In: *Nature* 449.7161 (2007), pp. 443–447. DOI: 10.1038/nature06184 (cit. on p. 29).
- [MPH+05] J. B. Majer, F. G. Paauw, A. C. J. ter Haar, C. J. P. M. Harmans, and J. E. Mooij. “Spectroscopy on Two Coupled Superconducting Flux Qubits”. In: *Phys. Rev. Lett.* 94 (9 2005), p. 090501. DOI: 10.1103/PhysRevLett.94.090501 (cit. on p. 17).
- [MCM+05] J. M. Martinis, K. B. Cooper, R. McDermott, M. Steffen, M. Ansmann, K. D. Osborn, K. Cicak, S. Oh, D. P. Pappas, R. W. Simmonds, and C. C. Yu. “Decoherence in Josephson Qubits from Dielectric Loss”. In: *Phys. Rev. Lett.* 95 (21 2005), p. 210503. DOI: 10.1103/PhysRevLett.95.210503 (cit. on p. 35).
- [MBB+03] J. McKeever, A. Boca, A. D. Boozer, J. R. Buck, and H. J. Kimble. “Experimental realization of a one-atom laser in the regime of strong coupling”. In: *Nature* 425.6955 (2003), pp. 268–271. DOI: 10.1038/nature01974 (cit. on p. 2).
- [MC00] J. Mompert and R. Corbalán. “Lasing without inversion”. In: *Journal of Optics B: Quantum and Semiclassical Optics* 2.3 (2000), R7. DOI: 10.1088/1464-4266/2/3/201 (cit. on p. 3).

- [MOL+99] J. E. Mooij, T. P. Orlando, L. Levitov, L. Tian, C. H. van der Wal, and S. Lloyd. “Josephson Persistent-Current Qubit”. In: *Science* 285.5430 (1999), pp. 1036–1039. doi: 10.1126/science.285.5430.1036 (cit. on pp. 2, 10, 11).
- [MVZ+12] K. W. Murch, U. Vool, D. Zhou, S. J. Weber, S. M. Girvin, and I. Siddiqi. “Cavity-Assisted Quantum Bath Engineering”. In: *Phys. Rev. Lett.* 109 (18 2012), p. 183602. doi: 10.1103/PhysRevLett.109.183602 (cit. on p. 46).
- [NPT99] Y. Nakamura, Y. A. Pashkin, and J. Tsai. “Coherent control of macroscopic quantum states in a single-Cooper-pair box”. In: *Nature* 398.6730 (1999), pp. 786–788. doi: doi:10.1038/19718 (cit. on p. 1).
- [NC10] P. Nataf and C. Ciuti. “Vacuum Degeneracy of a Circuit QED System in the Ultrastrong Coupling Regime”. In: *Phys. Rev. Lett.* 104 (2 2010), p. 023601. doi: 10.1103/PhysRevLett.104.023601 (cit. on pp. 106, 109).
- [NDH+10] T. Niemczyk, F. Deppe, H. Huebl, E. P. Menzel, F. Hocke, M. J. Schwarz, J. J. García-Ripoll, D. Zueco, T. Hümmer, E. Solano, et al. “Circuit quantum electrodynamics in the ultrastrong-coupling regime”. In: *Nature Physics* 6.10 (2010), pp. 772–776. doi: 10.1038/NPHYS1730 (cit. on p. 20).
- [OMA+13] G. Oelsner, P. Macha, O. V. Astafiev, E. Il’ichev, M. Grajcar, U. Hübner, B. I. Ivanov, P. Neilinger, and H.-G. Meyer. “Dressed-State Amplification by a Single Superconducting Qubit”. In: *Phys. Rev. Lett.* 110 (5 2013), p. 053602. doi: 10.1103/PhysRevLett.110.053602 (cit. on pp. 32, 53, 55).
- [OPM+10] G. Oelsner, S. H. W. van der Ploeg, P. Macha, U. Hübner, D. Born, S. Anders, E. Il’ichev, H.-G. Meyer, M. Grajcar, S. Wunsch, M. Siegel, A. N. Omelyanchouk, and O. Astafiev. “Weak continuous monitoring of a flux qubit using coplanar waveguide resonator”. In: *Phys. Rev. B* 81 (17 2010), p. 172505. doi: 10.1103/PhysRevB.81.172505 (cit. on pp. 31, 80).

- [OSG+10] A. N. Omelyanchouk, S. N. Shevchenko, Y. S. Greenberg, O. Astafiev, and E. Il'ichev. "Quantum behavior of a flux qubit coupled to a resonator". In: *Low Temp. Phys.* 36.10 (2010), pp. 893–901. DOI: 10.1063/1.3515520 (cit. on p. 80).
- [OMT+99] T.P.Orlando, J. E. Mooij, L. Tian, C. H. van der Wal, L. S. Levitov, S. Lloyd, and J. J. Mazo. "Superconducting persistent-current qubit". In: *Phys. Rev. B* 60 (22 1999), pp. 15398–15413. DOI: 10.1103/PhysRevB.60.15398 (cit. on pp. 11, 13).
- [Paa09] F. G. Paauw. "Superconducting flux qubits. quantum chains and tunable qubits". PhD thesis. Delft University of Technology, 2009 (cit. on pp. 16, 17, 60).
- [PSB+11] H. Paik, D. I. Schuster, L. S. Bishop, G. Kirchmair, G. Catelani, A. P. Sears, B. R. Johnson, M. J. Reagor, L. Frunzio, L. I. Glazman, S. M. Girvin, M. H. Devoret, and R. J. Schoelkopf. "Observation of High Coherence in Josephson Junction Qubits Measured in a Three-Dimensional Circuit QED Architecture". In: *Phys. Rev. Lett.* 107 (24 2011), p. 240501. DOI: 10.1103/PhysRevLett.107.240501 (cit. on pp. 1, 35).
- [PIB+07] S. H. W. van der Ploeg, A. Izmalkov, A. M. van den Brink, U. Hübner, M. Grajcar, E. Il'ichev, H.-G. Meyer, and A. M. Zagoskin. "Controllable Coupling of Superconducting Flux Qubits". In: *Phys. Rev. Lett.* 98 (5 2007), p. 057004. DOI: 10.1103/PhysRevLett.98.057004 (cit. on p. 16).
- [PCC+09] S. Poletto, F. Chiarello, M. G. Castellano, J. Lisenfeld, A. Lukashenko, C. Cosmelli, G. Torrioli, P. Carelli, and A. V. Ustinov. "Coherent oscillations in a superconducting tunable flux qubit manipulated without microwaves". In: *New Journal of Physics* 11.1 (2009), p. 013009. DOI: 10.1088/1367-2630/11/1/013009 (cit. on p. 1).
- [PRW+13] S. Probst, H. Rotzinger, S. Wunsch, P. Jung, M. Jerger, M. Siegel, A. V. Ustinov, and P. A. Bushev. "Anisotropic Rare-Earth Spin Ensemble Strongly Coupled to a Superconducting Resonator". In: *Phys. Rev. Lett.* 110 (15 2013), p. 157001. DOI: 10.1103/PhysRevLett.110.157001 (cit. on p. 93).

- [RBH01] J. M. Raimond, M. Brune, and S. Haroche. “Manipulating quantum entanglement with atoms and photons in a cavity”. In: *Reviews of Modern Physics* 73.3 (2001), p. 565. DOI: 10.1103/RevModPhys.73.565 (cit. on pp. 20, 31).
- [RTB+89] M. G. Raizen, R. J. Thompson, R. J. Brecha, H. J. Kimble, and H. J. Carmichael. “Normal-mode splitting and linewidth averaging for two-state atoms in an optical cavity”. In: *Phys. Rev. Lett.* 63 (3 1989), pp. 240–243. DOI: 10.1103/PhysRevLett.63.240 (cit. on p. 20).
- [RZS+08] A. L. Rakhmanov, A. M. Zagoskin, S. Savel’ev, and F. Nori. “Quantum metamaterials: Electromagnetic waves in a Josephson qubit line”. In: *Phys. Rev. B* 77 (14 2008), p. 144507. DOI: 10.1103/PhysRevB.77.144507 (cit. on pp. 3, 59).
- [RJH+10] M. D. Reed, B. R. Johnson, A. A. Houck, L. DiCarlo, J. M. Chow, D. I. Schuster, L. Frunzio, and R. J. Schoelkopf. “Fast reset and suppressing spontaneous emission of a superconducting qubit”. In: *Appl. Phys. Lett.* 96.20, 203110 (2010), p. 203110. DOI: 10.1063/1.3435463 (cit. on p. 35).
- [Rei12] J.-M. Reiner. “Kollektive Eigenschaften von Multi-Qubit-Systemen in der Circuit Quantenelektrodynamik”. Bachelor thesis. Karlsruher Institute für Technologie, 2012 (cit. on pp. 22, 23).
- [ROA05] M. Ricci, N. Orloff, and S. M. Anlage. “Superconducting metamaterials”. In: *Appl. Phys. Lett.* 87.3 (2005), pp. 034102–034102. DOI: 10.1063/1.1996844 (cit. on p. 4).
- [RBD05] C. Rigetti, A. Blais, and M. Devoret. “Protocol for Universal Gates in Optimally Biased Superconducting Qubits”. In: *Phys. Rev. Lett.* 94 (24 2005), p. 240502. DOI: 10.1103/PhysRevLett.94.240502 (cit. on p. 46).
- [RGP+12] C. Rigetti, J. M. Gambetta, S. Poletto, B. L. T. Plourde, J. M. Chow, A. D. Córcoles, J. A. Smolin, S. T. Merkel, J. R. Rozen, G. A. Keefe, M. B. Rothwell, M. B. Ketchen, and M. Steffen. “Superconducting qubit in a waveguide cavity with a coherence time approaching 0.1 ms”. In: *Phys. Rev. B* 86 (10

- 2012), p. 100506. DOI: [10.1103/PhysRevB.86.100506](https://doi.org/10.1103/PhysRevB.86.100506) (cit. on pp. 1, 35).
- [RGRS09] G. Romero, J. J. Garcia-Ripoll, and E. Solano. “Microwave Photon Detector in Circuit QED”. In: *Phys. Rev. Lett.* 102 (17 2009), p. 173602. DOI: [10.1103/PhysRevLett.102.173602](https://doi.org/10.1103/PhysRevLett.102.173602) (cit. on p. 5).
- [SDZ+11] C. Sayrin, I. Dotsenko, X. Zhou, B. Peaudecerf, T. Rybarczyk, S. Gleyzes, P. Rouchon, M. Mirrahimi, H. Amini, M. Brune, et al. “Real-time quantum feedback prepares and stabilizes photon number states”. In: *Nature* 477.7362 (2011), pp. 73–77. DOI: [10.1038/nature10376](https://doi.org/10.1038/nature10376) (cit. on p. 2).
- [SSG+10] D. I. Schuster, A. P. Sears, E. Ginossar, L. DiCarlo, L. Frunzio, J. J. L. Morton, H. Wu, G. A. D. Briggs, B. B. Buckley, D. D. Awschalom, and R. J. Schoelkopf. “High-Cooperativity Coupling of Electron-Spin Ensembles to Superconducting Cavities”. In: *Phys. Rev. Lett.* 105 (14 2010), p. 140501. DOI: [10.1103/PhysRevLett.105.140501](https://doi.org/10.1103/PhysRevLett.105.140501) (cit. on p. 4).
- [SWB+05] D. I. Schuster, A. Wallraff, A. Blais, L. Frunzio, R.-S. Huang, J. Majer, S. M. Girvin, and R. J. Schoelkopf. “ac Stark Shift and Dephasing of a Superconducting Qubit Strongly Coupled to a Cavity Field”. In: *Phys. Rev. Lett.* 94 (12 2005), p. 123602. DOI: [10.1103/PhysRevLett.94.123602](https://doi.org/10.1103/PhysRevLett.94.123602) (cit. on pp. 41, 101).
- [SHK+08] S. Sendelbach, D. Hover, A. Kittel, M. Mück, J. M. Martinis, and R. McDermott. “Magnetism in SQUIDS at Millikelvin Temperatures”. In: *Phys. Rev. Lett.* 100 (22 2008), p. 227006. DOI: [10.1103/PhysRevLett.100.227006](https://doi.org/10.1103/PhysRevLett.100.227006) (cit. on p. 43).
- [Son] *Sonnet® User’s Guide – Release 12 – Manual of the Program Sonnet* ®. Sonnet Software Inc. 100 Elwood Davis Road North Syracuse NY 13212 USA. 2009 (cit. on p. 63).
- [SW03] M. J. Storcz and F. K. Wilhelm. “Decoherence and gate performance of coupled solid-state qubits”. In: *Phys. Rev. A* 67 (4 2003), p. 042319. DOI: [10.1103/PhysRevA.67.042319](https://doi.org/10.1103/PhysRevA.67.042319) (cit. on p. 17).

- [TC68] M. Tavis and F. W. Cummings. “Exact solution for an N-molecule-radiation-field Hamiltonian”. In: *Phys. Rev.* 170 (1968), pp. 379–384. DOI: [10.1103/PhysRev.170.379](https://doi.org/10.1103/PhysRev.170.379) (cit. on p. 21).
- [Tia10] L. Tian. “Circuit QED and Sudden Phase Switching in a Superconducting Qubit Array”. In: *Phys. Rev. Lett.* 105 (16 2010), p. 167001. DOI: [10.1103/PhysRevLett.105.167001](https://doi.org/10.1103/PhysRevLett.105.167001) (cit. on pp. 5, 67).
- [TSS+10] J. Tuorila, M. Silveri, M. Sillanpää, E. Thuneberg, Y. Makhlin, and P. Hakonen. “Stark Effect and Generalized Bloch-Siegert Shift in a Strongly Driven Two-Level System”. In: *Phys. Rev. Lett.* 105 (25 2010), p. 257003. DOI: [10.1103/PhysRevLett.105.257003](https://doi.org/10.1103/PhysRevLett.105.257003) (cit. on p. 20).
- [VMS+12] R. Vijay, C. Macklin, D. H. Slichter, S. Weber, K. Murch, R. Naik, A. N. Korotkov, and I. Siddiqi. “Stabilizing Rabi oscillations in a superconducting qubit using quantum feedback”. In: *Bulletin of the American Physical Society* 57 (2012) (cit. on p. 2).
- [VSS11] R. Vijay, D. H. Slichter, and I. Siddiqi. “Observation of Quantum Jumps in a Superconducting Artificial Atom”. In: *Phys. Rev. Lett.* 106 (11 2011), p. 110502. DOI: [10.1103/PhysRevLett.106.110502](https://doi.org/10.1103/PhysRevLett.106.110502) (cit. on p. 4).
- [WSB+07] A. Wallraff, D. I. Schuster, A. Blais, J. M. Gambetta, J. Schreier, L. Frunzio, M. H. Devoret, S. M. Girvin, and R. J. Schoelkopf. “Sideband Transitions and Two-Tone Spectroscopy of a Superconducting Qubit Strongly Coupled to an On-Chip Cavity”. In: *Phys. Rev. Lett.* 99 (5 2007), p. 050501. DOI: [10.1103/PhysRevLett.99.050501](https://doi.org/10.1103/PhysRevLett.99.050501) (cit. on p. 47).
- [WSB+04] A. Wallraff, D. Schuster, A. Blais, L. Frunzio, R. Huang, J. Majer, S. Kumar, S. Girvin, and R. Schoelkopf. “Strong coupling of a single photon to a superconducting qubit using circuit quantum electrodynamics”. In: *Nature* 431.7005 (2004), pp. 162–167. DOI: [10.1038/nature02851](https://doi.org/10.1038/nature02851) (cit. on pp. 1, 20).

- [Whi01] S. Whitely. “FastHenry 3.0 wr (2001)”. In: *The code is available at <http://www.wrcad.com>* (2001) (cit. on pp. 63, 66).
- [WJD+10] C. M. Wilson, G. Johansson, T. Duty, F. Persson, M. Sandberg, and P. Delsing. “Dressed relaxation and dephasing in a strongly driven two-level system”. In: *Phys. Rev. B* 81 (2 2010), p. 024520. DOI: 10.1103/PhysRevB.81.024520 (cit. on p. 46).
- [WJP+11] C. M. Wilson, G. Johansson, A. Pourkabirian, M. Simoen, J. R. Johansson, T. Duty, F. Nori, and P. Delsing. “Observation of the dynamical Casimir effect in a superconducting circuit”. In: *Nature* 479.7373 (2011), pp. 376–379. DOI: 10.1038/nature10561 (cit. on p. 1).
- [WM93] H. M. Wiseman and G. J. Milburn. “Quantum theory of optical feedback via homodyne detection”. In: *Phys. Rev. Lett.* 70 (5 1993), pp. 548–551. DOI: 10.1103/PhysRevLett.70.548 (cit. on p. 2).
- [WED+77] F. Y. Wu, S. Ezekiel, M. Ducloy, and B. R. Mollow. “Observation of Amplification in a Strongly Driven Two-Level Atomic System at Optical Frequencies”. In: *Phys. Rev. Lett.* 38 (19 1977), pp. 1077–1080. DOI: 10.1103/PhysRevLett.38.1077 (cit. on p. 3).
- [WGW+10] H. Wu, R. E. George, J. H. Wesenberg, K. Mølmer, D. I. Schuster, R. J. Schoelkopf, K. M. Itoh, A. Ardavan, J. J. L. Morton, and G. A. D. Briggs. “Storage of Multiple Coherent Microwave Excitations in an Electron Spin Ensemble”. In: *Phys. Rev. Lett.* 105 (14 2010), p. 140503. DOI: 10.1103/PhysRevLett.105.140503 (cit. on p. 4).
- [XAY+13] Z.-L. Xiang, S. Ashhab, J. Q. You, and F. Nori. “Hybrid quantum circuits: Superconducting circuits interacting with other quantum systems”. In: *Rev. Mod. Phys.* 85 (2 2013), pp. 623–653. DOI: 10.1103/RevModPhys.85.623 (cit. on p. 4).

## References

---

- [YBG+12] F. Yan, J. Bylander, S. Gustavsson, F. Yoshihara, K. Harrabi, D. G. Cory, T. P. Orlando, Y. Nakamura, J.-S. Tsai, and W. D. Oliver. “Spectroscopy of low-frequency noise and its temperature dependence in a superconducting qubit”. In: *Phys. Rev. B* 85 (17 2012), p. 174521. DOI: 10.1103/PhysRevB.85.174521 (cit. on p. 35).
- [YN11] J. You and F. Nori. “Atomic physics and quantum optics using superconducting circuits”. In: *Nature* 474.7353 (2011), pp. 589–597. DOI: 10.1038/nature10122 (cit. on p. 1).
- [ZK12] N. I. Zheludev and Y. S. Kivshar. “From metamaterials to metadevices”. In: *Nature materials* 11.11 (2012), pp. 917–924. DOI: 10.1038/NMAT3431 (cit. on pp. 3, 59).
- [ZRK+09] D. Zueco, G. M. Reuther, S. Kohler, and P. Hänggi. “Qubit-oscillator dynamics in the dispersive regime: Analytical theory beyond the rotating-wave approximation”. In: *Phys. Rev. A* 80 (3 2009), p. 033846. DOI: 10.1103/PhysRevA.80.033846 (cit. on pp. 28, 29).

## List of publications

1. P. Macha, G. Oelsner, J.-M. Reiner, M. Marthaler, S. André, G. Schön, U. Hübner, H.-G. Meyer, E. Il'ichev and A. V. Ustinov. *Implementation of a Quantum Metamaterial*. arXiv:1309.5268
2. G. Oelsner, P. Macha, O. V. Astafiev, E. Il'ichev, M. Grajcar, U. Hübner, B. I. Ivanov, P. Neilinger, H.-G. Meyer. *Dressed-State Amplification by a Single Superconducting Qubit*. Phys. Rev. Lett. **110**, 053602 (2013)
3. M. Jerger, S. Poletto, P. Macha, U. Hübner, E. Il'ichev, A. V. Ustinov. *Frequency division multiplexing readout and simultaneous manipulation of an array of flux qubits*. Appl. Phys. Lett. **101**, 042604 (2012)
4. M. Jerger, S. Poletto, P. Macha, U. Huebner, A. Lukashenko, E. Il'ichev, A. V. Ustinov. *Spectroscopy of a Qubit Array via a Single Transmission Line*. Europhys. Lett. **96**, 40012 (2011)
5. A. Fedorov, P. Macha, A. K. Feofanov, C. J. P. M. Harmans, J. E. Mooij. *Tuned transition from quantum to classical for macroscopic quantum states*. Phys. Rev. Lett. **106**, 170404 (2011)
6. A. Fedorov, A. K. Feofanov, P. Macha, P. Forn-Díaz, C. J. P. M. Harmans, J. E. Mooij. *Strong Coupling of a Quantum Oscillator to a Flux Qubit at its Symmetry Point*. Phys. Rev. Lett. **105**, 060503 (2010)
7. G. Oelsner, S. H. W. van der Ploeg, P. Macha, U. Hübner, D. Born, E. Il'ichev, H.-G. Meyer, M. Grajcar, S. Wunsch, M. Siegel, A. N. Omelyanchouk, O. Astafiev. *Weak continuous monitoring of a flux qubit using coplanar waveguide resonator*. Phys. Rev. B **81**, 172505 (2010)

*List of publications*

---

8. P. Macha, S. H. W. van der Ploeg, G. Oelsner, E. Il'ichev, H.-G. Meyer, S. Wuensch, M. Siegel. *Losses in coplanar waveguide resonators at millikelvin temperatures*. Appl. Phys. Lett. **96**, 062503 (2010)

# Acknowledgments

During the time of my PhD I went to a few places and met a lot of people. So first of all, *thank you all for everything*.

I thank Alexey Ustinov and Evgeni Il'ichev for their inspiration and for giving me the freedom to do my research. Most of the experiments that made it into this book were performed at the Institute for Photonic Technologies in Jena. I enjoyed working with Gregor Oelsner, who has impressed me with his tenacity and thank Boris Ivanov for support with the electronic setup. I thank Uwe Hübner and his team at the IPHT clean-room, especially Solveig Anders and Birger Steinbach, for the fabrication of very reliable samples. Many thanks to Detlef Born who helped us running and maintaining our cryostats. I would like to thank Hans-Georg Meyer and his group who hosted our lab and supported us in any way possible. There are many people from the IPHT whom I would like to thank for their support and a good atmosphere, among them Thorsten May, Jürgen Kunert, Jana Schaarschmidt, Detlef Scharf, Matthias Schmelz, Heike Schneider, Marion Sondermann, Marco Schubert, Slava Zakosarenko and Gabriel Zieger.

Alexey's group at the Karlsruhe Institute of Technology was always there. I had the pleasure to work with Markus Jerger and Stephano Poletto on the multiplexing readout project for superconducting qubits. Markus continues to impress me with his deep understanding of everything. I am thankful to Susanne Butz for numerous discussions on metamaterials and other important things in life. I was happy to meet Jürgen Lisenfeld already during my time in Delft, thank you for becoming my friend. I want to thank Sebastian Probst, Jochen Zimmer, Grigorij Grabovskij and Phillip Jung for their good company on many occasions, not only during conferences on physics at low temperatures. Pavel Bushev, we should have had more discussions, thank you for your input.

## *Acknowledgements*

---

For theory support I am indebted to Jan-Michael Reiner, Michael Marthaler and Gerd Schön. I'm thankful to Jan-Michael for getting things moving. Michael, you're right that science brings people together who would not have met otherwise, however same can be said about life.

At the beginning of my thesis I got the chance to visit the quantum transport group at the TU Delft. I thank Hans Mooij, from whom I learned a lot, for giving me this possibility. There, I could join Arkady Fedorov and we had a good and very productive time, thank you for that.

Oleg Astavief visited us for a few month in Jena and showed me that you can work anywhere, anytime. I enjoyed the numerous visits from Miroslav Grajcar, who's always thinking on his own terms. Yakov Greenberg came over from Russia calculating and calculating, thank you for your time.

Almost last but not least I thank my family, especially my parents Peter and Silvia who continue to support me through anything.

I thank Nadine, without her this thesis would not be. Auf das wir unsere Menschen bleiben.